



저작자표시-비영리-변경금지 2.0 대한민국

이용자는 아래의 조건을 따르는 경우에 한하여 자유롭게

- 이 저작물을 복제, 배포, 전송, 전시, 공연 및 방송할 수 있습니다.

다음과 같은 조건을 따라야 합니다:



저작자표시. 귀하는 원저작자를 표시하여야 합니다.



비영리. 귀하는 이 저작물을 영리 목적으로 이용할 수 없습니다.



변경금지. 귀하는 이 저작물을 개작, 변형 또는 가공할 수 없습니다.

- 귀하는, 이 저작물의 재이용이나 배포의 경우, 이 저작물에 적용된 이용허락조건을 명확하게 나타내어야 합니다.
- 저작권자로부터 별도의 허가를 받으면 이러한 조건들은 적용되지 않습니다.

저작권법에 따른 이용자의 권리는 위의 내용에 의하여 영향을 받지 않습니다.

이것은 [이용허락규약\(Legal Code\)](#)을 이해하기 쉽게 요약한 것입니다.

[Disclaimer](#)

# The antimetastatic effect of IGFBP-3 and the development of natural HSP90 inhibitor targeting cancer stemness

Thuy Huong Le

A thesis submitted in partial fulfillment of the requirement for the degree  
of

**Doctor of Pharmacy**

Graduate School of Pharmacy

Seoul National University

Physiology and Pathology Department

Under the supervision of Prof. Ho-Young Lee

02-2021

**Confirming the Ph.D. Dissertation written by**

**Thuy Huong Le**

Chair

Young Kee Shin

(Seal)

Vice-Chair

Yun-Hee Lee

(Seal)

Examiner

Hyo-Jong Lee

(Seal)

Examiner

Doo-gyeon Lee

(Seal)

Examiner

Ho-Young Lee

(Seal)



Ph.D. Dissertation of Graduation School of Pharmacy

**The antimetastatic effect of IGFBP-3 and  
the development of natural HSP90 inhibitor  
targeting cancer stemness**

February 2021

**Graduate School of Pharmacy  
Seoul National University  
Physiology and Pathology Department  
Thuy Huong Le**

# The antimetastatic effect of IGFBP-3 and the development of natural HSP90 inhibitor targeting cancer stemness

Thuy Huong Le

A thesis submitted in partial fulfillment of the requirement for the degree  
of

**Doctor of Pharmacy**

Graduate School of Pharmacy

Seoul National University

Physiology and Pathology Department

Under the supervision of Prof. Ho-Young Lee

02-2021

**Confirming the Ph.D. Dissertation written by**

**Thuy Huong Le**

Chair

Young Kee Shin

(Seal)

Vice-Chair

Yun-Hee Lee

(Seal)

Examiner

Hyo-Jong Lee

(Seal)

Examiner

Doo-yeon Lee

(Seal)

Examiner

Ho-Young Lee

(Seal)



## **ABSTRACT**

### **The antimetastatic effect of IGFBP-3 and the development of natural HSP90 inhibitor targeting cancer stemness**

**Thuy Huong Le**  
**College of pharmacy**  
**The graduate school**  
**Seoul National University**

Aerodigestive tract cancer, including non-small cell lung cancer (NSCLC) and head and neck squamous cell carcinoma (HNSCC), is the leading cause of cancer-related death worldwide. The poor prognosis in patients with NSCLC and HNSCC is frequently associated with migration and metastasis. However, there is no available therapeutic option to cure invasive and metastasis tumors due to the complexity of metastasis's biology.

Chapter 1 of this study investigates the antimetastatic effect of insulin-like growth factor binding protein-3 (IGFBP-3) in HNSCC and NSCLC. Depletion of IGFBP-3 enhances the migratory and invasive capacities of HNSCC and NSCLC cells *in vitro*, whereas overexpression of IGFBP-3 reverses these invasive phenotypes. Additionally, silencing of IGFBP-3 significantly promotes metastatic potential of HNSCC and NSCLC cells, demonstrated in serial animal experiments. Strikingly, IGFBP-3 regulates the expression of an EMT marker-vimentin in an IGF-independent manner. IGFBP-3 directly binds to vimentin and decreases its protein stability through the ubiquitin-dependent proteasome pathway by recruiting the E3 ligase FBXL14. Moreover, this chapter demonstrates that the C-terminal of IGFBP-3 and the head domain of vimentin are critical for their interaction. Together, chapter 1 highlights IGFBP-3 as a novel strategy for HNSCC and NSCLC metastasis.

Although chemoradiation therapy is the cornerstone of NSCLC treatment, patients often develop drug resistance, tumor relapse after long-term treatment. Cancer stem cells (CSC), a subpopulation of tumor cells, contribute to anticancer drug resistance and tumor relapse in various cancer, including NSCLC. Thus targeting CSC appears to be an effective strategy for anticancer treatment. Chapter 2 of this study demonstrates the inhibitory effects of panaxynol, a natural compound isolated from the non-saponin fraction from *Panax ginseng* (*P. ginseng*), on cancer-stem and non-stem cells in NSCLC. Panaxynol inhibits the viability by inducing apoptosis in both cancer stem and non-stem populations while exhibits minimal toxicity to normal cells. Panaxynol suppresses tumor growth and the tumor-initiating ability in NSCLC xenograft and Kras-driven spontaneous lung tumor models. Together, chapter 2 highlights panaxynol, a natural HSP90 inhibitor, effectively targets both CSC and non-CSC populations in NSCLC.

In summary, the study provides promising therapeutic strategies for aerodigestive tract cancer metastasis by utilizing IGFBP-3 and the cancer stemness by panaxynol- a natural HSP90 inhibitor in NSCLC.

**Keywords:** Insulin-like growth factor binding protein-3, vimentin, metastasis, heat shock protein 90, panaxynol, cancer stem cells.

**Student number: 2013-22582**

# LIST OF CONTENTS

ABSTRACT .....	I
LIST OF CONTENTS.....	III
LIST OF FIGURES .....	VII
LIST OF TABLES .....	X
LIST OF ABBREVIATIONS .....	XI
I. CHAPTER 1 .....	1
INSULIN-LIKE GROWTH FACTOR BINDING PROTEIN-3 EXERTS THE ANTIMETASTATIC EFFECT IN AERODIGESTIVE TRACT CANCER BY DISRUPTING THE PROTEIN STABILITY OF VIMENTIN .....	1
1. INTRODUCTION .....	2
<i>Aerodigestive tract cancer</i> .....	3
<i>Cancer metastasis</i> .....	4
<i>Epithelial-mesenchymal transition (EMT)</i> .....	6
<i>Vimentin</i> .....	8
<i>Insulin-like growth factor binding protein-3 (IGFBP-3)</i> .....	9
2. PURPOSE OF STUDY.....	14
3. MATERIAL AND METHODS .....	16
<i>Reagents</i> .....	17
<i>Cell culture</i> .....	17
<i>Plasmid and siRNA, shRNA</i> .....	18
<i>Transfections</i> .....	18
<i>Cell proliferation assay</i> .....	19
<i>Scratch assay</i> .....	19
<i>Migration and invasion assay</i> .....	19
<i>Immunofluorescence staining</i> .....	20

<i>Aldehyde dehydrogenase assay</i> .....	21
<i>Sphere forming assay</i> .....	21
<i>Western blot analysis</i> .....	21
<i>Immunoprecipitation</i> .....	22
<i>Pull-down assay</i> .....	22
<i>In vitro binding assay</i> .....	23
<i>Real-time polymerase chain reaction</i> .....	23
<i>Animal experiments</i> .....	24
<i>Statistics</i> .....	25
4. RESULTS .....	29
<i>IGFBP-3 inhibits the migratory and invasive potential of HNSCC and NSCLC cells by suppressing EMT phenotypes</i> .....	30
<i>IGFBP-3 suppresses HNSCC and NSCLC metastasis in vivo</i> .....	40
<i>IGFBP-3 downregulates vimentin protein expression in an IGF-independent manner</i> .....	47
<i>IGFBP-3 regulates the stabilization of vimentin protein</i> .....	52
<i>The C-terminal domain of IGFBP3 and the head domain of vimentin are critical for their interaction</i> .....	58
<i>IGFBP-3 induces vimentin protein destabilization through the ubiquitin-dependent-proteasome pathway by mediating the complex between vimentin and the F-box E3 ubiquitin ligase FBXL14</i> ...	62
5. DISCUSSION .....	66
6. CONCLUSION .....	71
II. CHAPTER 2 .....	74
THE DEVELOPMENT OF A NATURAL HSP90 INHIBITOR TARGETING BOTH CANCER STEM AND NON-STEM POPULATIONS IN NON-SMALL CELL LUNG CANCER .....	74
1. INTRODUCTION .....	75
<i>Cancer stem cells (CSCs)</i> .....	76
<i>Heat shock protein 90 (HSP90)</i> .....	78
<i>Panax ginseng</i> .....	81

2. PURPOSE OF THE STUDY.....	82
3. MATERIALS AND METHODS.....	84
<i>Reagents</i> .....	85
<i>Cell culture</i> .....	85
<i>MTT assay</i> .....	86
<i>Sphere formation assay</i> .....	86
<i>Aldehyde dehydrogenase (ALDH) assay</i> .....	87
<i>Anchorage-dependent colony-formation assay</i> .....	87
<i>Soft agar colony formation assay</i> .....	87
<i>Cell cycle analysis</i> .....	88
<i>Tube formation assay</i> .....	88
<i>Western blot analysis</i> .....	88
<i>RT-PCR</i> .....	89
<i>Reporter gene assay</i> .....	89
<i>Transfection</i> .....	89
<i>Immunoprecipitation and pull-down assay</i> .....	90
<i>Animal experiments</i> .....	90
<i>In vivo serial dilution tumor-propagating assay</i> .....	91
<i>Immunofluorescence staining</i> .....	92
<i>Statistics</i> .....	92
4. RESULTS.....	94
<i>Panaxynol is the active compound isolated from the non-saponin fraction of P. ginseng that suppresses the viability and sphere-forming ability of NSCLC cells.</i> .....	95
<i>Panaxynol suppresses the function of HSP90 in NSCLC cells.</i> .....	101
<i>Panaxynol inhibits both the CSC and non-CSC population of NSCLC by inducing apoptosis.</i> .....	107
<i>Panaxynol suppresses NSCLC tumor growth in vivo.</i> .....	121
5. DISCUSSION.....	127
6. CONCLUSION.....	131

III. SUMMARY.....	132
IV. REFERENCES .....	134
ACKNOWLEDGEMENT .....	142

# LIST OF FIGURES

FIGURE 1-1: THE METASTATIC CASCADES .....	5
FIGURE 1-2. THE EMT PROGRAM .....	7
FIGURE 1-3. THE PROPOSED ANTITUMOR MECHANISM OF IGFBPS .....	11
FIGURE 1-4. THE STRUCTURE AND CELLULAR DISTRIBUTION OF IGFBP-3 .....	13
FIGURE 1-5. THE IGFBP-3 EXPRESSION IN HNSCC CELL LINES.....	33
FIGURE 1-6. THE EFFECT OF IGFBP-3 ON THE PROLIFERATIVE, MIGRATORY AND INVASIVE POTENTIAL OF NSCLC AND HNSCC CELLS. ....	35
FIGURE 1-7. IGFBP-3 REGULATES EMT MARKERS EXPRESSION IN HNSCC CELLS. ....	36
FIGURE 1-8. THE EFFECT OF IGFBP-3 ON TGF-B- INDUCED MIGRATORY PHENOTYPES IN HNSCC AND NSCLC CELLS.....	37
FIGURE 1-9. THE EXPRESSION OF EMT MARKERS IN H226B-SHEV AND H226B-SHBP3 XENOGRAFT TUMORS .....	38
FIGURE 1-10. IGFBP-3 INHIBITS CSC PROPERTIES IN HNSCC AND NSCLC CELLS. ....	39
FIGURE 1-11. THE ANTIMETASTATIC ACTIVITY OF IGFBP-3 IN THE SPONTANEOUS HNSCC TUMORIGENESIS MODEL.....	43
FIGURE 1-12. THE ANTIMETASTATIC ACTIVITY OF IGFBP-3 IN THE HNSCC ORTHOTOPIC MOUSE MODEL. ....	44
FIGURE 1-13. THE ANTIMETASTATIC ACTIVITY OF IGFBP-3 IN THE NSCLC XENOGRAFT MOUSE MODEL ...	46
FIGURE 1-14. IGFBP-3 DOWNREGULATES VIMENTIN EXPRESSION. ....	49
FIGURE 1-15. THE REVERSE CORRELATION BETWEEN IGFBP-3 AND VIMENTIN EXPRESSION IN H226B-SHEV XENOGRAFT TUMOR. ....	50
FIGURE 1-16. IGFBP-3 REGULATES VIMENTIN EXPRESSION IN AN IGF-INDEPENDENT MANNER .....	51

FIGURE 1-17. IGFBP-3 REGULATES VIMENTIN STABILITY THROUGH THE UBIQUITIN-DEPENDENT PROTEASOME PATHWAY.....	55
FIGURE 1-18. IGFBP-3 INTERACTS WITH VIMENTIN IN HNSCC CELLS.....	57
FIGURE 1-19. THE C-TERMINAL DOMAIN OF IGFBP-3 IS CRITICAL FOR THE INTERACTION WITH VIMENTIN. .....	60
FIGURE 1-20. THE HEAD DOMAIN OF VIMENTIN IS CRITICAL FOR THE BINDING WITH IGFBP-3 .....	61
FIGURE 1-21. VIMENTIN EXPRESSION IN CELLS WITH SIRNAS MEDIATED-F-BOX PROTEINS SILENCING. ....	64
FIGURE 1-22. IGFBP-3 INDUCES UBIQUITIN-MEDIATED VIMENTIN DEGRADATION BY RECRUITMENT OF THE E3 LIGASE FBXL14. ....	65
FIGURE 1-23. THE SCHEMATIC MODEL OF THE ANTIMETASTASIS MECHANISM OF IGFBP-3 .....	73
FIGURE 2-1. THE MARKERS OF CANCER STEM CELLS .....	77
FIGURE 2-2. THE STRUCTURE AND CONFORMATIONAL CHANGES OF HSP90.....	80
FIGURE 2-3. THE NON-SAPONIN FRACTION OF <i>P. GINSENG</i> DISRUPTS THE HSP90 FUNCTION AND VIABILITY OF BOTH NON-CSC AND CSCS.....	97
FIGURE 2-4. THE EFFECTS OF THE <i>P.GINSENG</i> NON-SAPONIN FRACTION ON LUNG TUMORIGENESIS. ....	99
FIGURE 2-5. THE INHIBITORY EFFECT OF SIX NON-SAPONIN SUB-FRACTIONS ON H1299'S CELL VIABILITY. .....	100
FIGURE 2-6. PANAXYNOL SUPPRESSES HSP90 FUNCTION IN NSCLC CELLS. ....	103
FIGURE 2-7. PANAXYNOL SUPPRESSES HRE ACTIVITY AND TUBE FORMATION OF HUVEC CELLS.....	104
FIGURE 2-8. PANAXYNOL TREATMENT DOES NOT ALTER HSP70 EXPRESSION. ....	105
FIGURE 2-9. THE EFFECT OF PANAXYNOL ON THE SPHERE-FORMING ABILITY AND ANCHORAGE- DEPENDENT-COLONY FORMATION IN H1299SHEV AND SHHSP90 CELLS. ....	106
FIGURE 2-10. PANAXYNOL INHIBITS NSCLC CSC POPULATIONS.....	110

FIGURE 2-11. PANAXYNOL INHIBITS NSCLC CELLS IN SPHERE CULTURE CONDITIONS AND ALDH ACTIVITY OF H1299 CELLS .....	112
FIGURE 2-12. PANAXYNOL INDUCES APOPTOSIS IN H1299 CELLS GROWN IN SPHERE-FORMING CONDITIONS. ....	114
FIGURE 2-13. THE EFFECT OF PANAXYNOL ON THE VIABILITY OF HBE CELLS WITH KRAS MUTANT OR P53 LOSS FUNCTION. ....	115
FIGURE 2-14. THE EFFECT OF PANAXYNOL ON THE VIABILITY OF NAÏVE OR ACQUIRED ANTICANCER DRUG RESISTANCE NSCLC CELLS .....	116
FIGURE 2-15. THE EFFECT OF PANAXYNOL ON THE VIABILITY OF NORMAL CELLS. ....	117
FIGURE 2-16. PANAXYNOL SUPPRESSES THE ANCHORAGE-DEPENDENT COLONY-FORMING ABILITY OF NSCLC CELLS.....	118
FIGURE 2-17. PANAXYNOL INDUCES APOPTOSIS IN NSCLC CELLS GROWN IN MONOLAYER CONDITIONS. ....	120
FIGURE 2-18. THE ANTITUMOR ACTIVITIES OF PANAXYNOL ON KRAS <sup>G12D/+</sup> -DRIVEN-SPONTANEOUS LUNG TUMOR FORMATION. ....	124
FIGURE 2-19. THE ANTITUMOR EFFECT OF PANAXYNOL IN THE H1299 XENOGRAFT MODEL.....	126

# LIST OF TABLES

TABLE 1. LIST OF PLASMIDS .....	27
TABLE 2. LIST OF PRIMERS FOR REAL-TIME PCR.....	28
TABLE 3. LIST OF PRIMERS FOR RT-PCR.....	93

## LIST OF ABBREVIATIONS

ALDH	Aldehyde dehydrogenase
ATP	Adenosine triphosphate
CSC	Cancer stem cells
E-cad	E-cadherin
EMT	Epithelial-mesenchymal transition
FBXL14	F-box and leucine-rich repeat protein 14
FBXO1	F-box only protein 1
GST	Glutathione S-transferase
HIF1 $\alpha$	Hypoxia-inducible factor -1 $\alpha$
HNSCC	Head and neck squamous cell carcinoma
HSP90	Heat shock protein 90
IGF	Insulin-like growth factor
IGF-1	Insulin-like growth factor type 1
IGF-1R	Insulin-like growth factor type 1 receptor
IGF2	Insulin-like growth factor type 2
IGFBPs	Insulin-like growth factor binding proteins
IGFBP-3	Insulin-like growth factor binding protein-3
N-cad	N-cadherin
NSCLC	Non-small cell lung carcinoma
TGF $\beta$	Transforming growth factor- $\beta$
Ub	Ubiquitin
VEGF	Vascular endothelial growth factor
VIM	Vimentin

# **I. CHAPTER 1**

**Insulin-like growth factor binding protein-3 exerts the antimetastatic effect in aerodigestive tract cancer by disrupting the protein stability of vimentin**

## **1. INTRODUCTION**

## **Aerodigestive tract cancer**

Aerodigestive tract cancer, including non-small cell lung cancer (NSCLC) and head and neck squamous cell carcinoma (HNSCC), is the leading cause of cancer-related death worldwide [1, 2]. While HNSCC is the upper digestive tract cancer derived from the malignant mucosa epithelium in the oral cavity, pharynx, and larynx that arise in the head and neck, NSCLC is lower digestive tract cancer that accounts for more than 85% of lung cancer. NSCLC comprises three main subtypes, including squamous cell carcinoma, adenocarcinoma, and large cell carcinoma [1]. Chemotherapy and radiation therapy is the cornerstone of these cancers treatment. Generally, the treatment methods are surgery, followed by chemoradiation or target therapies for late-stage patients with tumor recurrence and metastatic disease [3]. However, patients often acquire anticancer drug resistance, tumor relapse, and metastasis after long-term treatment. Ongoing efforts aim to elucidate the most effective therapeutic intervention for patients with HNSCC and NSCLC.

## **Cancer metastasis**

Metastasis, the leading cause of cancer-related death worldwide, is related to poor prognosis and low survival rate in patients with NSCLC and HNSCC [4-7]. In aerodigestive tract cancer, most patients developed metastasis with advanced stages at the time of initial diagnosis. Approximately 15% of HNSCC and 20-40% of NSCLC patients develop metastasis after the initial treatment [3, 8].

Metastasis is the primary tumor cells' movement from the original sites to the secondary organs following several steps [9]: (1) The epithelial cells lose their cell-cell contact, cell adhesion and disassociate others. (2) Consequently, cancer cells acquire more invasive mesenchymal phenotypes, evade the surrounding tissues, and enter the circulation system. (3) The circulating tumor cells (CTCs) travel through the blood system until they reach distant sites. (4) CTCs exit the circulation system and colonize distant tissues. (5) The invaded cells adapt to the microenvironment, proliferate to form micro or macro-metastasis.

However, we still lack knowledge explaining the mechanism of cancer cell migration and invasion, how cancer cells metastasize to specific organs, the dormancy of cancer cells, and the impact of the tumor environment at the secondary sites. Therefore, increased understanding of the metastasis complexity can help develop effective antimetastasis strategies in HNSCC and NSCLC.

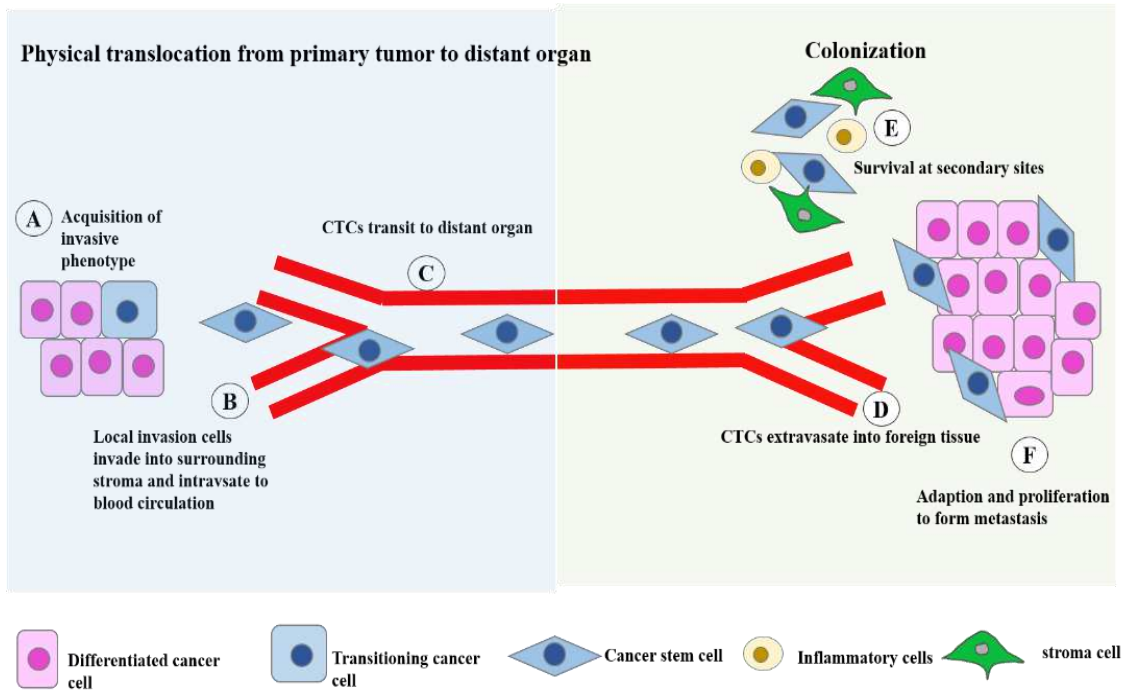


**Figure 1-1: The metastatic cascades**

The metastatic cascade's two primary phases are the physical translocation of cancer cells from the primary site and the colonization of circulating tumor cells in the distant organs.

(A) At the primary site, the epithelial cancer cells undergo EMT to acquire invasive phenotypes. (B) The local invasive cells break through the surrounding tissues and enter the blood circulation. (C) The circulating cancer cells (CTCs) travel in the circulation system. (D) when reaching the distant organs, CTCs exit the circulation and colonize foreign tissues. (E) Cancer cells evade the innate immune surveillance for their survival at distant tissues. (F) Cancer cells adapt to the tumor microenvironment, proliferate, and develop micro and macro-metastasis.

Reference: Chaffer, Christine & Weinberg, Robert. (2011). A Perspective on Cancer Cell Metastasis. *Science* (New York, N.Y.). 331. 1559-64. 10.1126/science.1203543.

### **Epithelial-mesenchymal transition (EMT).**

The epithelial-mesenchymal transition (EMT) and its reverse event mesenchymal-epithelial transition (MET) play an essential role during embryonic development and cancer metastasis [10]. EMT is the transition of cancer cells from the epithelial to mesenchymal phenotypes. By acquiring the mesenchymal phenotypes, primary cancer cells lose their cell contact and increase motility, favoring their dissemination and invasion. Thus, EMT has been considered as the initial steps of cancer metastasis. On the other hand, the reverse process MET, the transition of mesenchymal cells to the epithelial state, has been the essential step for metastasis after cell dissemination at the distant sites.

EMT induces the downregulation of epithelial markers such as E-cadherin, Occludin, and upregulation of mesenchymal markers such as N-cadherin, vimentin, and fibronectin. The EMT program is regulated by EMT transcription factors, including the ZEB family, Snail, Slug, and Twist. Snail and ZEB1 repress E-cadherin's expression and upregulate vimentin and N-cadherin's expression through modulation of these genes promoter activation. Snail and ZEB1 can also upregulate matrix metalloproteinases (MMPs) expression, which induces the basement membrane's degradation and promotes cell invasion [11]. Accumulating evidence revealed EMT is induced by signaling pathways such as Wnt, Notch, and TGF $\beta$  or growth factors secreted from the tumor environment's components [11]. Several studies reveal the link between EMT and cancer stemness. Activation of EMT by overexpression EMT-TF or TGF $\beta$  increases populations with CSC properties [12, 13], whereas CSC from several carcinomas displays the EMT phenotypes [14]. EMT has been proposed to contribute to tumor progression, therapeutic drug resistance, invasion, and metastasis; therefore, targeting EMT appears to be an effective option to cure and prevent metastasis.

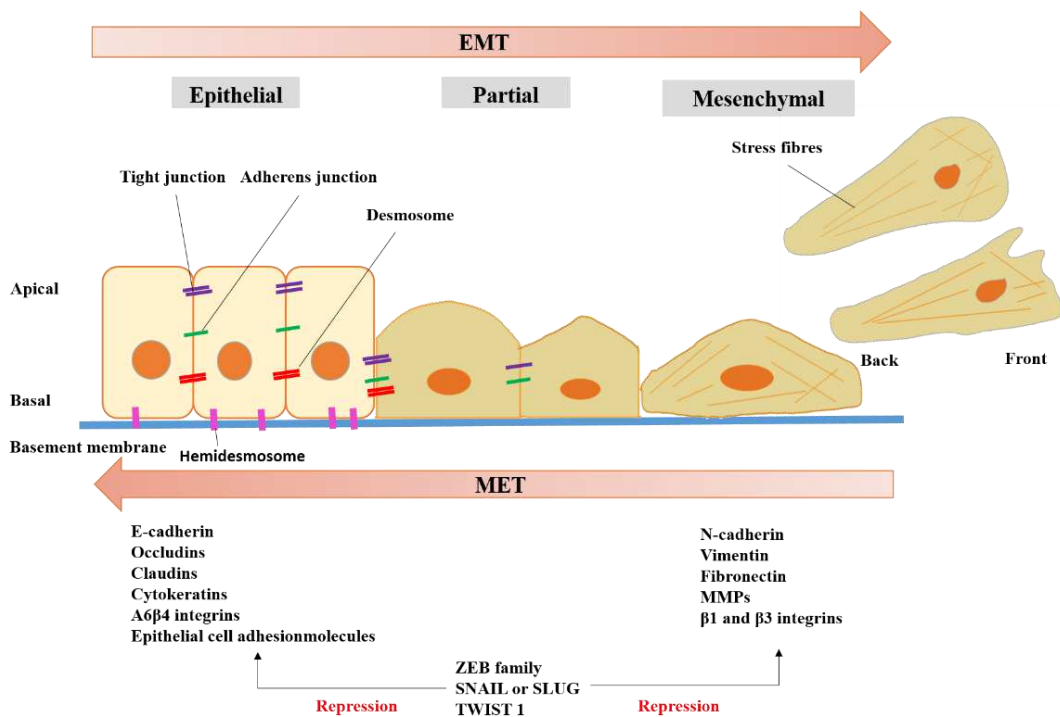


**Figure 1-2. The EMT program**

The EMT (epithelial-mesenchymal transition) and the reverse process MET is essential for cell migration and metastasis. Cell interactions are maintained by tight, adherent, basal-apical, and desmosomes junctions. Cancer cells undergoing EMT lose their cell-cell contact and acquire mesenchymal phenotypes, promoting migration and cancer metastasis. During EMT, mesenchymal markers such as N-cadherin, vimentin, and fibronectin were upregulated, while epithelial markers (E-cadherin, occludin, claudin...) were downregulated. Transcription factors such as Twist, Slug, Snail, ZEB regulate the EMT process by inhibiting or activating the EMT-related genes.

Reference: Dongre, A., Weinberg, R.A. New insights into the mechanisms of epithelial–mesenchymal transition and implications for cancer. *Nat Rev Mol Cell Biol* **20**, 69–84 (2019).

## **Vimentin**

Vimentin is the intermediate filament that plays a crucial role in maintaining cytoskeleton structure and cell integrity [15]. Vimentin is highly expressed in mesenchymal cells and is considered a canonical marker of EMT. Overexpression of vimentin has been observed in various tumor types, including NSCLC and HNSCC, correlates with tumor aggressiveness and poor patient outcomes [16-19].

During the EMT, vimentin is sufficient to induce morphological changes to more mesenchymal-like states, enhance motility and cell-adhesion [20]. The silencing of vimentin suppresses the migratory and invasive capacities of NSCLC and oral squamous carcinoma cells [21, 22]. Additionally, vimentin implicates in the signaling pathways associated with EMT and migration. Vimentin is crucial for Erk-Slug mediating cancer cell migration and invasion [23]. Induction of vimentin by TGF $\beta$  or Snail potentiates cancer cell migration [15, 24].

The role of vimentin on HNSCC and NSCLC metastasis has been described previously. High vimentin expression has been observed in metastatic oral squamous carcinoma cell lines and correlated with lymph node metastases [18]. Among the 5 EMT markers, vimentin has been considered the most potential prognostic factor for tongue squamous cell carcinoma [19]. High vimentin expression is correlated with poor survival rate, advanced TNM stages, and lymph node metastasis in patients with HNSCC and NSCLC [17, 19, 22]. Recently, vimentin promotes metastasis by modulation of the tumor microenvironment. Loss of vimentin did not affect primary tumors but suppress lymph node metastasis in lung adenocarcinoma [25]. Strikingly, vimentin is not present in the invading cancer cells but in the tumor-associated fibroblast surrounding the invasive pack [25]. Based on the accumulating evidence demonstrating the role of vimentin on EMT, invasion, and metastasis, vimentin could be a potential target for metastasis treatment.

### **Insulin-like growth factor binding protein-3 (IGFBP-3)**

The insulin-like growth factor (IGF) axis plays an essential role in the proliferation and survival of normal and malignant tissues [26]. The IGF axis comprises the two ligands insulin-like growth factors (IGF-1 and IGF-2), the two IGF receptors (IGF-1R and IGF-2R), and insulin-like growth factor-binding proteins. The ligand IGFs primarily form the complexes with the (IGF-1R), leading to the activation of intrinsic oncogenic pathways PI3K/ AKT and RAS/MAPK.

The (IGFBPs) family composes of 6 members (IGFBP-1 to IGFBP-6). IGFBPs could bind to IGFs with high affinity than the IGF1, form ternary complexes with IGFs, increase the half-life of IGFs in the circulation, and sequester IGFs from the IGF-1R receptor. Therefore, by regulating the IGFs bioavailability, IGFBPs suppress the downstream signaling of the IGF axis. IGFBPs have been considered tumor suppressors [27], and the proposed growth inhibitory mechanism of IGFBPs was demonstrated in Figure 1-3.

Among IGFBPs, IGFBP-3 is the predominant form found in the circulation. IGFBP-3 comprises three domains: the N-, M- and C-terminal domains that contain several functional motifs essential for IGFBP-3 modifications. Both the N- and C-terminal domain of IGFBP-3 contains the binding site for IGFs. The N-terminal domain contains motifs responsible for the binding with nuclear proteins and IGFBP-3 transactivation; the M-terminal domain contains motifs essential for the modifications of IGFBP-3; the C-terminal domain contains the nuclear localization sequence (NSL), ECM, and cell surface binding motifs. IGFBP-3 is a secreted protein and functions extracellularly but can be internalized into the cells and transported in the nucleus. IGFBP-3 binds to other non-IGF components in the extracellular matrix (ECM), cellular membrane (LRP-1, transferrin, transferrin receptor...), and nucleus (RAR $\alpha$ , RXR $\alpha$ , Nur77....) [28, 29] to exert its IGF-independent functions [27]. The interaction with low-density lipoprotein receptor-related protein 1

(LRP-1) is essential for the IGFBP-3 uptake, leading to growth inhibition [30]. IGFBP-3 possesses the nuclear localization sequences and can translocate into the nucleus through importin  $\beta$  [31]. Intracellular IGFBP-3 interacts with nuclear receptors RAR $\alpha$ , RXR $\alpha$  and mediates their signaling in the nucleus. IGFBP-3 induces intrinsic apoptosis in prostate cancer cells through binding with the orphan nuclear receptor Nurr77 [32].

IGFBP-3 functions as a tumor suppressor and is downregulated in several carcinomas. The low IGFBP-3 expression is frequently associated with poor prognosis. Previous prognostic studies revealed that the low expression of IGFBP-3 correlates with low disease-specific and overall survival, poor prognosis, and metastasis in patients with early-stage of NSCLC and esophageal cancer [33-35]. IGFBP-3 induces apoptotic events in prostate and lung cancer cells without modulating the IGF1R activation [36, 37]. IGFBP-3 has also been reported to possess antiangiogenic, antitumor, antimetastatic activities in several cancer types [38-42]. IGFBP-3 regulates Erg1-mediated transcriptional activities [43] and suppress cell adhesion through integrin signaling downregulation [39]. Although IGFBP-3 has been considered the metastasis suppressor in the prostate, lung, and endometrioid ovarian carcinoma [40, 44, 45], the effects of IGFBP-3 on HNSCC and NSCLC metastasis and its underlying mechanism remains unknown.

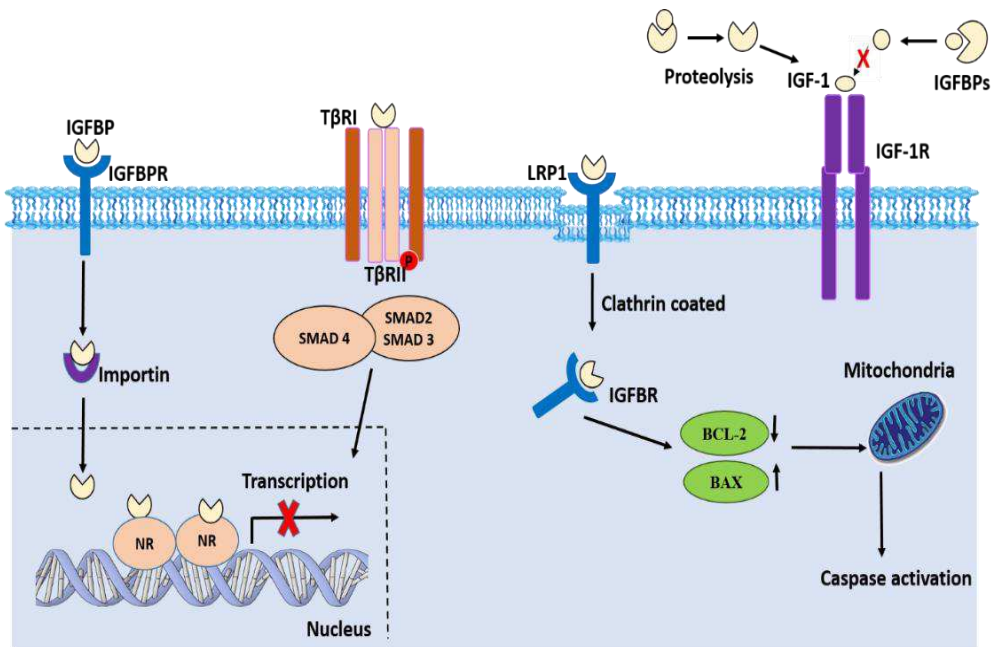
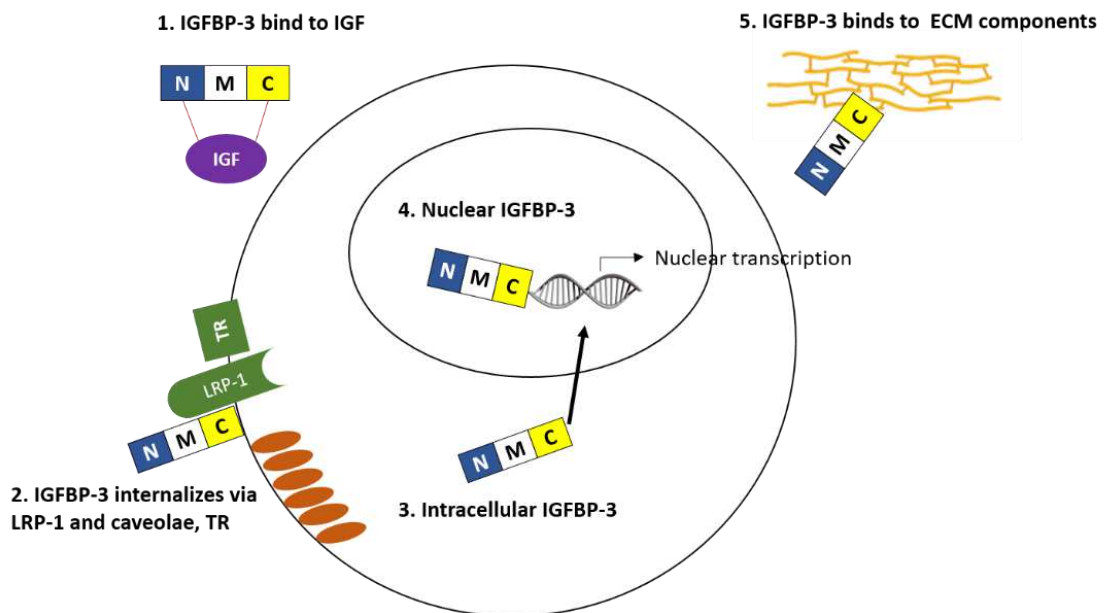


**Figure 1-3. The proposed antitumor mechanism of IGF-BPs**

IGFBPs mediates cellular functions via multiple mechanisms. 1). IGFBPs bind to IGF-1 and IGF-2 to sequester them from IGF-1R results in the suppression of the IGF-axis's downstream signalings. The binding capacity of IGFBPs with IGFs can be decreased by IGFBPs proteolysis. 2). The interaction with cell-surface proteins such as LRP-1, caveolin can promote IGFBPs internalization. Intracellular IGFBPs interact with their corresponding receptors and trigger the proapoptotic events. 3). IGFBPs bind to TGF $\beta$  receptors, resulting in Smad4, Smad2, Smad3 complex activation, eventually trigger the inhibitory TGF $\beta$  signaling. 4). IGFBPs transport into the nucleus by importin  $\beta$ , interact with nuclear proteins (RAR $\alpha$ , RXR $\alpha$ ), and regulate the nuclear-dependent transcriptional activity.

Reference: Baxter, R. IGF binding proteins in cancer: mechanistic and clinical insights. *Nat Rev Cancer* **14**, 329–341 (2014). <https://doi.org/10.1038/nrc3720>



N-terminal domain	M-terminal domain	C-terminal domain
<ol style="list-style-type: none"> <li>1. IGF binding motif</li> <li>2. Residues involve in RXR<math>\alpha</math> and RAR<math>\alpha</math> interaction</li> <li>3. Functional transactivation domain</li> </ol>	<ol style="list-style-type: none"> <li>1. Heparin binding sequence</li> <li>2. Modification sites: glycosylation, phosphorylation....</li> </ol>	<ol style="list-style-type: none"> <li>1. IGF binding motif</li> <li>2. NSL sequence</li> <li>3. Heparin/ glycosaminoglycan binding domain</li> <li>4. ECM, cell surface binding motifs</li> <li>5. RXR<math>\alpha</math> and RAR<math>\alpha</math> interaction motifs</li> </ol>

#### **Figure 1-4. The structure and cellular distribution of IGFBP-3**

The structure of IGFBP-3 contains three regions: the N-, M- and C- terminal domains. The N-terminal domain of IGFBP-3 contains motifs responsible for IGF binding, RXR $\alpha$ -RAR $\alpha$  interaction, and the transactivation of IGFBP-3. The M-terminal domain contains several sites for post-translational modifications. The C-terminal domain contains sequences responsible for the IGF-binding, nuclear translocation, Heparin-binding site, and the interaction with ECM components of IGFBP-3. 1) IGFBP-3 binds to IGFs by both N- and C- terminal domains, resulting in IGF sequestration. 2) IGFBP-3 endocytosis is mediated through its interaction with caveolin-1, transferrin, and transferrin receptor. IGFBP-3 can be internalized via interaction with cell surface protein LRP-1. 3) Intracellular IGFBP-3 interacts with its specific receptor and other cellular partners to mediate intracellular signalings. 4) IGFBP-3 interacts with importin  $\beta$  and translocates into nuclear wherein it binds to nuclear receptors (RAR $\alpha$ , RXR $\alpha$ ...) and regulates the nuclear-dependent transcription. 5) C-terminal domain of IGFBP-3 attaches to the extracellular matrix (ECM) components (fibrin, latent transforming growth factor binding protein-1...).

Reference: Yamada, Paulette & Lee, Kuk-Wha. (2009). Perspectives in Mammalian IGFBP-3 Biology: Local vs. Systemic Action. American journal of physiology. Cell physiology. 296. C954-76. 10.1152/ajpcell.00598.2008.

## **2. PURPOSE OF STUDY**

Metastasis, the leading cause of death in aerodigestive tract cancer, is associated with poor prognosis and patient outcomes. In metastatic cascades, cancer cells initially acquire EMT phenotypes, increase cell motility to break through the surrounding tissue, and then experience several steps to translocate from the primary to the favorable secondary sites. The circulating tumor cells colonize distant organs, develop micro and macro metastasis. However, there is still a lack of available antimetastasis treatments due to the complexity of metastasis biology. Therefore, understanding the mechanism of metastasis progression and developing a novel strategy is urgently needed.

Although the antimetastatic effect of IGFBP-3 has been supposed in several human malignancies, the role of IGFBP-3 on EMT and metastasis in aerodigestive tract cancers remains unknown.

Thus, this study investigates the antimetastatic role of IGFBP-3 in HNSCC and NSCLC and the underlying mechanism of these events.

### **3. MATERIAL AND METHODS**

## **Reagents**

Antibodies against E-cadherin, N-cadherin, Fibronectin were purchased from BD Bioscience (San Jose, CA, USA). Antibodies against IGFBP-3 and vimentin, Ubiquitin, GST, HA, and actin were purchased from Santa Cruz Biotechnology (Dallas, TX, USA). Antibodies against IGF1-R, tubulin were purchased from Cell Signalling Technology (Danvers, MA, USA). The horseradish peroxidase (HRP-) conjugated secondary antibodies were purchased from GeneTex (Irvine, CA, USA). Fluorochrome Alexa Fluor 488, Alexa Fluor 546, and Alexa Fluor 594 were purchased from Thermo Fisher Scientific (Waltham, MA, USA).

Recombinant IGFBP-3 was purchased from R&D Systems (Minneapolis, USA). G418 was purchased from Enzo Life Science. Puromycine and MG132 were purchased from Sigma Aldrich (St. Louis, MO, USA).

## **Cell culture**

Human HNSCC cell lines (UMSCC38, UMSCC1, UMSCC14A, UMSCC4, and OSC19-Luc) were kindly provided by Dr. Jeffrey N. Myers (MD Anderson Cancer Center, Houston, TX, USA). The human NSCLC cell line H226B was kindly provided by Dr. John V. Heymach (MD Anderson Cancer Center, Houston, TX, USA). The human HNSCC cell line Fadu, the human NSCLC cell line H1299, and the human embryonic kidney 293T cell line (HEK293T) were purchased from the American Type Culture Collection (ATCC, USA). UMSCC1, UMSCC14A, UMSCC4, OSC19-Luc, Fadu cells were cultured in Dulbecco's modified Eagle's medium (DMEM). UMSCC38 cells were cultured in the Dulbecco's modified Eagle's medium nutrient mixture F-12 (DMEM-F/12), and H1299, H226B cells were cultured in RPMI-1640 medium with 10% fetal bovine serum (FBS) and 1% antibiotic (WeiGENE, Kyeongsan-si, Korea). All cells were maintained in the humidified incubator with 5% CO<sub>2</sub> at 37°C.

### **Plasmid and siRNA, shRNA**

The expression plasmids of full-length IGFBP-3 (pCMV6 IGFBP-3), full-length vimentin (pCMV-Tag2B-vimentin) were previously generated in our laboratory. The expression plasmids of the N-, M-, and C-terminal domains of IGFBP-3 were generated by cloning the IGFBP-3 domains sequence into the pCDNA 3.1 vector.

The bacterial plasmids of His-tagged full-length (FL) IGFBP-3 and its domains were generated by cloning FL-IGFBP-3, N-IGFBP-3, M-IGFBP-3, C-IGFBP-3 into the pET32a vector. The pEGFP-C1 vimentin was kindly provided by Dr. Dale D. Tang (Albany Medical College, Albany, NY, USA). The bacterial plasmid for GST-tagged vimentin was generated by subcloning pEGFP-C1 vimentin into the pGEX-4T2 vector (GE Healthcare Life Science, Chicago, IL, USA). The bacterial plasmids of the head (1-101), coiled-coil (102-410), tail domain (411-467), and domain-deletion mutants of vimentin ( $\Delta$ head,  $\Delta$ coiled-coil,  $\Delta$ -tail) were generated in our laboratory by cloning their sequence into the pGEX-4T2 vector. The mCherry-Cyclin F (FBXO1) was a present from Michele Pagano (Addgene plasmid #32975) (Addgene, Watertown, MA, USA). shRNAs for silencing IGFBP-3, IGF-1R, and pLKO.1 puro empty vectors were purchased from Open Biosystems (Thermo Fisher Scientific) and Sigma Aldrich. The siRNAs for silencing E3 ligases ( FBXO1, FBX04, FBX09, FBX15, FBX32, FBX41, FBXL6, FBXL12, FBXL14, FBXW7, FBXW8) were kindly provided by Dr. Su Jae Lee (Hanyang University, Korea).

### **Transfections**

For the transient transfection, we used the transfection reagents JetPRIME (Polyplus transfection, Illkirch, France), Fugene 6 (Promega, Madison, WI, USA), and Lipofectamine 2000 (Thermo Fisher Scientific) according to the manufacture's instructions.

To generate the stable knockdown of IGFBP-3 and IGF-1R cell lines, we first generated the lentivirus supernatants by transfecting the empty vector (PLKO.1 shEV), shIGF-1R, shIGFBP-3, lentiviral packaging (pHR8.2deltaR), and envelope plasmids (pCMV-VSV-G) into the HEK293T cells using Fugence 6. After 24-48 hours of transfection, the lentiviral supernatants were collected and filtered using the 0.22  $\mu$ m syringe. Next, the shEV, shIGFBP-3 lentiviral supernatants were transduced into the UMSCC38, UMSCC1, H226B cells, or shIGF-1R lentiviral supernatant was transduced into UMSCC38, H1299 cells in the medium containing 8  $\mu$ g/ml polybrene for 24 hours. The cells were then selected with 1-2  $\mu$ g/ml puromycin for 2-3 weeks.

To generate cell lines with IGFBP-3 overexpression, we transfected the IGFBP-3 expressing vector (pCMV6 EV and pCMV6 IGFBP-3) to H1299, OSC19-Luc cells using the transfection reagent- JetPRIME. The cells were then maintained and selected by G418.

### **Cell proliferation assay**

The indicating cells ( $5 \times 10^4$ /well) were seeded in 24-well plates. The cell's number in each well at different time points was calculated using the hemocytometer.

### **Scratch assay**

Cells were seed into 6-well plates until reaching the confluence. We used the 200  $\mu$ l sterile plastic tips to create the scratches. Subsequently, cells were washed with PBS to remove the floating cells. The scratches' images were photographed at the start point and different indicated time points using the EVOS FL Cell Imaging System (Thermo Fisher Scientific) until the cells completely cover the scratch areas. The scratch distances were measured using ImageJ software (National Institutes of Health, Bethesda, MD, USA).

### **Migration and invasion assay**

For the migration assay, the transwell's outer membrane (8 $\mu$ m, Corning Inc, NY, USA) was coated with 15  $\mu$ l of 0.05% gelatin.  $2 \times 10^4$  cells were seed into the transwell insert in

free serum medium. The mixture of 10% serum medium with NIH3T3 supernatant (ratio 1:1) was added to the lower chamber. Cells were incubated for about 12-24 hours in the humidified incubator, and the incubation time depends on cell types. The cells were then fixed with methanol at room temperature (RT) for 10 minutes, stained with hematoxylin for 8 minutes, eventually washed with PBS and distilled water several times. Cells on the inner surface were removed using the cotton swab. The membranes were cut and dipped into the xylene solution and subsequently mounted onto a microscope slide. The migrated cells were visualized using a microscope (Nikon Eclipse 80i, Nikon Instrument Inc, Tokyo, Japan).

For the invasion assay, the outer membrane was coated with 0.015% gelatin, and the inner membrane was coated with Matrigel (BD Bioscience). The following steps were similar to the migration assay except that cells were incubated for 18-36 hours at 37°C.

### **Immunofluorescence staining**

Cells were cultured on the glass coverslips in the 24 well-plate and then fixed with methanol for 10 minutes in RT. Cells were then incubated with 0.3% Triton X-100 for 10 minutes for permeabilization and then washed with TBS containing 0.025% Triton X-100 (TBST). Subsequently, cells were blocked with 10% normal serum diluted in 3% BSA and then incubated with anti-IGFBP-3, anti-vimentin, anti-N-cadherin, anti-E-cadherin antibodies (1:400 dilution) at 4°C overnight. After washed with TBST, cells were incubated with fluorochrome-conjugated secondary antibodies (Alexa Fluor 488, Alexa Fluor 546, Alexa Fluor 594) (1:1000 dilution) for 1 hour in RT. Eventually, cells were washed, stained with 4',6-diamino-2-phenylidole (DAPI) solution, and mounted onto the glass slides using the fluorescence mounting solution. The fluorescence images were visualized using the fluorescent microscope (Zeiss Axio Observer Z1, Carl Zeiss AG, Oberkochen, Germany).

### **Aldehyde dehydrogenase assay**

The ALDH activity of cancer cells was determined using the AldeRed assay kit (Merck KgaA, Darmstadt, Germany). Each group contains the test sample (without DEAB) and the DEAB sample. In both samples, cells were resuspended into AldeRed buffer and stained with the fluorescent dye AldeRed A-588. The DEAB samples are used as a negative control, in which we added the ALDH inhibitor- N, N-diethylaminobenzadehyde (DEAB). All the samples were incubated at 37<sup>0</sup>C for 40 minutes. Cells were washed and resuspended in AldRed buffer. The ALDH<sup>high</sup> population was determined by flow cytometry (BD Bioscience). The fluorescence baseline in each group was set based on the corresponding DEAD sample using Flowing Software (Turku Bioscience Center).

### **Sphere forming assay**

Cells were seeded in the low-attachment 96-well plate (Corning Inc) and cultured in the sphere medium containing DMEM-F/12, B27 supplements (Thermo Fisher Science), basic fibroblast growth factor (bFGF), epidermal growth factor (EGF), and 1% antibody. Cells were incubated at 37°C and 5% CO<sub>2</sub> until the spheres' size is above 150 μm<sup>3</sup>.

### **Western blot analysis**

After washed with cold PBS, the cells were lysed in RIPA buffer containing 50mM Tris-HCl (pH 8.0), 150 nM NaCl, 1% Triton X-100, 1% sodium deoxycholate, 0.1% SDS, 1 mM EDTA, and protease and phosphatase inhibitor cocktail (Roche, Manheim, Germany). Cell lysates were collected by centrifugation at 13000 rpm, and protein concentration was determined using the BCA assay kit (Thermo Fisher Scientific). The proteins were segregated by sodium dodecyl sulfate-polyacrylamide gel electrophoresis (SDS-PAGE) and transferred onto the polyvinylidene difluoride (PVDF) membranes. The membranes were blocked with a blocking solution (3% BSA in TBST) for 1 hour at RT, followed by primary antibody incubation (1:1000 dilution) in 3% BSA at 4°C overnight. After three

times washed with TBST, membranes were incubated with HRP-conjugated secondary antibodies diluted (1:5000) in the blocking solution (3%BSA in TBST) for 1 hour RT. The membrane was then washed three times with TBST, and the protein signal was visualized with SuperSignal West Femto chemiluminescent substrates (Thermo Fisher Scientific) using the ImageQuant LAS4000 system (GE healthcare).

### **Immunoprecipitation**

After washed with cold PBS, the cells were lysed in EBC lysis buffer containing 50mM Tris-HCl (pH 8.0), 120 nM NaCl, 0.5% NP-40, 1 mM EDTA, and protease and phosphatase inhibitor cocktail (Roche, Mannheim, Germany). The cell lysates were collected by centrifuging, and the protein concentration was determined using the BCA assay kit (Thermo Fisher Scientific). 0.7-1mg of cell lysates were incubated with 1 $\mu$ g of primary antibodies in 1.5ml microtubes followed by overnight rotation at 4°C. The total volume of IP reaction is 1ml. Subsequently, 20  $\mu$ l Protein A agarose (Merck KGaA, Darmstadt, Germany) was added to each microtube, and the IP reaction was gently rotated for 2 hours. The immunoprecipitants were washed three times with EBC buffer, boiled in 5X sample buffer, and eventually subjected to western blot analysis.

### **Pull-down assay**

The glutathione-S-transferase (GST) - tagged vimentin protein bound to the glutathione beads or the hexahistidine (6His, His)- tagged IGFBP-3 protein bound to the Ni-NTA beads were incubated with 1mg of cell lysates in the microtubes overnight at 4°C. The pull-down complexes were collected by centrifuging at 13000 rpm for 30 seconds, washed three times with cold EBC lysis buffer, boiled in 5X sample buffer, and subjected to western blot analysis.

### **In vitro binding assay**

The glutathione-S-transferase (GST) - tagged vimentin protein bound to the glutathione beads or the hexahistidine (6His, His)- tagged IGFBP-3 protein bound to the Ni-NTA beads were incubated with the recombinant IGFBP-3 or recombinant vimentin proteins respectively in TNE buffer containing 50 nM Tris-HCl (pH 8.0), 120 nM NaCl, 0.1M EDTA) in 1.5 ml microtubes for 2 hours at 4°C. The binding complexes were pulled down, washed three times with cold TNE buffer, and then subjected to SDS-PAGE and western blot analysis.

### **Real-time polymerase chain reaction**

The total RNA was extracted using the Transcripts first-strand cDNA synthesis kit (Transgen Biotech, Beijing, China) with the oligo(dT)<sub>18</sub> primer. For RT-PCR, the PCR reaction included 2x MyTaq Red Mix (Bioline, London, UK), the forward and reverse primers of IGFBP-3 and actin. The applied PCR conditions were as follows: the initial denaturation step at 94°C for 5 min, 20-30 cycles at 94°C for 30 sec, 55-60°C for 30 sec, 72°C for 30 sec, and the final elongation step at 72°C for 5-7 min. The PCR products are subjected to 2% agarose gel electrophoresis and visualized by Gel Doc EZ System (Bio-Rad Laboratories, Hercules, CA, USA).

For real-time PCR, the PCR reaction included the SYBER green reagents (Enzynomics, Daejon, Korea), forward and reverse primers of vimentin, actin. The real-time PCR was performed using Applied Biosystems 7300 real-time PCR system ( Applied Biosystems, Thermo Fisher Scientific, USA). The applied real-time PCR conditions were as follows: the pre-incubation step at 95°C for 15 min; 40 cycles at 95°C for 10 min; 60°C for 20 sec, 72°C for 30 sec, and the melting curve analysis to determined reaction specificity. The relative quantification of mRNA levels was performed using the comparative CT method.

## Animal experiments

All the animal procedures were performed under the control of the Seoul National University Institutional Animal Care and Use Committee's approved protocols. Mice were housed in the standard temperature and humidity-controlled facility with 12 hours of light/dark cycle.

For the spontaneous HNSCC tumorigenesis model, the 8-week-old wild-type (WT) (*Igfbp3*<sup>+/+</sup>) and *Igfbp3* KO mice (*Igfbp3*<sup>-/-</sup>) were administered with drinking water contained 100 µg/ml of 4-NQO for four months. At the endpoint, mice were euthanized. The primary tumors and lung tissues were collected, fixed with 4% formalin, embedded in paraffin, and sectioned. Metastatic tumor formation was determined by hematoxylin and eosin (H&E) staining, followed by microscopic evaluation.

For HNSCC orthotopic xenograft models, the stable knockdown UMSCC38-shEV and UMSCC38-shBP3 cells were injected into the tongue of 8 week-old non-obese diabetic/serve combined immunodeficiency (NOD/SCID) mice. After five weeks, the mice were tail vein injected with the MMPsense 680 probe. The bioluminescence imaging was determined by IVIS SpectrumCT In Vivo Imaging System (PerkinElmer, Waltham, MA, USA). The mice were then sacrificed, and the lymph node and primary tumor tissues were harvested. The local lymph node metastasis was determined by H&E staining, followed by microscopic evaluation.

For the NSCLC xenograft model, the stable knockdown H226B-shEV and H226B-shBP3 cells were subcutaneously injected into the right flank of 8 week-old NOD/SCID mice. H226B-shBP3 tumors grown slower than the H226B-shEV tumors; therefore, primary tumor weight and lung metastasis were assessed when H226B-shBP3 tumors reach the same size as H226B-shEV tumors. Mice were sacrificed, and the primary tumor and lung tissues were collected. The tissues were fixed in 4% paraffin, embedded, and sectioned at

4  $\mu\text{m}$ . The metastatic pulmonary nodules were detected by H&E staining. The tumor number and tumor volume were calculated following the formula:  $V (\text{mm}^3) = (\text{long diameter} \times \text{short diameter}^2)/2$ , and tumor burden was calculated by the mean tumor number (N) multiplied to mean tumor volume (V). The tumor number and volume were calculated in 5 section intervals throughout the tissues.

### **Immunohistochemistry staining**

The paraffin-embedded (FFPE) tumor tissues were deparaffinized at 65°C overnight. The tissues were rehydrated with xylene and sequential percentages of ethanol solution, treated with 0.3% hydrogen peroxide for 20 min, washed with TBST and incubated with 0.3% Triton X-100 for 10 min. Subsequently, tissues were autoclaved with the antigen retrieval buffer and cooled at RT. The tissues were blocked with 10% normal serum in blocking solution (1% BSA in TBST) for 1 hour at RT. The slides were drained for a few seconds; applied diluted primary antibodies (1:1000), and incubated overnight at 4°C. After rinsed with TBST, tissues were incubated with biotinylated secondary antibodies diluted in blocking solution (1:1000 dilution) for 1 hour at RT. The tissues were washed three times with TBST and treated with avidin-biotin complexes (Vectastain Elite ABC Kit, Vector Laboratories, Burlingame, CA, USA), and the signaling was visualized using a diaminobenzidine (DAB) detection reagent (Enzo Life Science). Finally, the tissues were mounted with an IHC mounting solution (Vector Laboratories, Burlingame, CA, USA), and the IHC images were obtained using a microscope (Nikon Eclipse 80i, Nikon Instrument Inc, Tokyo, Japan).

### **Statistics**

Data are presented as the mean  $\pm$  SD. All the *in vitro* were independently repeated at least twice, and the representative results are demonstrated. The representative values in each graph were multiple replicated, and statistical significance was determined by a two-tailed

student's t-test or one analysis of variance (ANOVA) using GraphPad Prism (version 8, GraphPad Software, San Diego, CA, USA). The Shapiro-Wilk-test was performed to determine whether the *in vivo* data follows a Gaussian distribution. In the analysis,  $P < 0.05$  was considered significant.

**Table 1. List of plasmids**

Insert	Vector	Length (bp)
Flag-IGFBP-3	pCMV6	891
Flag-IGFBP-3 GGG	pCMV7	891
Flag-Vimentin	pCMV Tag2B	1398
HA-FBXL14	pCMV6	4183
Flag-FBX01	pCDNA	2358
pET32 FL- IGFBP-3	pET32a	891
pET32 N- IGFBP-3	pET32a	180
pET32 M- IGFBP-3	pET32a	288
pET32 C- IGFBP-3	pET32a	327
Myc- N- IGFBP-3	pCDNA3.1 Myc	180
Myc-M- IGFBP-3	pCDNA3.1 Myc	288
Myc C- IGFBP-3	pCDNA3.1 Myc	327
GST-FL Vim	pGEX4T2	1398
GST-head Vim	pGEX4T2	222
GST-coil Vim	pGEX4T2	927
GST-tail Vim	pGEX4T2	171
GST- head-deletion Vim	pGEX4T2	1098
GST- coil-deletion Vim	pGEX4T2	393
GST- tail-deletion Vim	pGEX4T2	1098

**Table 2. List of primers for real-time PCR**

Targets	Forward	Reverse
Vimentin	CTTCGCCAACTACATCGACA	GCTTCAACGGCAAAGTTCTC
IGFBP-3	GCCAGCTCCAGGAAATGCTA	TGAATGGAGGGGGTGGAACT

## **4. RESULTS**

**IGFBP-3 inhibits the migratory and invasive potential of HNSCC and NSCLC cells by suppressing EMT phenotypes.**

Base on the evidence that IGFBP-3 suppresses cell- adhesion, angiogenic and metastatic activities in NSCLC and HNSCC [40-42, 46], I investigated the effect of IGFBP-3 on the proliferative, migratory, and invasive capacities of HNSCC and NSCLC cells. I first determined the mRNA and protein expression of IGFBP-3 in several HNSCC cell lines (**Figure 1-5A**). Among cell lines, I selected those with high (UMSCC38, UMSCC1) and low (OSC19-Luc) levels of IGFBP-3 to perform the gain and loss of IGFBP-3 experiments. I generated UMSCC38 and UMSCC1 cells in which IGFBP-3 was silenced by shRNAs (UMSCC38-shBP3 and UMSCC1-shBP3) or the OSC19-Luc cells with IGFBP-3 overexpression (OSC19-BP3) (**Figure 1-5B**). Moreover, the NSCLC cell lines with high (H226B) and low (H1299) IGFBP-3 expression [47] were included in this study, and the H226B-shBP3 and H1299-BP3 cell lines were established by stable transfection of shRNA IGFBP-3 or IGFBP-3 expression vector (**Figure 1-5B**). Subsequently, the effects of IGFBP-3 on the proliferation, migration, and invasion of HNSCC and NSCLC cells with IGFBP-3 manipulation were investigated. The manipulation of IGFBP-3 expression negligibly affected cell proliferation (**Figure 1-6A**) but induced remarkable changes in the migratory and invasive capacity of HNSCC and NSCLC cells (**Figure 1-6B-C**). The UMSCC38-shBP3, UMSCC1-shBP3, and H226B-shBP3 cells exhibited faster-wound closure than the corresponding control cells as determined by scratch assay. In contrast, force overexpression of IGFBP-3 significantly delayed wound closure in OSC19-Luc and H1299 cells (**Figure 1-6B**). The consistent results were observed in the transwell assays. Silencing of IGFBP-3 showed a significant increase in migratory and invasive capacities of UMSCC38, UMSCC1, H226B cells, whereas overexpression of IGFBP-3 remarkably suppressed the migration and invasion of OSC19 and H1299 cells (**Figure 1-6C, D**). These

results indicate that IGFBP-3 suppresses the migratory and invasive potential of HNSCC and NSCLC cells.

Given that EMT is the initial step for cancer cell migration and metastasis [10], I next investigated whether IGFBP-3 could suppress the EMT phenotypes. The common characterization of EMT is the downregulation of epithelial markers and upregulation of mesenchymal markers; thus, I examined the effect of IGFBP-3 on the E-cadherin, N-cadherin in HNSCC cells with the manipulation of IGFBP-3 expression. Silencing of IGFBP-3 induced E-cadherin's downregulation and N-cadherin's upregulation, whereas overexpression of IGFBP-3 decreased N-cadherin expression and increased E-cadherin expression, as demonstrated in western blot (**Figure 1-7A**) and immunofluorescence (**Figure 1-7B**) analysis. The role of IGFBP-3 on TGF $\beta$ -induced EMT was further investigated. Treatment with TGF $\beta$ - a well-known EMT inducer [48] significantly increased migration in UMSCC38-shBP3 cells compared to UMSCC38-shEV cells (**Figure 1-8B**). However, the TGF $\beta$ -enhanced migration effect was markedly ablated by treatment with recombinant IGFBP-3 protein (**Figure 1-8B**). TGF- $\beta$  induced morphological changes to a more mesenchymal-like state in UMSCC38-shBP3 cells but not in the corresponding control cells (**Figure 1-8A**). The inhibitory effect of IGFBP-3 on EMT *in vivo* was confirmed by immunohistochemistry (IHC) analysis of N-cadherin and fibronectin expression in xenograft tumors derived from mice inoculated with H226B-shEV and H226B-shBP3 cells. Tumor tissues from mice bearing H226B-shBP-3 cells exhibited a significantly increased N-cadherin and fibronectin expression compared to the tumor tissues from mice bearing H226B-shEV cells (**Figure 1-9**).

Accumulating evidence shows the interplay between EMT cancer stem cells (CSC) properties [49]. Cancer cells undergoing EMT exist in the CSC population leading to anticancer drug resistance, tumor recurrence, metastasis, and malignant tumors [50]. Thus,

I next investigated whether IGFBP-3 could inhibit CSC phenotypes. The HNSCC and NSCLC cells in which IGFBP-3 was silenced increased sphere-forming ability, whereas cells with IGFBP-3 overexpression significantly decreased sphere formation (**Figure 1-10A**). Treatment with recombinant IGFBP-3 protein markedly suppressed the OSC19 and H1299 sphere formation (**Figure 1-10B**). Aldehyde dehydrogenase (ALDH) has been considered the marker for CSC in various cancer types [51]; therefore, I investigated the impact of IGFBP-3 on the ALDH<sup>high</sup> population in NSCLC and HNSCC cells using the AldRed 588-A assay. As shown in **Figure 1-10C**, the depletion of IGFBP-3 expression increased the ALDH<sup>high</sup> population in UMSCC38, UMSCC1 cells. Contrastingly, ectopic expression IGFBP-3 decreased the OSC19 and H1299 ALDH<sup>high</sup> populations. Altogether, these results indicate that IGFBP-3 suppresses EMT phenotypes in HNSCC and NSCLC cells.

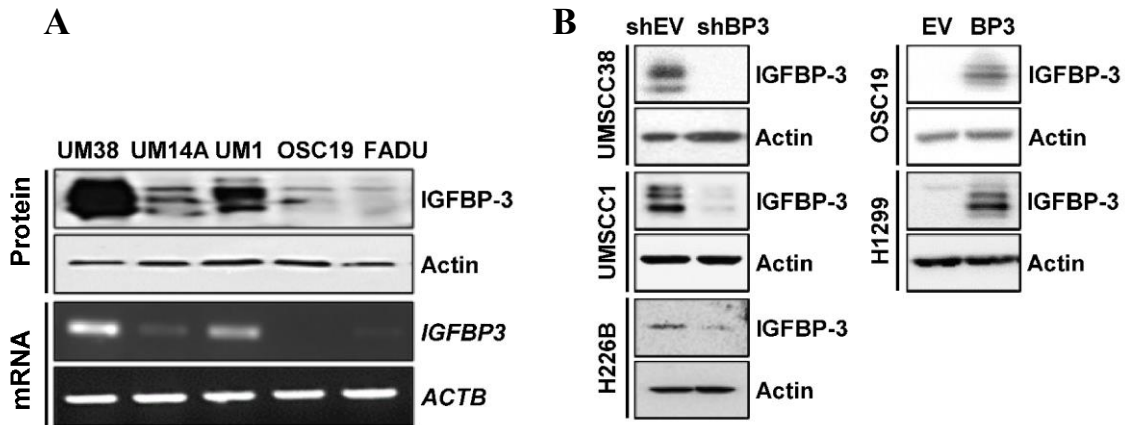


**Figure 1-5. The IGFBP-3 expression in HNSCC cell lines.**

(A) The protein and mRNA expression of IGFBP-3 in the indicated HNSCC cells were determined by western blot (upper panels) and RT-PCR (lower panels) analysis. (B) Cells with high IGFBP-3 levels (UMSCC38, UMSCC1, H226B) were stably transfected with the empty control shRNAs (shEV) and IGFBP-3 shRNA (left), whereas cells with low IGFBP-3 expression (OSC19-Luc, H1299) were forced to express IGFBP-3 (right). The protein expression of IGFBP-3 in the indicated cells were determined by western blot analysis. UM38: UMSCC38; UM1: UMSCC1; UM14A: UMSCC14A; OSC19: OSC19-Luc.

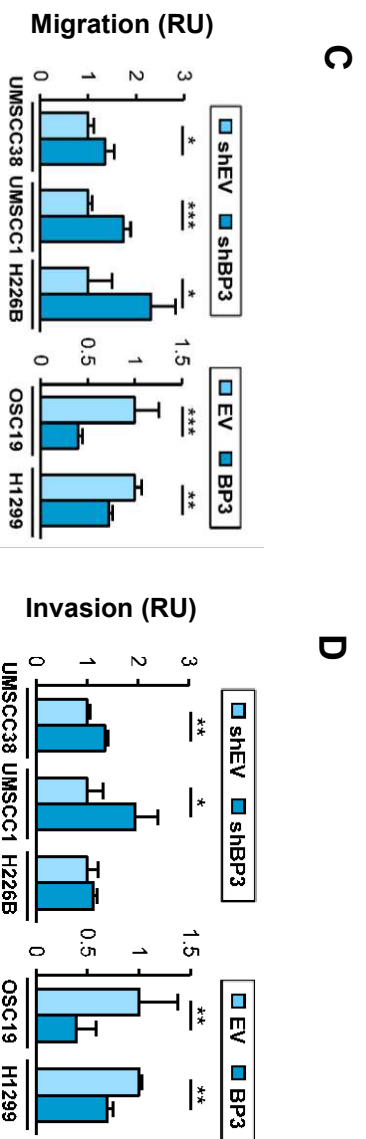
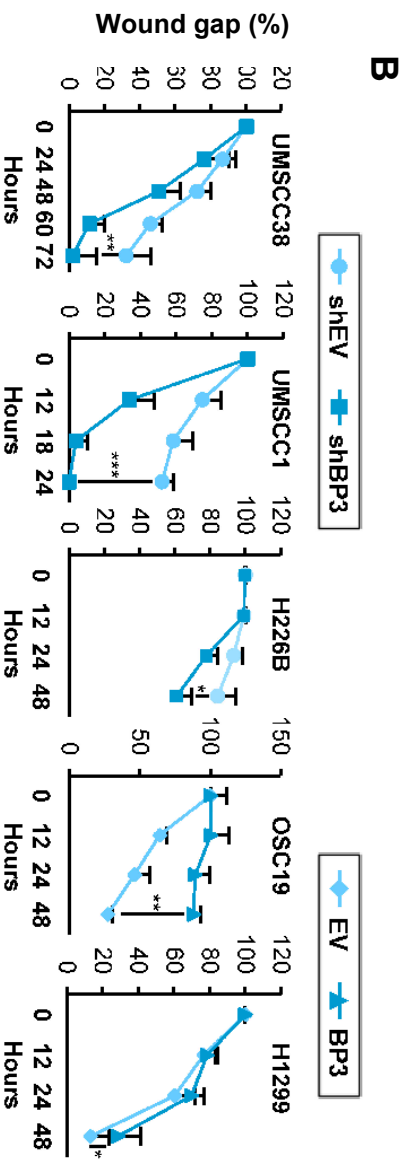
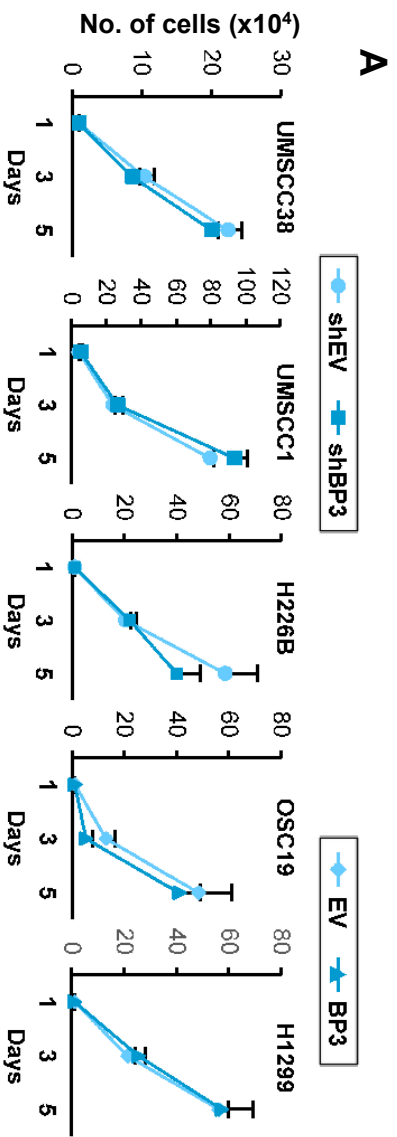


**Figure 1-6. The effect of IGFBP-3 on the proliferative, migratory and invasive potential of NSCLC and HNSCC cells.**

(A) The cell proliferation abilities of indicated cells were determined by cell counting assay. The migratory and invasive capacity of HNSCC and NSCLC cells wherein IGFBP-3 levels were manipulated are determined by scratch assay (B), migration (C), and invasion (D) assays. Data represent the mean  $\pm$  SD. \*\*P<0.01, \*\*\*P<0.001 were determined by the two-tailed Student's t-test compared with the corresponding control cells.

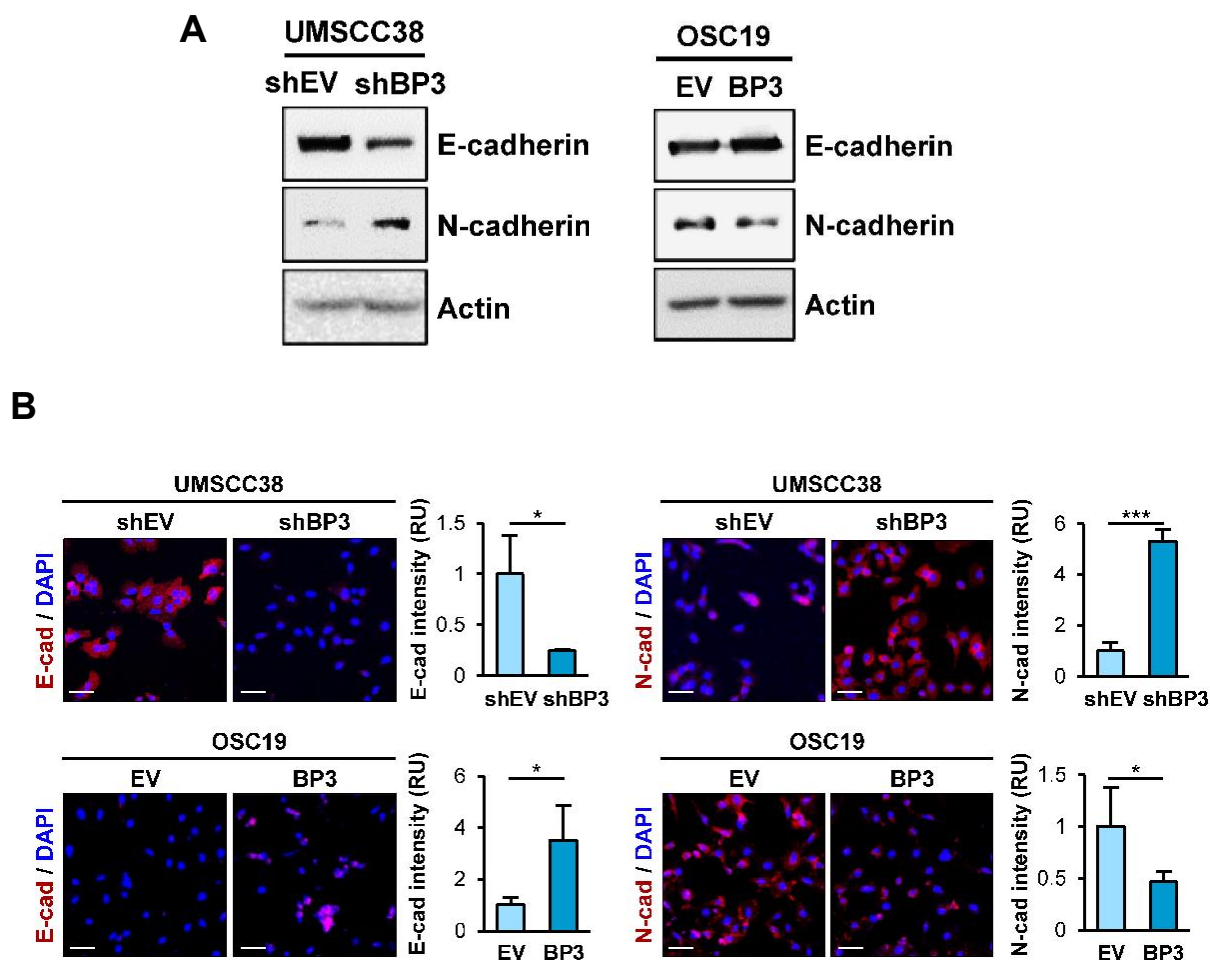


**Figure 1-7. IGFBP-3 regulates EMT markers expression in HNSCC cells.**

The protein expression of EMT markers (E-cadherin, N-cadherin) of indicated cells was determined by western blot analysis (A) and Immunofluorescence analysis (B). Scale bar: 50  $\mu$ m. The quantification of the E-cadherin intensity was analyzed using ImageJ software. The bar represents the mean of intensity relative unit (RU)  $\pm$  SD. \* $P$ <0.05, \*\*\* $P$ <0.001 were determined by the two-tailed Student's t-test compared with the corresponding control cells.

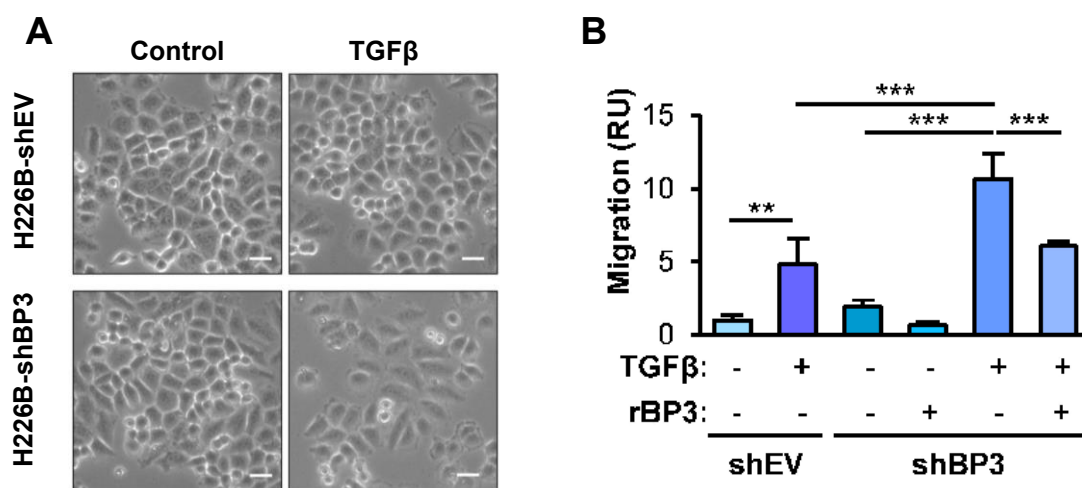


**Figure 1-8. The effect of IGFBP-3 on TGF- $\beta$ - induced migratory phenotypes in HNSCC and NSCLC cells.**

(A) H226B-shEV and H226B-shBP3 cells were treated with TGF- $\beta$  (10ng/ml) for 48 hours. The representative images of control and TGF- $\beta$  treated cells were determined by microscope. Scale bar: 40  $\mu$ m. (B) UMSCC38-shEV and UMSCC38-shBP3 cells were stimulated with or without TGF- $\beta$  (10ng/ml) in the absence or presence of recombinant IGFBP-3 (10  $\mu$ g/ml) for 48 hours and then subjected to migration assay. The bar represents the mean migration relative unit (RU)  $\pm$  SD. \*\*P<0.01, and \*\*\*P<0.001 were determined by the two-tailed Student's t-test compared with the corresponding control cells.

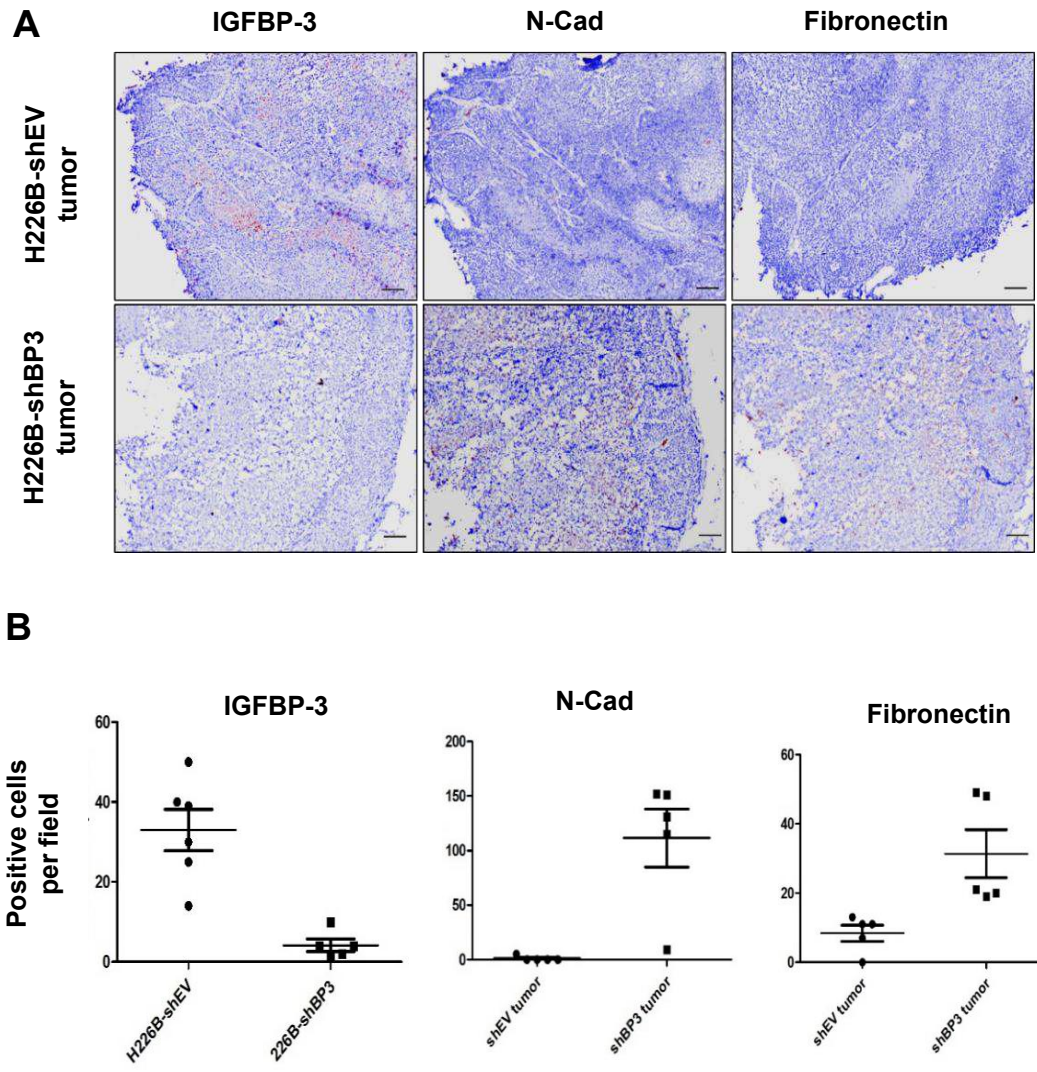


**Figure 1-9. The expression of EMT markers in H226B-shEV and H226B-shBP3 xenograft tumors**

(A) The expression of IGFBP-3, N-cadherin, and fibronectin in H226B-shEV and H226B-shBP3 xenograft tumors was determined by IHC staining, scale bar: 0.5 mm. (B) The IHC quantification was examined using ImageJ software. The bar represents the mean  $\pm$  SD.

\* $P < 0.5$ , \*\* $P < 0.01$ , and \*\*\* $P < 0.001$  were determined by the two-tailed Student's t-test.

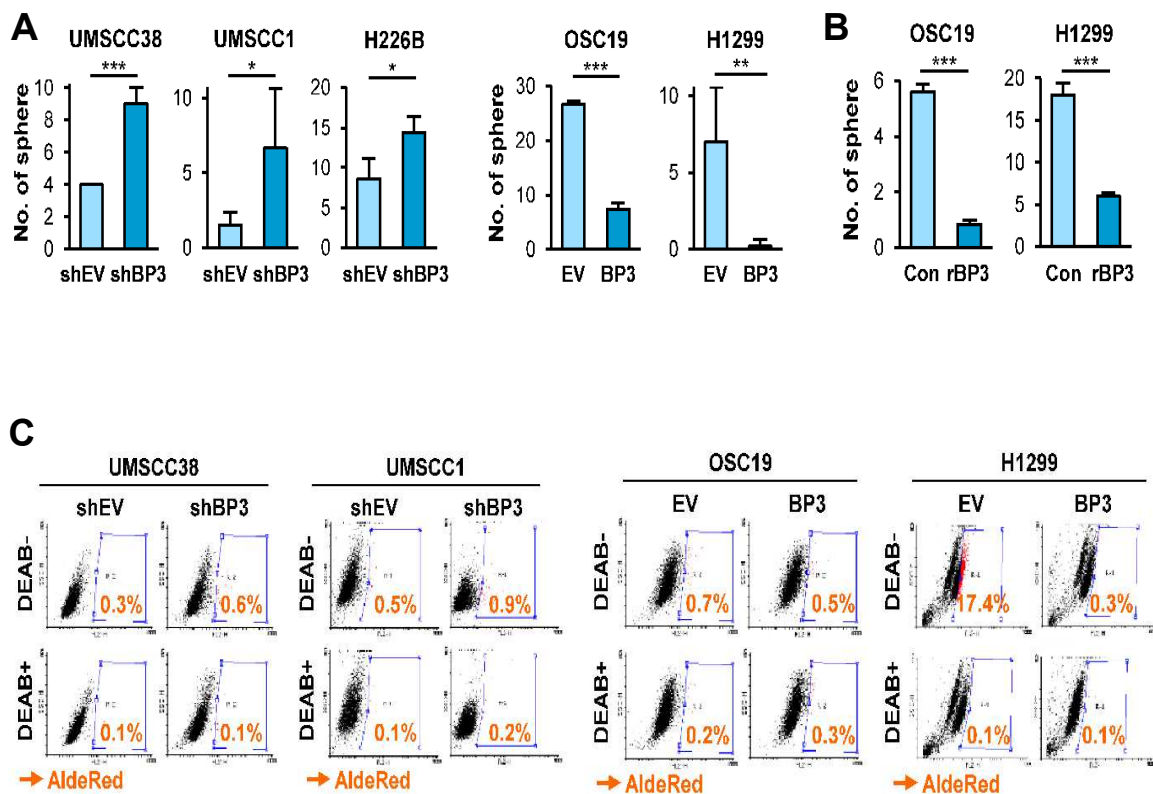


**Figure 1-10. IGFBP-3 inhibits CSC properties in HNSCC and NSCLC cells.**

The sphere-forming ability of stable knockdown IGFBP-3 cells (UMSCC38, UMSCC1) and cells with IGFBP-3 overexpression (OSC19, H1299) (A) or recombinant IGFBP-3 treatment (B) were determined by sphere formation assay. (C) The ALDH activity of the indicated cells was determined by the ALDH assay. An aliquot of each cell sample was treated with AldeRed 588-A with or without DEAB, followed by flow cytometry. The DEAB sample is the negative control used for the fluorescent baseline setting. The shift of fluorescence in the gating area representing the ALDH<sup>high</sup> population. Data represent the mean  $\pm$  SD. \* $P < 0.05$ , \*\* $P < 0.01$ , and \*\*\* $P < 0.001$  were determined by the two-tailed Student's t-test compared with the corresponding control cells.

### **IGFBP-3 suppresses HNSCC and NSCLC metastasis *in vivo*.**

We further examined the antimetastasis effect of IGFBP-3 on HNSCC and NSCLC cells using *in vivo* animal experiments. We induced the oral carcinogenesis in the systemic *Igfbp3* knockout (KO) mice on FVB/N background [52] by exposure to 4-nitroquinoline-1-oxide (4-NQO), a carcinogen agent that has been described previously to generate squamous tumor in mouse oral cavity [53-55]. After three months of 4-NQO administration, both wild-type (WT) and *Igfbp3* KO mice developed squamous tongue lesions (**Figure 1-11A, B**). The high susceptibility of FVB/N background to chemical-induced carcinogenesis [56, 57] might explain the formation of the metastatic nodule in WT mice (**Figure 1-11C**), which is inverse with the previous reports. However, 4-NQO-administered *Igfbp3* KO mice displayed significantly increased number, volume, and burden of metastatic lung tumors compared to WT mice (**Figure 1-11D**). Few carcinogen agents such as methylcarbamate and N-nitroso-tris-chloroethylureas [58] induce squamous cell carcinoma in murine lungs. Previous studies have been indicated that lung tumors induced by 4-NQO were papillary adenomas [59]. Thus, we assessed the expression of SOX2- a squamous cell carcinoma marker [60] in metastatic lung nodules by immunohistochemistry analysis (**Figure 1-11E**). The presence of SOX2 in lung nodules indicated the metastasis of HNSCC tumors.

The antimetastatic activities of IGFBP-3 were further demonstrated in the orthotopic tongue tumor model of HNSCC cells. UMSCC38-shEV and UMSCC38-shBP3 cells were injected into the tongue of non-obese diabetic severe combined immunodeficiency (NOD/SCID) mice (**Figure 1-12A**). After five weeks, all mice developed squamous tongue tumors, and the local metastatic tumor formation was assessed by IVIS imaging using the MMP 680 probe (**Figure 1-12B**), followed by the histological evaluation of cervical lymph node lesions. Histological analysis revealed that mice bearing the UMSCC38-shBP3

tumors display significantly more local lymph node metastasis than mice bearing the UMSCC38-shEV tumors (**Figure 1-12C**).

Furthermore, the effect of IGFBP-3 on the metastatic potential of NSCLC cells was further investigated in the xenograft model. The H226B-shEV and H226B-shBP3 cells were subcutaneously inoculated into the right flank of NOD/SCID mice. After 1.5 months, the primary and metastatic tumors were analyzed (**Figure 1-13A**). We observed a negligible difference in tumor weights in each group (**Figure 1-13B**). However, mice bearing H226B-shBP3 tumors displayed increased metastatic tumor number, tumor volume, and tumor burden than those bearing H226B-shEV tumors (**Figure 1-13C, D**). Accumulatively, these results indicate that IGFBP-3 suppresses the metastatic potential of HNSCC and NSCLC cells *in vivo*.

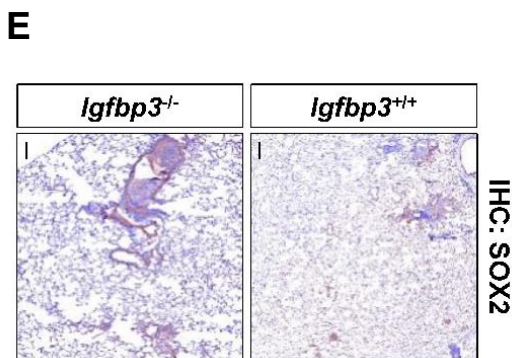
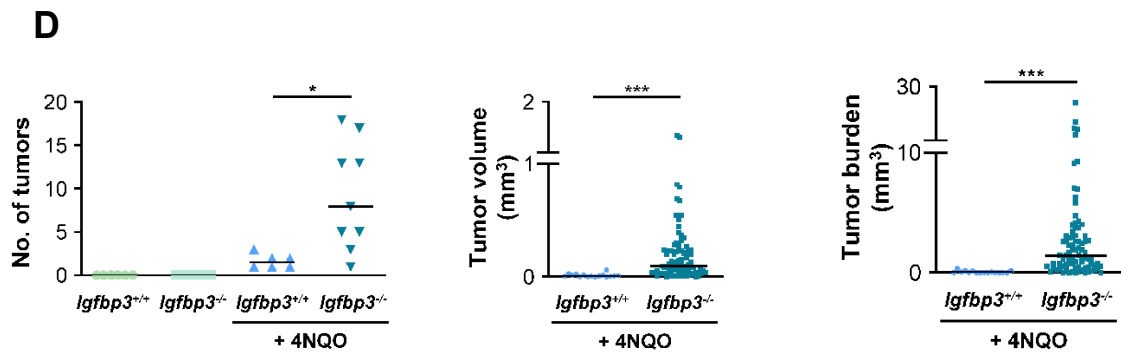
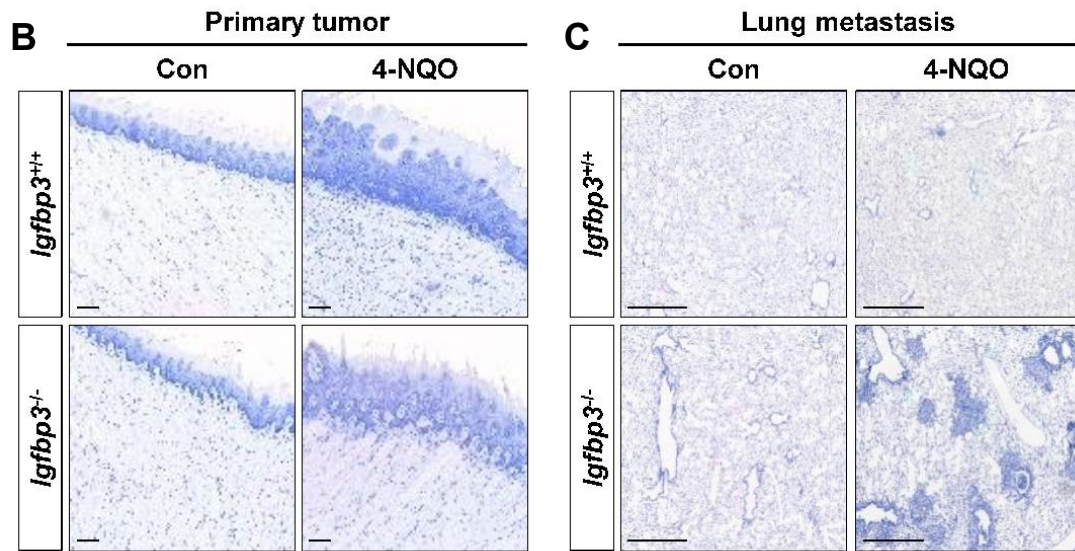
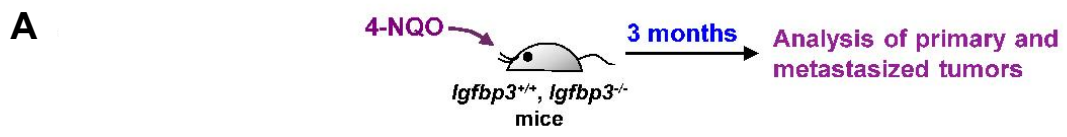


**Figure 1-11. The antimetastatic activity of IGFBP-3 in the spontaneous HNSCC tumorigenesis model.**

(A) Schematic diagram illustrating the protocol using the 4-NQO- to induce HNSCC oral tumorigenesis model in systemic *Igfbp3* KO mice: the WT and *Igfbp3* KO mice (*Igfbp3*<sup>+/+</sup> con: n=6; *Igfbp3*<sup>+/+</sup> 4-NQO: n=7; *Igfbp3*<sup>-/-</sup> con: n=6; *Igfbp3*<sup>-/-</sup> 4-NQO: n=9) were exposed to 4-NQO for three months. The primary tumors (B) and the metastatic lung tumors (C) formation were determined by H&E staining. (D) The numbers, volume, and burdens of metastatic tumors were assessed using microscopic analysis. (E) The expression of squamous cell marker SOX-2 in metastatic nodules was determined by Immunohistochemistry (IHC) analysis. Scale bar: 25  $\mu$ m. The bar represents the mean  $\pm$  SD. \*P<0.05, \*\*\*P<0.001 were determined by the Mann-Whitney test compared with the corresponding control mice.

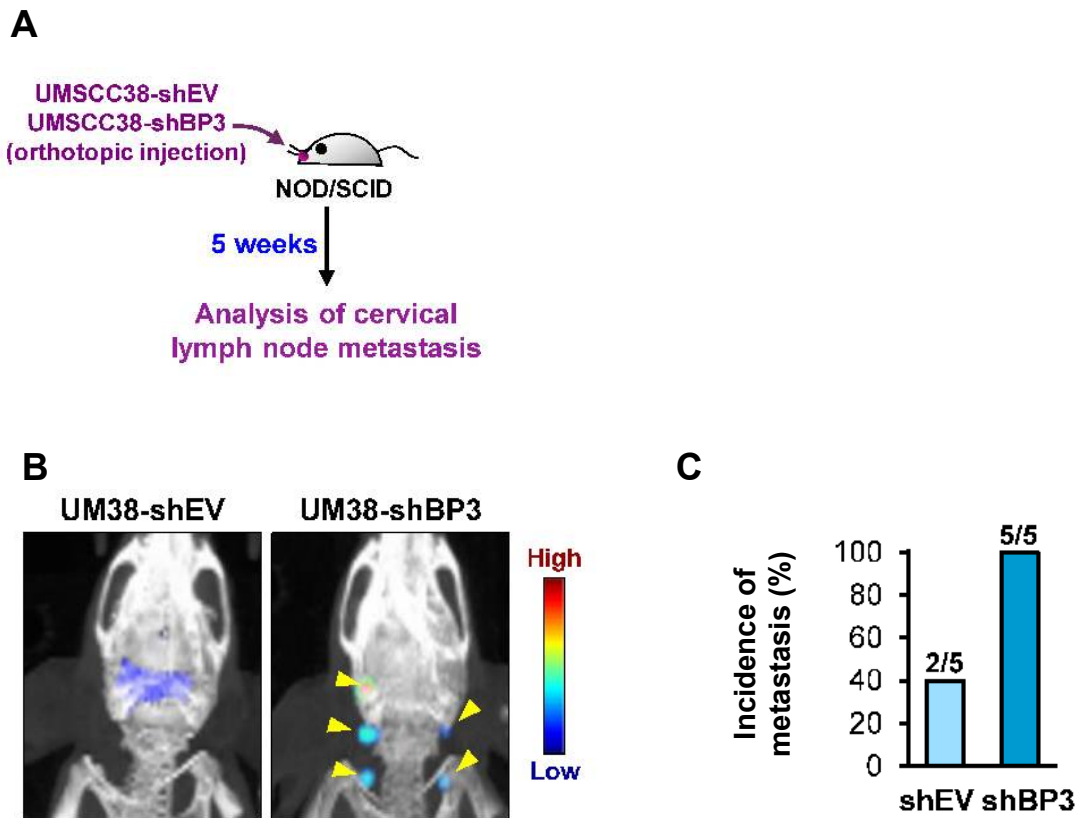


**Figure 1-12. The antimetastatic activity of IGFBP-3 in the HNSCC orthotopic mouse model.**

(A) The schematic diagram illustrating the HNSCC orthotopic mouse model: UMSCC38-shEV and UMSCC38-shBP3 cells were injected into the tongue of NOD/SCID mice (n=5). After five weeks, the primary tumor formation and local lymph node metastasis were analyzed. (B) Representative bioluminescent images demonstrated the local lymph node metastasis in mice bearing UMSCC38-shEV and UMSCC38-shBP3 tumors were determined by IVIS imaging analysis. (C) The incidence of metastatic tumors was determined by histological evaluation.



**Figure 1-13. The antimetastatic activity of IGFBP-3 in the NSCLC xenograft mouse model.**

(A) The schematic diagram illustrating the NSCLC xenograft mouse model: H226B-shEV and H226B-shBP3 cells were subcutaneously injected into NOD/SCID mice's right flank. After 1.5 months, the tumor weight (B) and metastatic lung tumor formation (C) were analyzed. No changes in the tumor weight mice in each group (B). The representative images demonstrated the metastatic lung nodules in mice bearing H226B-shEV, and H226B-shBP3 tumors were determined by H&E staining (C), scale bar: 1 mm. (D) The numbers, volume, and burden of metastatic lung tumors in each group were determined by microscopic analysis. The bar represents the mean  $\pm$  SD. \* $P < 0.05$ , \*\* $P < 0.01$ , and \*\*\* $P < 0.001$  as determined by the Mann-Whitney test (D middle and right) and the two-tailed Student's t-test (D, left) compared with the corresponding control mice.

### **IGFBP-3 downregulates vimentin protein expression in an IGF-independent manner.**

Vimentin is a cytoskeleton component that plays an essential role in cell integrity maintenance. Vimentin increases the motility, adhesion, and migration of cancer cells during the EMT. Based on the crucial impact of vimentin on EMT, migration, and metastasis [15], I assessed whether vimentin involves the antimetastatic mechanism of IGFBP-3 in aerodigestive tract cancer cells. The effect of IGFBP-3 on vimentin-induced OSC19-Luc migration was illustrated in **Figure 1-14A**. Overexpression of vimentin enhanced the migratory and invasive capacities of OSC19-Luc. However, the increased migration and invasion induced by vimentin were remarkably ablated by the dose-dependent expression of IGFBP-3. The effect of IGFBP-3 downregulated vimentin expression was determined by western blot (**Figure 1-14C**) and immunofluorescence (**Figure 1-14D**) analysis. Vimentin expression was significantly elevated in stable IGFBP-3 knockdown cells while was suppressed in cells with IGFBP-3 overexpression (**Figure 1-14C, D**). Moreover, IGFBP-3 decreased-vimentin protein expression in a dose-dependent manner (**Figure 1-14B**). Consistently, immunofluorescence analysis revealed the inverse correlation between IGFBP-3 and vimentin expression (**Figure 1-15**) in the H226B-shEV xenograft tumor.

Given that IGFBP-3 exerts cellular functions through both IGF-dependent and independent actions [39, 40], I further examined whether the IGF axis is involved in vimentin regulation by IGFBP-3. Treatment with recombinant IGFBP-3 induced vimentin downregulation in cells with shRNA-mediated IGF1-R silencing (**Figure 1-16A**). The decreased vimentin expression was also observed in UMSCC38 cells transfected with the construct encoding IGFBP-3 GGG (I56, L80G, L81G), a mutant IGFBP-3 with reduced IGF-binding affinity [61] (**Figure 1-16B**). Additionally, IGFBP-3 regulates vimentin expression in an IGF-independent manner was confirmed by immunofluorescence analysis. As shown in **Figure**

**1-16C**, both WT IGFBP-3 and IGFBP-3 GGG suppressed vimentin expression in UMSCC38-shBP3 and H1299 cells. Vimentin expression also was elevated in primary H226B-shBP3 tumors compared to H226B-shEV tumors (**Figure 1-16D**). Generally, these results indicate that IGFBP-3 downregulates vimentin in an IGF-independent manner, and vimentin is the downstream target for the antimetastatic effect of IGFBP-3.

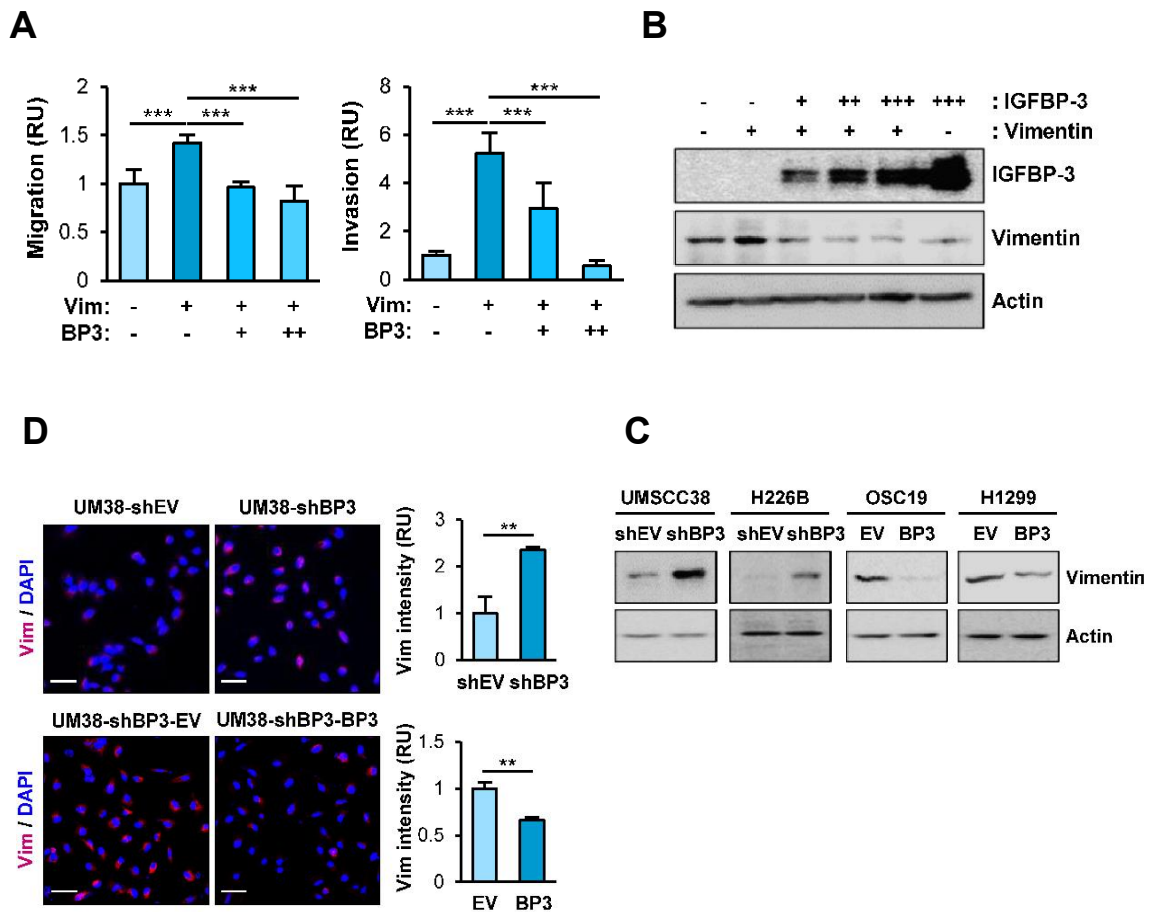


**Figure 1-14. IGFBP-3 downregulates vimentin expression.**

(A) The migratory and invasive activities of OSC19-Luc cells in which pEGFP-vimentin was transiently transfected alone or combined with the increasing amounts of IGFBP-3 plasmid were determined by migration and invasion assays. The expression of vimentin and IGFBP-3 were determined by western blot analysis (B). The vimentin expression in indicated cells was determined by western blot analysis and immunofluorescence staining (D). Scale bar: 50  $\mu$ m.

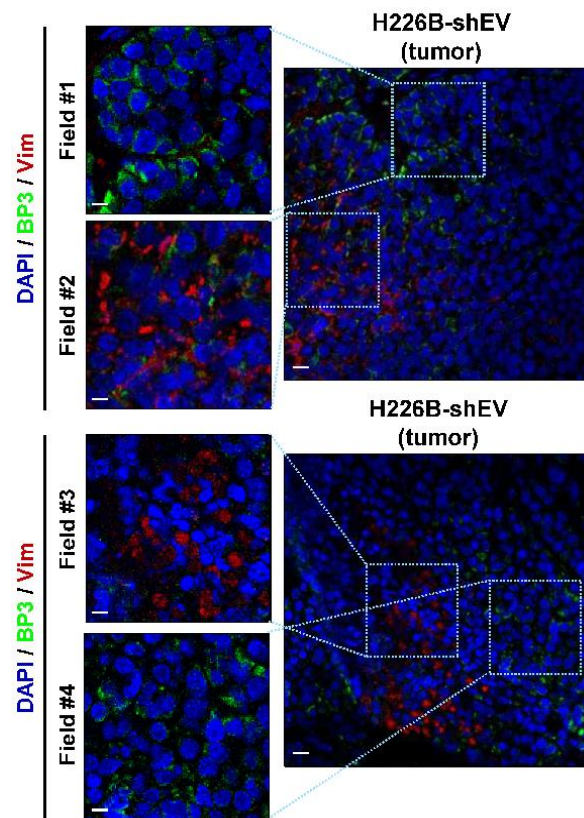


**Figure 1-15. The reverse correlation between IGFBP-3 and vimentin expression in H226B-shEV xenograft tumor.**

The reverse correlation between IGFBP-3 and vimentin in H226B-shEV xenograft tumors was determined by immunofluorescence analysis. Scale bar: 10  $\mu\text{m}$  (left), 20  $\mu\text{m}$  (right).

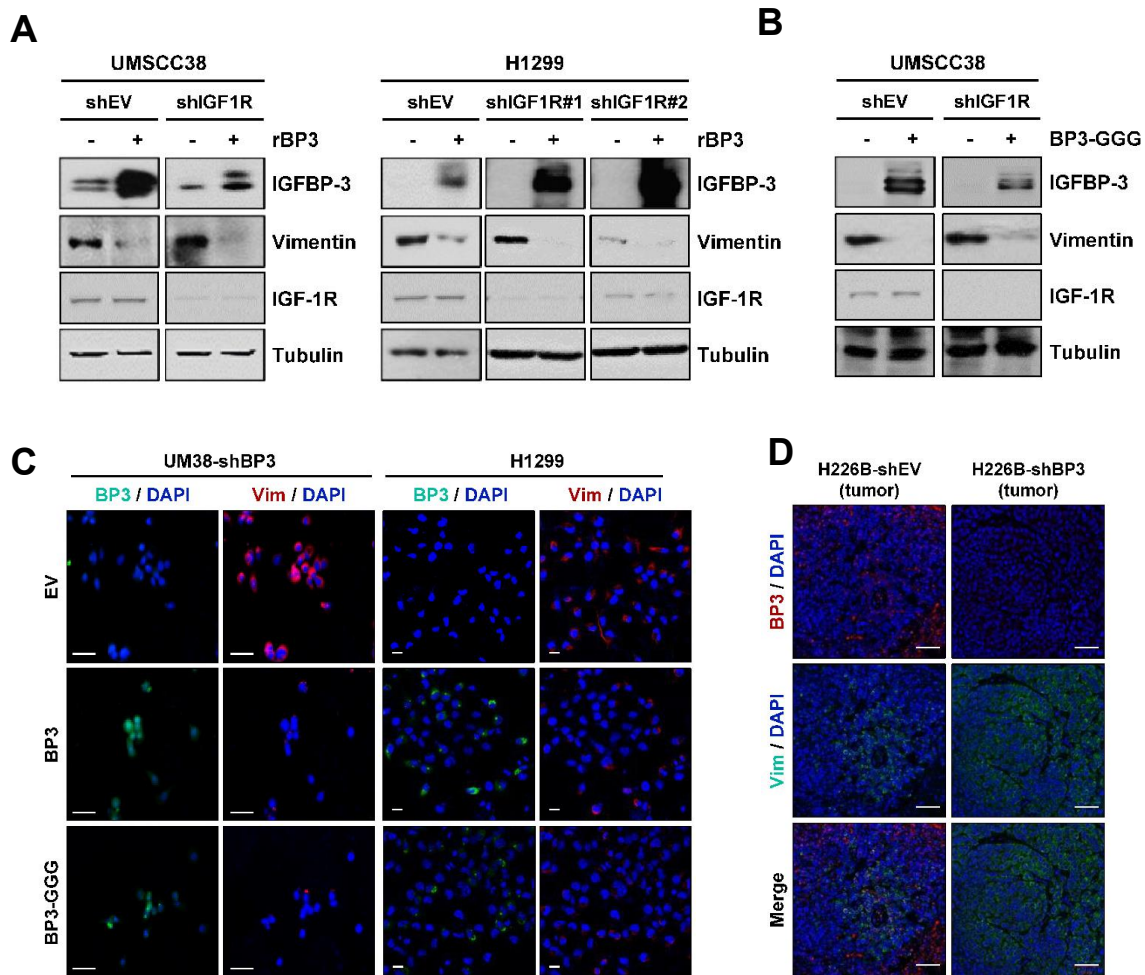


**Figure 1-16. IGFBP-3 regulates vimentin expression in an IGF-independent manner**

(A) The stable control or IGF-1R knockdown UMSCC38 (left panels) and H1299 (right panels) cells were treated with recombinant IGFBP-3 protein (10  $\mu\text{m}/\text{ml}$ ) for 48 hours. The expressions of IGFBP-3, IGF-1R, and vimentin were determined by western blot analysis. UMSCC38-shEV and UMSCC38-shIGF1R cells were transiently transfected with empty vector or pCMV6-IGFBP-3-GGG (BP3-GGG) for 48 hours. The expressions of indicated proteins were determined by western blot analysis (B) and immunofluorescence staining (C). Scale bar: 50  $\mu\text{m}$  (left) and 20  $\mu\text{m}$  (right). (D) The vimentin expression in the 226B-shEV and H226B-shBP3 xenograft tumors were determined by immunofluorescence staining using anti-vimentin, anti-IGFBP-3 antibodies, scale bar: 50  $\mu\text{m}$

### **IGFBP-3 regulates the stabilization of vimentin protein.**

Given that IGFBP-3 downregulates vimentin protein expression in HNSCC and NSCLC cells, I further investigated the effect of IGFBP-3 on the vimentin mRNA expression. As shown in **Figure 1-17A**, manipulation of IGFBP-3 expression did not alter vimentin mRNA levels in HNSCC and NSCLC cells, suggesting that IGFBP-3 regulates vimentin expression post-transcriptionally. I next examined the effect of IGFBP-3 on vimentin stability in UMSCC38-shEV and UMSCC38-shBP-3 cells in the presence of cycloheximide (CHX) [62] to block the protein synthesis. Interestingly, silencing of IGFBP-3 expression significantly enhanced the vimentin half-life, whereas overexpression of IGFBP-3 in UMSCC38-shBP3 cells remarkably diminished the vimentin stabilization (**Figure 1-17B, C**). This result indicates that IGFBP-3 regulates the protein stability of vimentin.

The ubiquitin-dependent proteasome pathway is critical for controlling cell functions by regulating various cellular proteins' stability [63]. The proteasome mediates the degradation of vimentin, which has been suggested previously [64]. Thus, I investigated whether IGFBP-3 regulates vimentin stability via the ubiquitin-dependent proteasome pathway. As shown in **Figure 1-17D**, vimentin's ubiquitylation was diminished in UMSCC38-shBP3 cells, whereas overexpression of IGFBP-3 remarkably enhanced ubiquitination of vimentin (**Figure 1-17E**). These results suggest that IGFBP-3 induces vimentin degradation through the ubiquitin-dependent proteasome pathway. To elucidate whether IGFBP-3 could interact with vimentin, I performed the immunoprecipitation assay using MG132-treated UMSCC38-shEV cells. I detected the endogenous vimentin in IGFBP-3 immunoprecipitates and endogenous IGFBP-3 in vimentin immunoprecipitates (**Figure 1-18A**). There is undetectable IGFBP-3 – vimentin association in cells with low IGFBP-3 basal level. However, ectopic expression of IGFBP-3 enhanced the interaction

between IGFBP-3 and vimentin in these cells (**Figure 1-18B**). I next generated the bacterial recombinant His-tagged IGFBP-3 and GST-tagged vimentin proteins. The IGFBP-3 and vimentin interaction was further investigated using a pull-down assay with bacterial recombinant IGFBP-3 or GST-tagged vimentin and UMSCC38 cell lysate. **Figure 1-18C** showed the apparent association between IGFBP-3 and vimentin. I further investigated whether IGFBP-3 directly binds to vimentin. By performing the *in vitro* binding assay using bacterial recombinant His-tagged IGFBP-3 and GST-tagged vimentin proteins, I detected the direct interaction between IGFBP-3 and vimentin (**Figure 1-18D**). Immunofluorescence analysis of vimentin and IGFBP-3 expression in MG132-treated UMSCC38 cells demonstrated their co-localization in the cytoplasm (**Figure 1-18E**). Altogether, these results suggest that IGFBP-3 interacts with vimentin and mediates vimentin degradation through the ubiquitin-dependent proteasome pathway.

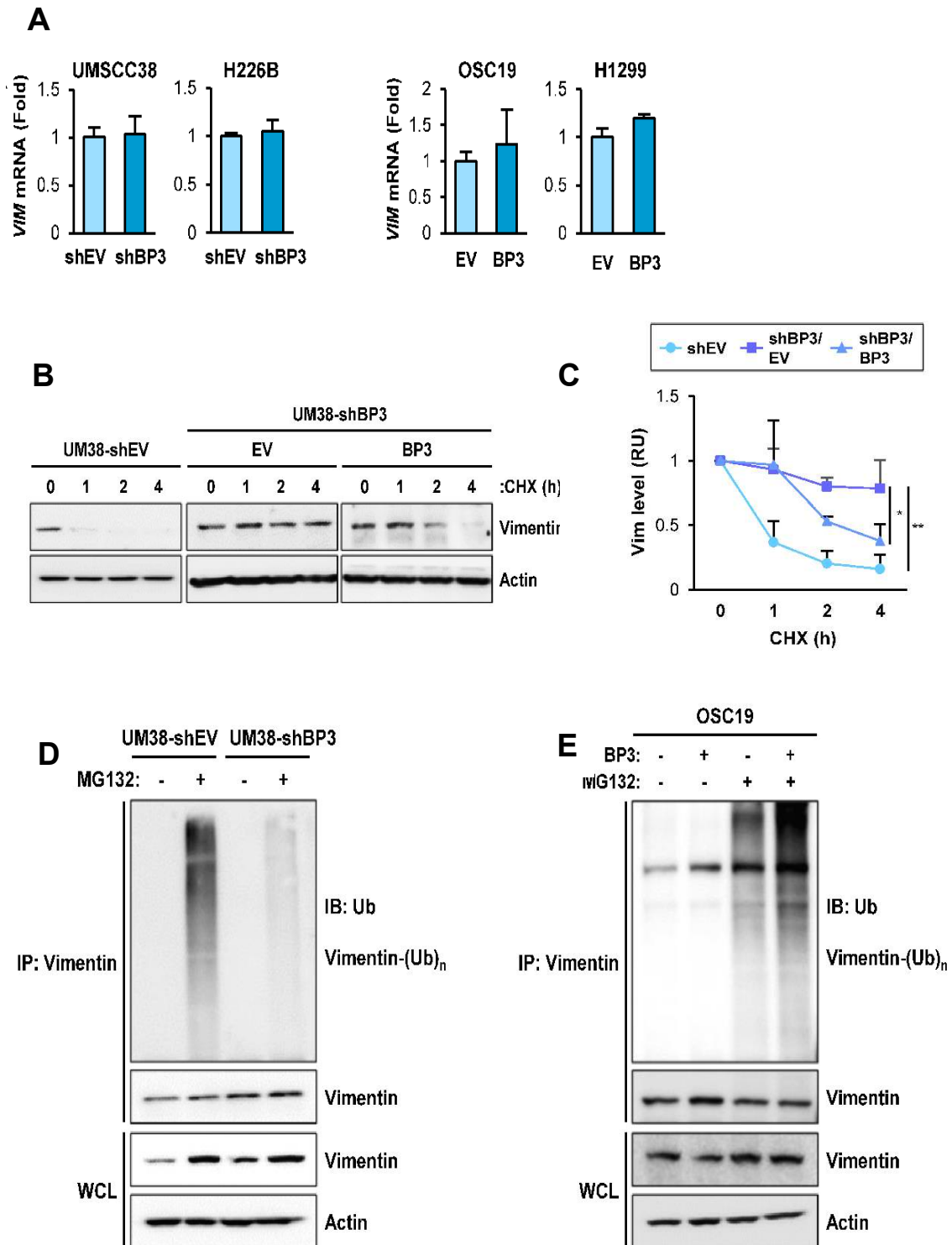


**Figure 1-17. IGFBP-3 regulates vimentin stability through the ubiquitin-dependent proteasome pathway.**

(A) The *VIM* mRNA expression in HNSCC and NSCLC cells with the manipulation of IGFBP-3 expression was determined by real-time PCR analysis. (B) UMSCC38-shEV cells (B, left) and UMSCC38-shBP3 cells are transfected with empty vector pCMV6 (EV) (B, middle) or pCMV6-IGFBP3 (BP3) vector (B, right) and treated with cycloheximide (CHX; 100  $\mu$ g/ml). The vimentin expression at indicated time points was determined by western blot analysis. (C) The relative vimentin level was determined by densitometric analysis of vimentin expression normalized with the actin level at each time point using ImageJ software. UMSCC38-shEV, UMSCC38-shBP3 cells (D), and OSC19-EV, OSC19-BP3 cells (E) were treated with MG132 (10  $\mu$ M, 6 hours), followed by immunoprecipitation with anti-vimentin antibody and western blot analysis with anti-ubiquitin antibody. The whole-cell lysate (WCL) protein expression was determined by western blot analysis. BP3: IGFBP-3; WCL: whole cell lysates, Ub: ubiquitin. Each bar represents the mean  $\pm$  SD. \* $P < 0.05$ , \*\* $P < 0.01$  were determined by the one-way ANOVA followed by Dunnett's post-hoc test.

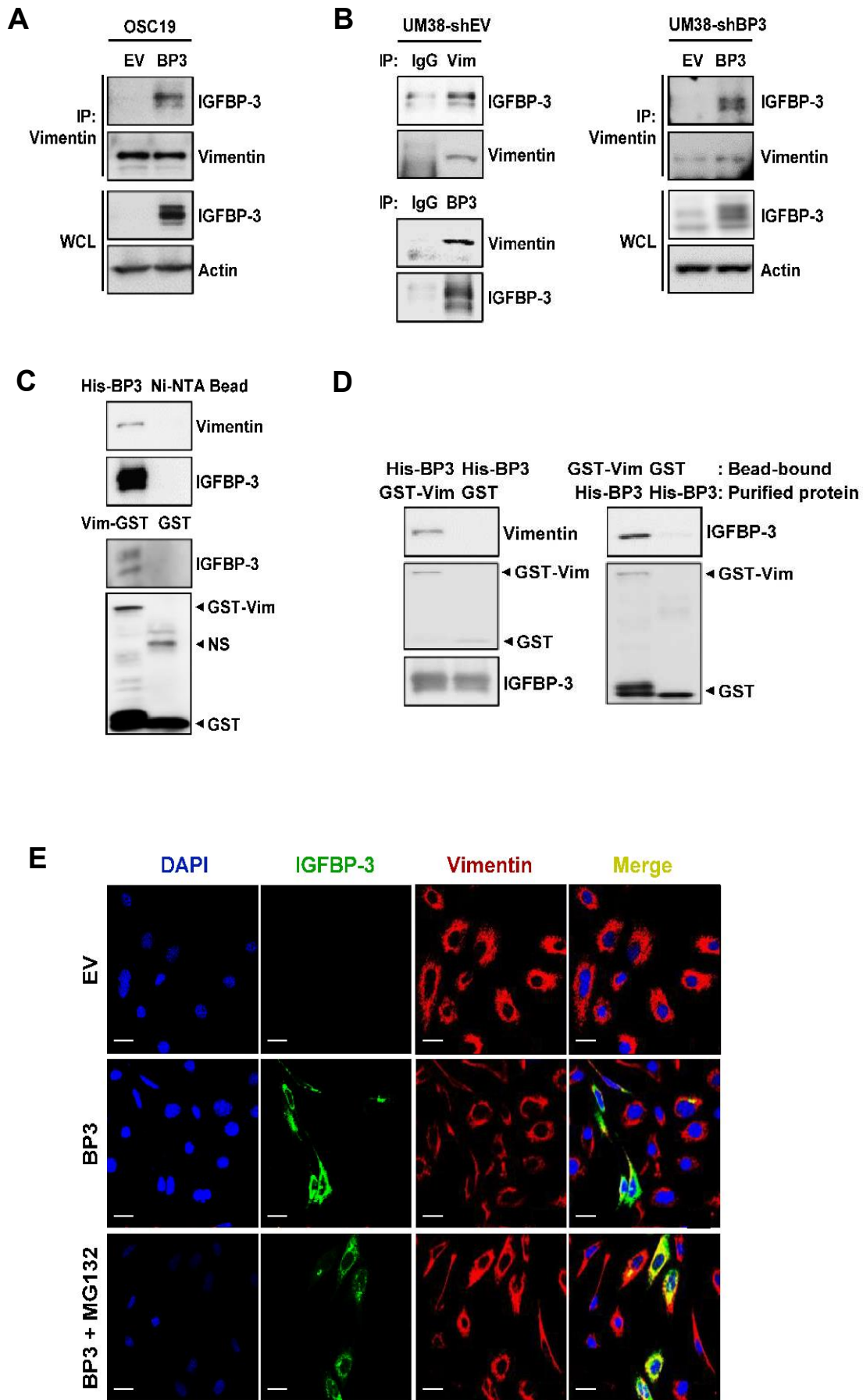


**Figure 1-18. IGFBP-3 interacts with vimentin in HNSCC cells.**

(A) The IGFBP-3 and vimentin interaction was determined by immunoprecipitation with anti-vimentin or anti-IGFBP-3 antibodies, followed by western blot analysis. (B) UMSCC38-shBP-3 and OSC19 cells were transfected with an empty vector (EV) or pCMV6-IGFBP3 (BP3). The cell lysates were subjected to immunoprecipitation with the anti-vimentin antibody, followed by western blot analysis. (C) Ni-NTA agarose bound recombinant His-tagged IGFBP-3 (upper) or glutathione (GSH) agarose bound recombinant GST-tagged vimentin proteins were incubated with UMSCC38 cell lysates. The interaction between agarose-bound proteins and endogenous proteins was determined by immunoblotting with anti-IGFBP-3 or anti-vimentin antibodies. Ni-NTA agarose and GSH agarose bound GST binding acts as the negative control binding to ensure specific interaction. (D) The direct interaction between vimentin and IGFBP-3: the bead-bound proteins and the purified recombinant proteins of IGFBP-3 and vimentin were incubated in TNE buffer. The complexes were pulled down. The direct interaction of two proteins was determined by western blot using anti-IGFBP-3, anti-vimentin, anti-GST, anti-His antibodies. (E) The co-localization of vimentin and IGFBP-3: UMSCC38-shBP3 cells were transiently transfected with empty vector pCMV6 (EV) or pCMV6-IGFBP3 (BP3) for 48 hours, followed by MG132 treatment (10  $\mu$ M, 6 hours). The co-localization of IGFBP-3 and vimentin was determined by immunofluorescence. Scale bar: 20  $\mu$ m. Vim: BP3: IGFBP-3; WCL: whole cell lysates; or UM38-shEV: UMSCC38-shEV; UM38-shBP3: UMSCC38-shBP3; OSC19: OSC19-Luc. NS: the nonspecific band.

**The C-terminal domain of IGFBP3 and the head domain of vimentin are critical for their interaction.**

To determine which domain of IGFBP-3 is crucial for its interaction with vimentin, I first generated the plasmids encoding for Myc-tagged N- (N), middle-(M), and C- terminal (C) domains of IGFBP-3 [65] (**Figure 1-19A**) and then transfected them into the HEK293T cells. The interaction of IGFBP-3 domains with vimentin was determined by immunoprecipitation assay using the anti-vimentin antibody. **Figure 1-19B** exhibits the apparent interaction between the C-terminal domain of IGFBP-3 with vimentin. I next generated the bacterial plasmids containing the N-, M-, C- terminal residues of IGFBP-3 and produced the respective recombinant proteins. The pull-down assay showed the interaction between the C-terminal domain of IGFBP-3 and endogenous vimentin protein (**Figure 1-19C**). The direct association between recombinant C-terminal residues of IGFBP-3 and recombinant GST-tagged vimentin proteins was confirmed by *in vitro* binding assay (**Figure 1-19D**).

The human full-length vimentin composes the central  $\alpha$ -helical- $\alpha$  coiled-coil domain capped on each side by the non- $\alpha$  helical amino- (head) and the carboxy- (tail) terminal domains [66, 67]. To determine the vimentin domain, which is critical for binding with IGFBP-3, I generated the recombinant GST-tagged head, coiled-coil, and tail domains of vimentin proteins (**Figure 1-20A**). The interaction of vimentin domains with IGFBP-3 was determined by *in vitro* binding assay. The head domain of vimentin directly binds to IGFBP-3, as shown in **Figure 1-20B**. I further confirmed the specific binding of IGFBP-3 and vimentin head domain using the recombinant vimentin domain-deletion mutants. Deleting the tail and coiled-coil domains of vimentin did not affect its interaction with IGFBP-3, whereas deleting the vimentin head domain significantly eliminated the IGFBP-

3 and vimentin interaction (**Figure 1-20C**). Together, these results indicate that the C-terminal domain of IGFBP-3 and the head domain of vimentin are critical for their binding.

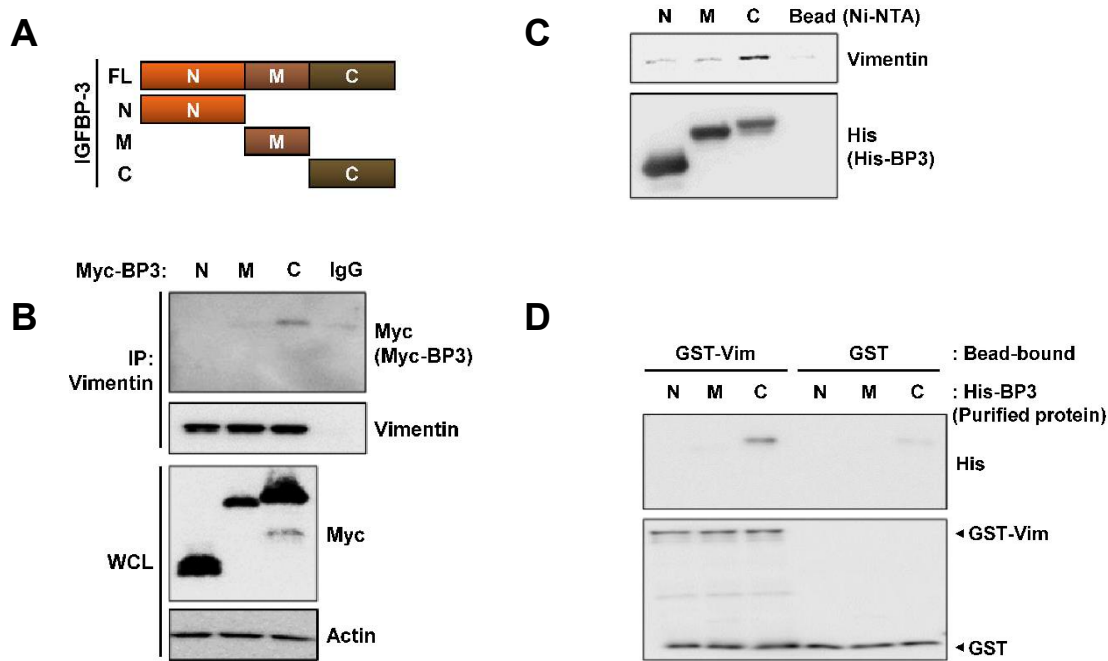


**Figure 1-19. The C-terminal domain of IGFBP-3 is critical for the interaction with vimentin.**

(A) The schematic diagram illustrates the structure of full-length and domains of IGFBP-3. (B) The binding of IGFBP-3 domains with vimentin was determined using immunoprecipitation: HEK293T cells were transfected with Myc-tagged N-, M- and C-terminal domains of IGFBP-3 plasmids for 48 hours. The cell lysates were immunoprecipitated with anti-vimentin antibody, followed by western blot analysis. (C) The interaction between N-, M- and C-terminal domains of IGFBP-3 with endogenous vimentin was determined by pull-down assay: The Ni-NTA agarose bound recombinant His-tagged N-, M-, C-terminal domains of IGFBP-3 were incubated with UMSCC38 cell lysates. (D) Direct interaction between domains of IGFBP-3 with vimentin was examined by *in-vitro* binding assay: The GSH beads-bound recombinant vimentin was incubated with the recombinant N-, M-, C-terminal domain of IGFBP-3 proteins in the TNE buffer. The protein interaction was determined by immunoblotting using anti-Histidine, anti-GST antibodies.

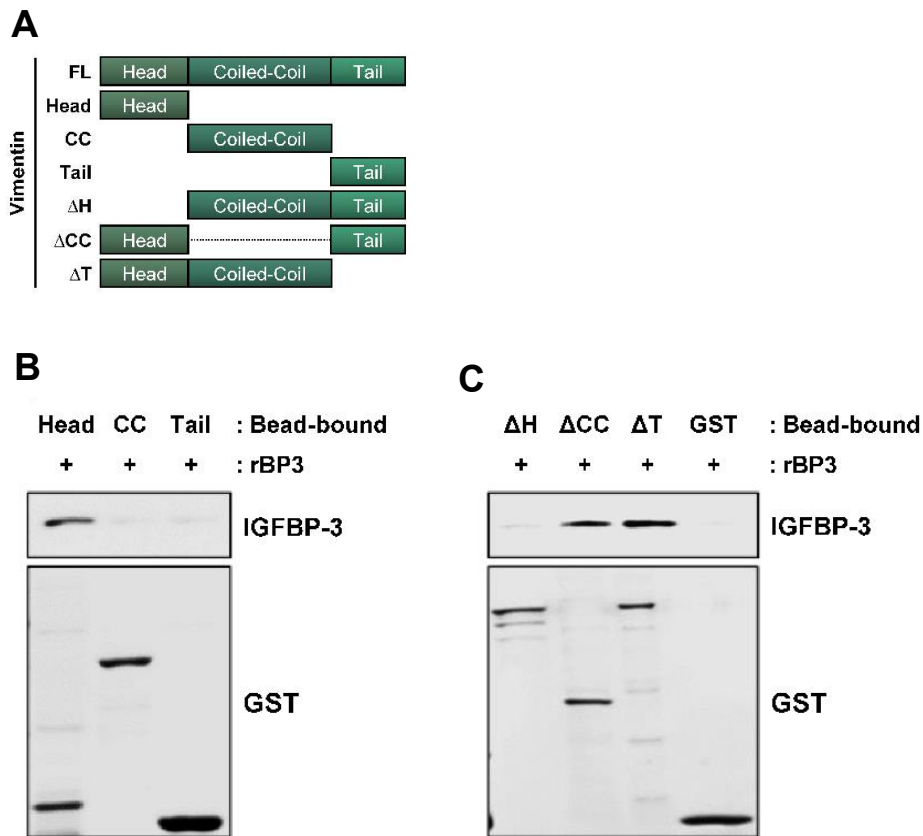


**Figure 1-20. The head domain of vimentin is critical for the binding with IGFBP-3**

(A) The schematic diagram illustrates the full-length and domain constructs of vimentin. (B) The *in-vitro* binding assay determined the binding of vimentin domains and IGFBP-3: the bead-bound recombinant vimentin's domain (head, coil-coiled, tail) proteins (B) or the bead-bound recombinant domain-deletion mutant of vimentin (C) were incubated with the recombinant IGFBP-3 protein in TNE buffer. The binding complexes were pulled down, and the protein interaction was determined by immunoblotting. The GSH-bound GST binding acts as a negative binding control sample. Head: head domain; CC: coiled-coil domain; Tail: tail domain;  $\Delta H$ : head domain deletion mutant;  $\Delta CC$ : coiled-coil domain deletion mutant;  $\Delta T$ : tail domain deletion mutant.

**IGFBP-3 induces vimentin protein destabilization through the ubiquitin-dependent-proteasome pathway by mediating the complex between vimentin and the F-box E3 ubiquitin ligase FBXL14.**

Since IGFBP-3 induces vimentin ubiquitination, I assessed the E3 ligases implicates in the polyubiquitination of vimentin. The SKP-Cullin1-F box (SCF) comprises the S phase kinase adapter protein, scaffold protein Cullin1, and F-box protein is the largest family of the ubiquitin ligase complexes [68]. In SCF complexes, the F-box protein ligases recognize various biological and oncogenic substrates for ubiquitination and protein degradation. A siRNA library was screened to determine the potential ubiquitin ligases that mediate vimentin degradation by IGFBP-3, including siRNA targeting 11 F-box E3 ligases: FBXO1, FBX04, FBX09, FBX15, FBX32, FBXL6, FBXL12, FBXL14, FBXW7, and FBXW8. Silencing of FBXO1, FBX04, FBXL14 by siRNAs remarkably suppressed vimentin expression (**Figure 1-21**), which is consistent with previous studies that reported these F-box ligases' impact on the expression of several mesenchymal markers, including vimentin [69-72]. Next, I investigated whether these candidate proteins could mediate the vimentin ubiquitination in UMSCC38 cells. As shown in **Figure 1-22A**, siRNA mediated FBXO1 or FBXL14 silencing significantly abolished the polyubiquitination of vimentin in UMSCC38 cells. To further elucidate which E3 ligases are involved in the IGFBP-3-induced vimentin degradation process, I performed immunoprecipitation of vimentin expression in the HEK293T cells cotransfected with IGFBP-3 and FBXL14, or FBXO1, followed by MG132 treatment. **Figure 1-22B** showed the interaction of IGFBP-3 and vimentin with FBXL14 but not with FBXO1. Consistently, FBXL14 interacted with IGFBP-3 and vimentin determined by immunoprecipitation using the anti-HA antibody (**Figure 1-22C**). Moreover, FBXL14 - vimentin interaction was apparent in cells with high IGFBP-3 expression (UMSCC38-shEV and OSC19-BP3 cells) but undetectable in cells

loss IGFBP-3 expression (UMSCC38-shBP3 and OSC19-EV cells) (**Figure 1-22D**). Co-expression of IGFBP-3 and FBXL14 in HEK293T cells markedly suppressed vimentin expression in HEK293T cells, whereas overexpression of IGFBP-3 or FBXL14 alone failed to do that (**Figure 1-22E**). Altogether, these findings suggest that IGFBP-3 induced proteasome-mediated vimentin degradation by recruiting the E3 ligase FBXL14.

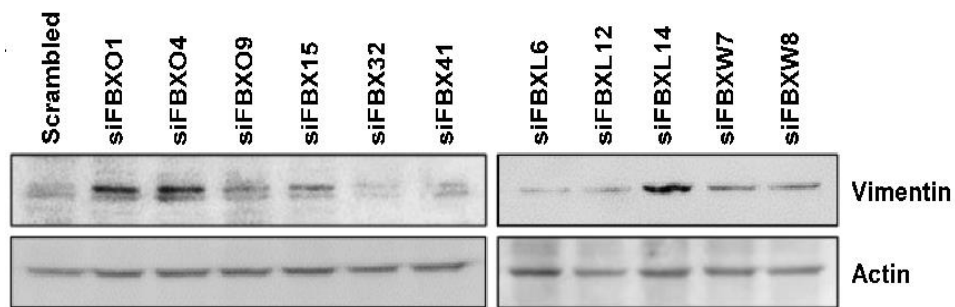


**Figure 1-21. Vimentin expression in cells with siRNAs mediated-F-Box proteins silencing.**

UMSCC38 cells were transiently transfected with control siRNA and various siRNAs targeting F-box proteins for 48 hours. The expression of vimentin was determined by western blot analysis.

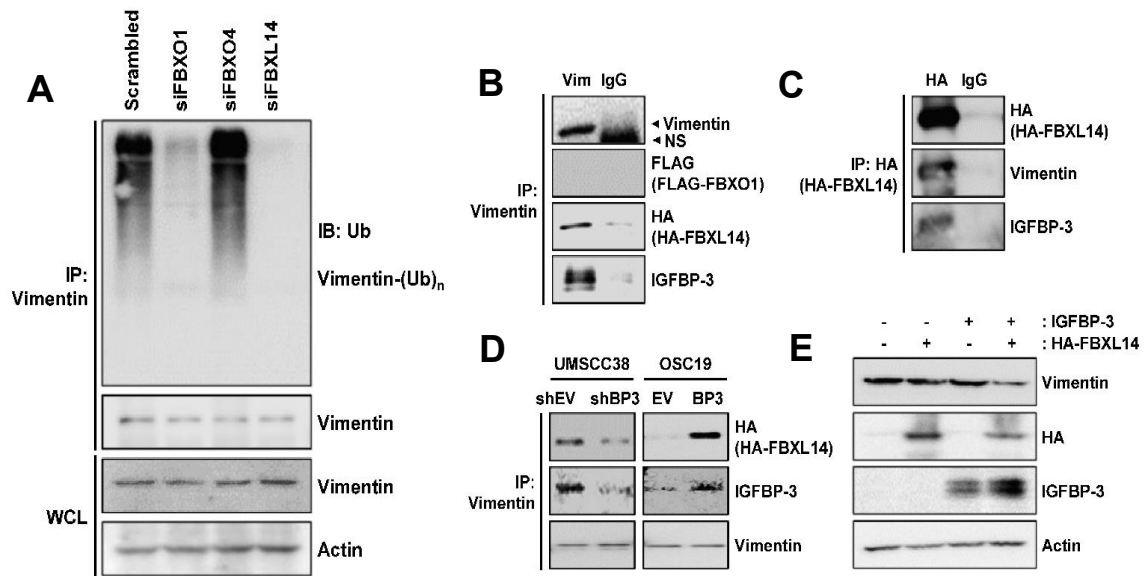


**Figure 1-22. IGFBP-3 induces ubiquitin-mediated vimentin degradation by recruitment of the E3 ligase FBXL14.**

(A) UMSCC38 cells were transiently transfected with siRNAs targeting FBXO1, FBXO4, and FBXL14 for 48 hours and then treated with MG132 (10  $\mu$ M, 6 hours). The polyubiquitylation of vimentin was determined by immunoprecipitation with the anti-vimentin antibody, followed by immunoblotting. HEK293T cells were transiently transfected with Flag-tagged FBXO1 (B) or HA-tagged FBXL14 (B, C) vectors, followed by MG132 treatment (10  $\mu$ M, 6 hours). The interaction of these E3 ligases with endogenous vimentin was determined by immunoprecipitation using the anti-vimentin antibody (B) or anti-HA (C). (D) IGFBP-3 expression enhances the interaction of vimentin and FBXL14. UMSCC38-shEV, UMSCC38-shBP3 (left) or OSC19-EV, OSC19-BP3 (right) cells were transiently transfected with HA-FBXL14 and IGFBP-3 expressing vectors and then treated with MG132 (10  $\mu$ M, 6 hours). The cell lysate was subjected to immunoprecipitation using the anti-vimentin antibody, followed by immunoblotting. (E) HEK293T cells were transiently transfected with empty vector, pCMV6-IGFBP-3, HA-FBXL14 vectors alone, or the combination of FBXL14 and IGFBP-3. The vimentin expression was determined by western blot analysis. BP3: IGFBP-3; Ub: ubiquitin; WCL: whole cell lysate.

## **5. DISCUSSION**

Metastasis, the cancer cells' movement from the primary tumors to the local or distant sites, is the leading cause of cancer-related death [73-75]. Metastasis biology is a complicated process. Until now, there is still a lack of knowledge about cancer cell migration and invasion processes, the heterogeneity of metastasis, the organotropism, and the implication of the microenvironment at the distant sites. Thus, well-understanding metastasis biology helps us prevent or develop appropriate therapeutic strategies to overcome cancer metastasis. Here, this study highlights the antimetastatic role of IGFBP-3 in aerodigestive tract cancers. IGFBP-3 suppresses EMT phenotypes, cancer migration, and metastatic potential of HNSCC and NSCLC cells. Moreover, IGFBP-3 directly associates with vimentin and mediates vimentin degradation through the ubiquitin-dependent proteasome pathway by recruiting the E3 ligase FBXL14. The C-terminal domain of IGFBP-3 and the head domain of vimentin is crucial for their binding. Altogether, these findings suggest the role of IGFBP-3 as the metastasis suppressor in aerodigestive tract cancers.

IGFBP-3 has been shown as a tumor suppressor based on its antitumor, antiangiogenic activities, and cell-adhesion suppression in various cancers [38-40]. The antimetastatic activities of IGFBP-3 have been suggested in several carcinomas [40-42]. However, the functional role of IGFBP-3 on HNSCC and NSCLC metastasis and the downstream target involved in its antimetastatic mechanism remains unknown. Therefore, I hypothesized that IGFBP-3 could exert the antimetastatic effects in HNSCC and NSCLC. In this study, serial *in vitro* and *in vivo* experiments were performed, and these results support my hypothesis: (1) Silencing IGFBP-3 expression increased the migratory and invasive capacity, whereas overexpression of IGFBP-3 suppressed these invasive phenotypes in HNSCC and NSCLC cells. (2) IGFBP-3 regulated the migratory and invasive capacity of HNSCC and NSCLC cells by suppressing the EMT phenotypes. (3) The metastatic potential of HNSCC was enhanced in 4-NQO administered *Igfbp3* KO mice. (4) The silencing of IGFBP-3 promotes

local lymph node metastasis in the HNSCC orthotopic mouse model. (5) Depletion of IGFBP-3 enhances the metastatic potential of NSCLC cells in the xenograft mouse model. Given that IGFBP-3 is a metastasis suppressor in HNSCC and NSCLC, I further determined its downstream target protein and the underlying mechanism. It has been known that IGFBP-3 could exert cellular actions in both IGF-dependent and independent manners. The IGF-independent actions of IGFBP-3 are mediated by the interaction of IGFBP-3 with non-IGFs proteins in ECM, cell surface, nucleus, or intracellular locations. IGFBP-3 suppresses tumor growth, angiogenesis, and cell adhesion in HNSCC and NSCLC by regulating Egr1 transcriptional activity and integrin signaling. EMT is the initial step for cancer metastasis. By undergoing EMT, epithelial cancer cells acquire mesenchymal phenotypes, favoring their local or distant invasion [10, 76]. However, the effect of IGFBP-3 on EMT remains unknown. This study revealed that IGFBP-3 suppressed EMT phenotypes demonstrated in the following results (1) IGFBP-3 downregulates mesenchymal markers (N-cadherin and vimentin) and upregulates epithelial marker (E-cadherin) expression in HNSCC and NSCLC cells. (2) Silencing IGFBP-3 expression promotes the TGF- $\beta$ -induced mesenchymal phenotypes in HNSCC cells. (3) Mice bearing H226B-shBP-3 tumors displayed increased mesenchymal marker expression (N-cad and Fibronectin) compared to those bearing H226B-shEV tumors. Strikingly, this study shows that IGFBP-3 suppresses vimentin expression in an IGF-independent manner. Previous studies have shown that vimentin sufficiently induces morphological changes in epithelial cancer cells to a mesenchymal-like shape [15]. Vimentin expression promotes cell adhesion, motility by affecting microtubules, restricting actin flow, regulating traction stress, supporting lateral cell-cell contacts, and upregulating contact-dependent cell stiffening [20]. Vimentin regulates signaling pathways associated with cell adhesion, EMT, and invasion by forming a complex with VAV-FAK [77], protecting Erk from inactivation

and promoting Erk-Slug mediated invasion [23], protecting Scribble from proteasomal degradation [78]. By maintaining heterotypic tumor cells during the collective invasion, vimentin is essential for lung adenocarcinoma metastasis. Vimentin was found in the tumor-associated fibroblasts at the invasive pack edges but not in the invading tumor cells [25]. Moreover, vimentin has been considered a valuable prognostic factor for tongue squamous cell carcinoma and NSCLC. High vimentin expression is correlated with tumorigenesis, advanced TNM stage, metastasis, and lower survival in TSCC and NSCLC patients [16, 18, 19]. These findings suggest that vimentin involves cancer metastasis through multiple aspects, and targeting vimentin is a promising strategy for antimetastasis. My results illustrated that IGFBP-3 downregulates vimentin expression in HNSCC and NSCLC cells. Overexpression of IGFBP-3 abolished vimentin-induced migration and invasion in HNSCC cells, indicating that IGFBP-3 suppresses migratory and invasive activities through its regulation on vimentin expression. I further elucidated the underlying mechanism of how IGFBP-3 negatively regulated vimentin and revealed that IGFBP-3 directly binds to and inhibits vimentin's protein stability through the ubiquitin-dependent proteasome pathway. Overexpression of IGFBP-3 induced vimentin polyubiquitination, while IGFBP-3 depletion suppressed the polyubiquitination of vimentin. The degradation of vimentin through the proteasomal pathway has been described previously. A small inhibitor, FiVe1, induces ubiquitylation, and degradation of vimentin, leading to vimentin disorganization and mitotic disruption in mesenchymal cancers [79]. Thus, vimentin depletion via proteasomal degradation pathway results in the disruption of its architecture and morphological changes to more epithelial-like states in cancer cells, explaining why IGFBP-3 regulates vimentin could inhibit cancer cell migration and invasion.

My study also revealed that the C-terminal domain of IGFBP-3 and the head domain of vimentin are crucial for their interaction. Previous studies showed that the IGFBP-3 C-

terminal domain has been crucial for its cellular internalization. Additionally, the C-terminal domain also contains multiple functional motifs such as the nuclear localization sequence (NLS), the binding sites for Heparin, acid-labile subunit (ALS), IGFs [27]. On the other hand, the head domain of vimentin contained several phosphorylation sites essential for its assembly [80]. Previously, Akt1 has been shown to phosphorylate the Ser39 [74] residue on the head domain of vimentin, enhancing vimentin-induced cancer cell motility and invasion. Therefore, I suggest that IGFBP-3 regulates cancer cell migration and invasion by preventing Akt-induced phosphorylation in vimentin's head domain.

This study further demonstrated that IGFBP-3 promotes the interaction between vimentin and the E3 ligase FBXL14, leading to ubiquitin-mediated vimentin degradation. In breast cancer, FBXL14 suppresses EMT markers expression, including vimentin [69]. FBXL14 mediates Twist and Snail proteasomal degradation, thereby regulates their protein stabilities [71, 72, 81]. Ppa, a homolog of FBXL14 in *X. laevis* embryos, has also mediated another EMT transcription factor's degradation- Slug [81]. The antimetastatic role of FBXL14 has been reported in previous studies [69]. Thus, targeting FBXL14 could control the EMT-induced metastasis in cancer cells. However, further experiments are required to elucidate the mechanism by which FBXL14 mediates the proteasomal degradation of vimentin. Here, IGFBP-3 appears as an enhancer for vimentin-FBXL14 interaction results in the destabilization and disassembly of vimentin.

## **6. CONCLUSION**

In conclusion, chapter 1 demonstrated the inhibitory effect of IGFBP-3 on migration and invasion of aerodigestive tract cancer cells by suppressing EMT phenotypes. IGFBP-3 suppresses vimentin-induced migration and invasion in HNSCC cells and negatively regulates vimentin protein expression in an IGF-independent manner. This study reveals the first time vimentin is the downstream target of IGFBP-3. IGFBP-3 directly binds vimentin and regulates vimentin protein stability through the ubiquitin-dependent proteasome pathway in cooperation with the E3 ligase FBXL14. These findings highlight the antimetastatic effect of IGFBP-3, and targeting vimentin by utilizing IGFBP-3 could be a promising strategy to treat EMT-induced metastasis. Further studies should be designed to evaluate the potential of IGFBP-3 and its C-terminal domain on the metastasis progression in aerodigestive tract cancers.

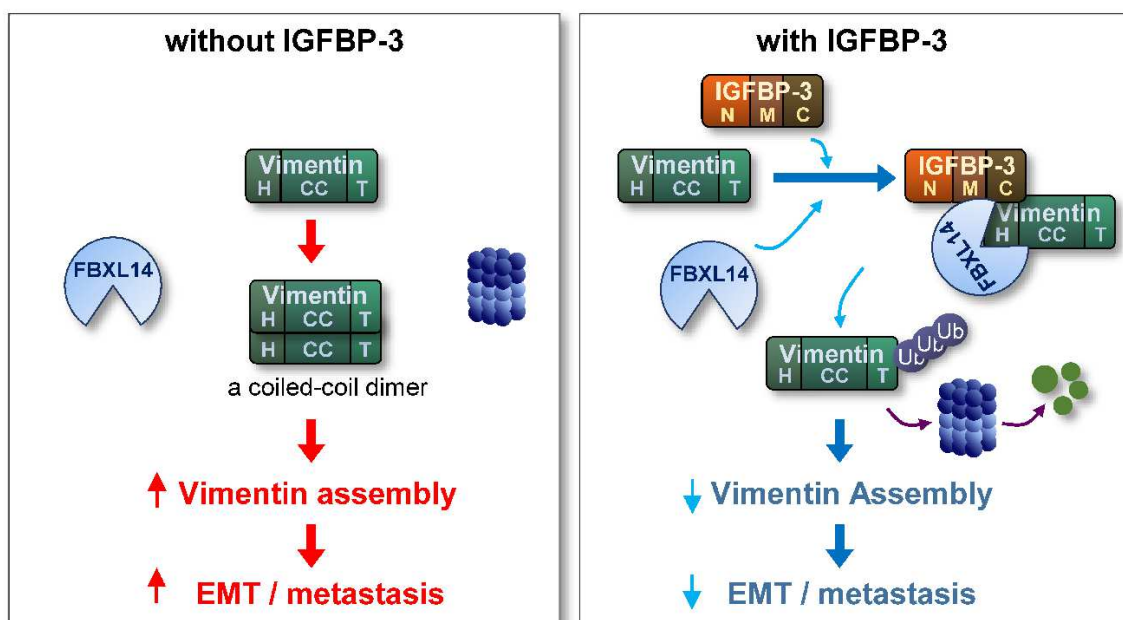


**Figure 1-23. The schematic model of the antimetastasis mechanism of IGFBP-3**

In the absence of IGFBP-3, vimentin protein composed of the central  $\alpha$ -helix coiled-coil (CC) domain capped on each side by amino (head; H) and carboxyl (tail; T) domains. Vimentin assembly mediated by coiled-coil dimerization stimulating EMT program and results in cancer metastasis (left). In the presence of IGFBP-3, IGFBP-3 mediates the ubiquitin-mediated degradation of vimentin via the recruitment of E3 ligase FBXL14, resulting in decreased vimentin assembly suppressing the EMT program and cancer metastasis (right).

## **II. CHAPTER 2**

**The development of a natural HSP90 inhibitor targeting both cancer stem and non-stem populations in non-small cell lung cancer**

## **1. INTRODUCTION**

## **Cancer stem cells (CSCs)**

The solid malignant tumors consist of cancer stem cells (CSC) and the bulk tumor (non-CSC) populations. Cancer stem cells are the subpopulation of tumor cells that can self-renew and differentiate to generate various cancer subtypes [82]. The conventional anticancer therapies only effectively eradicate the non-CSC but not CSCs populations, contributing to tumor relapse after treatment. Previous clinical studies revealed the intrinsic resistance of the CSC population to chemotherapy and radiation therapy in several malignancies [83, 84]. Moreover, drug treatment or microenvironment can induce the switch of differentiated cancer cells to CSC [85, 86], making tumor elimination more difficult. The CSC subpopulation exhibits a mesenchymal phenotype and increases migration and invasion capacities in several cancers. CSC's existence contributes to tumor development, progression, and anticancer drug resistance [87]; thus, targeting CSC is urgent.

CSCs have been supposed to originate from the normal stem cells or progenitor cells [87]. The accumulating studies revealed that CSCs are distinct from the bulk tumor cells and distinguished by specific cell surface proteins called CSC markers. Cells with stem-like properties have been shown to express CD44, CD133, epithelial cell adhesion molecule (EpCAM) on the cell surface, or exhibit the high enzymatic activity of aldehyde dehydrogenase (ALDH) in various cancers [88-91]. Moreover, inhibition of signalings essential for stemness maintenance such as Wnt, Notch, Hedgehog, Hippo has been considered anti-CSC strategy [87]. Although some progress has been made recently, the determination of specific agents targeting CSC remains challenging.

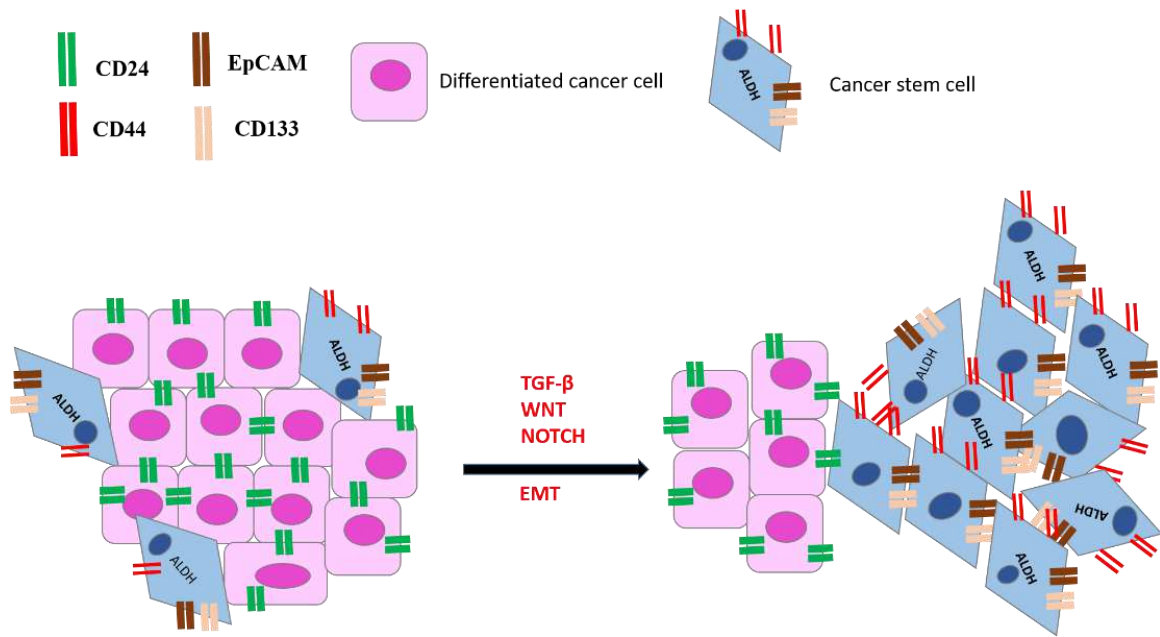


**Figure 2-1. The markers of Cancer stem cells**

CSCs are the subpopulation that possesses the self-renewal and differentiation capacity to generate the tumor's whole bulk. Tumor cells acquire stem-like properties by EMT or CSCs inducers such as TGF- $\beta$ , WNT, and Notch. CSCs can be isolated by distinct CSCs markers such as CD24, CD133, EpCAM, and aldehyde dehydrogenase (ALDH).

Reference: Singh, Anurag & Settleman, Jeff. (2010). EMT, cancer stem cells and drug resistance: An emerging axis of evil in the war on cancer. *Oncogene*. 29. 4741-51. 10.1038/onc.2010.215.

## **Heat shock protein 90 (HSP90)**

Heat shock protein 90 is a major molecular chaperone that plays an essential role in maintaining cellular homeostasis, especially under stressful conditions such as sudden increased temperature, which explains the term “heat shock.” HSP90 interacts with cellular proteins called substrates or HSP90’s clients to regulate their proper folding [92, 93]. The HSP90 monomer consists of three highly conserved domains, including the amino-terminal domain (N), the middle terminal domain (M), and the carboxy-terminal domain (C). It has been proposed that the N-terminal domain is responsible for the binding with ATP, the M-terminal domain is essential for the ATP-hydrolysis, and substrates binding; on the other hand, the C-terminal domain is responsible for the HSP90 dimerization, which is essential for HSP90 function [94].

The conformational changes of HSP90 dimer can be regulated by HSP90 co-chaperones, which control the ATP-hydrolysis, maintain the stable conformation, or recruit the client proteins to the HSPs machinery. In the unbound ATP-state, HSP90 is in the open conformation (V-shape) that allow for the recruitment and interaction with HSP90 substrates. However, upon ATP binding, HSP90 adopts the ATP-bound state. Next, the “lid region” on the N-terminal domain closes over the ATP-bound state, and the clients' protein was kept inside the chaperon complex. The N-terminal domains start to dimerize and form the closed state, crucial for the ATP hydrolysis process. After ATP-hydrolysis, two N-terminal domains disassociate to release ADP and the active form of client protein. Eventually, HSP90 returns to the open state.

The diverse HSP90 clients are protein kinases, transcription factors, steroid hormones, and E3 ubiquitin ligases. Thus by regulating these substrates' maturation, HSP90 involves many cellular pathways [94]. Overexpression of HSP90 has been reported in human cancers. High HSP90 expression frequently correlates with poor prognosis [95]. Recent

studies demonstrated the agents disrupt HSP90 function by targeting the ATP-binding pockets on the N- or C-terminal domain of HSP90. Currently, the effects of several promising inhibitors are evaluated in clinical trials [96, 97]. Thus, targeting HSP90 can be considered an effective strategy for anticancer therapy.

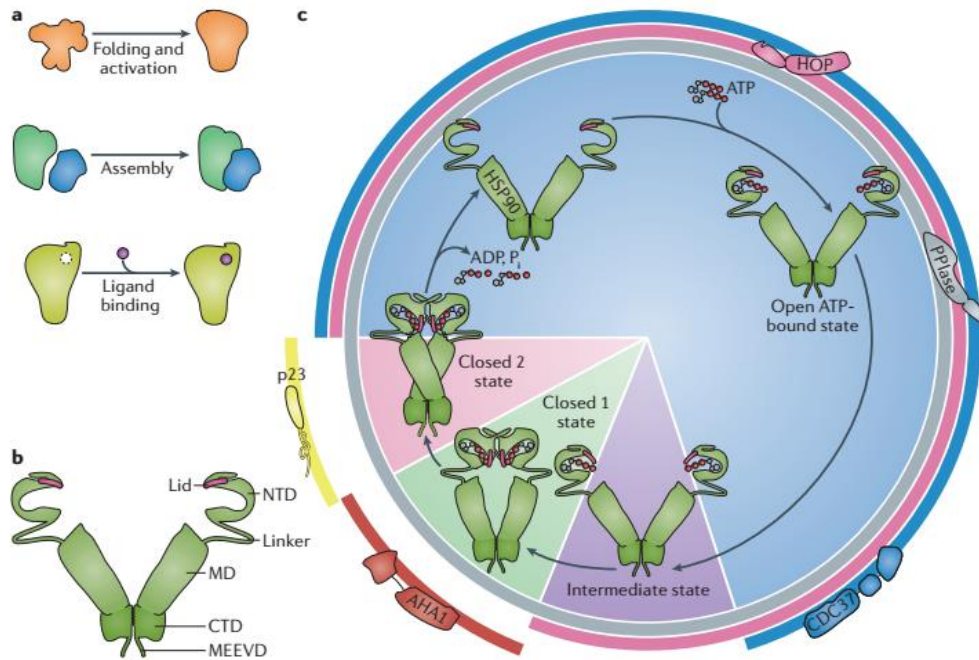


**Figure 2-2. The structure and conformational changes of HSP90**

The HSP90 mediates protein's proper folding and activation, assembly of protein complexes, or ligands' binding to its receptors. HSP90 structure composes of the N-terminal domain (NTD) containing the lid region, the middle domain (MD), and the C-terminal domain (CTD) containing a flexible MEEVD motif. The conformational changes of HSP90: when binding to ATP, HSP90 changes from the open ATP-bound to the intermediate state after the lid's closure. The interaction and twist of the two NTDs result in the conformational changes to the closed state 1 and 2 of HSP90. During the HSP90 cycles, various HSP90 co-chaperones associated with specific HSP90 states, including HOP, CDC37, AHA1, p23, and HSP70. After the ATP hydrolysis, the NCTs disassociate and release the ADP and inorganic phosphate Pi, and eventually, the HSP90 returns to the open conformation.

Reference: Schopf, F., Biebl, M. & Buchner, J. The HSP90 chaperone machinery. *Nat Rev Mol Cell Biol* 18, 345–360 (2017). <https://doi.org/10.1038/nrm.2017.20>

## **Panax ginseng**

*Panax ginseng* (*P.ginseng*) is a well-known traditional herb used worldwide and especially in Korea. Ginseng is commonly used as a dietary supplement to enhance life quality, especially in cancer patients who received conventional treatments [98]. Ginseng has been considered an adjuvant for cancer treatment when combined with other chemotherapy agents [99, 100] to reduce cancer-related symptoms or improve clinical outcomes. The ginseng compounds exert antitumor activities through cell cycle arrest, apoptosis induction, and angiogenesis suppression [98, 101, 102]. Additionally, *Panax ginseng* has been reported to exert another biological effect on cardiovascular, endocrines, and immune systems. The antioxidation and anti-inflammation effects of ginseng have been reported in previous studies [102-105].

Ginseng contains various active compounds, including saponin, polysaccharides, vitamins, flavonoids, fatty acids, etc. [100]. Many studies support the pharmacological effects of *P.ginseng* are attributed to the key ingredients- ginsenosides [101-105]. Even the research on non-saponin fractions of *P.ginseng* is low; few studies suppose the anticancer effects of these components [100, 106]. Based on the effectiveness and safety profile of *P.ginseng* on cancer treatment, identifying a new potent anticancer compound from *P.ginseng* might be a promising strategy for anticancer therapy.

## **2. PURPOSE OF THE STUDY**

The heat shock protein 90 (HSP90), a well-known chaperone, physiologically regulates the cellular proteostasis in normal and stress conditions. By controlling the proper folding of diverse proteins, HSP90 involves in many signaling pathways. Previous studies demonstrated that HSP90 facilitates many oncogenic substrates' activation leading to the HSP90 addiction of cancer cells. Moreover, HSP90 has been shown to contribute to cancer stem cells' development and maintenance (CSC) [107]. The increased HSP90 related-genes in cells with stem-like properties [107] led us to hypothesize that targeting HSP90 might be a promising strategy for anti-CSC therapy. *Panax ginseng* (*P. ginseng*), well-known Korean herbal medicine, has been used worldwide for thousands of years due to its multi-biological effects. Previous studies have revealed the anticancer activity of *P. ginseng*, and the combination of ginseng extract with other anticancer drugs improves the efficacy and reduces the cytotoxicity of these chemotherapy agents. Therefore, our study's goal in chapter 2 is to identify a natural HSP90 inhibitor isolated from *P. ginseng* that effectively targets both NSCLC non-CSC and CSC with minimal toxicity.

### **3. MATERIALS AND METHODS**

## **Reagents**

All cell culture reagents were purchased from Welgene (Daegu, Republic of Korea). The pIGF1R (Y1135/6), IGF1R, pEGFR (Y1063), EGFR, pAkt (S473), Akt, Sox2, pMEK1/2 (S217/221), MEK1/2, pmTOR (S2448), mTOR, GAPDH, pSrc (Y416), Src, caspase3, PARP, and cleaved caspase3 antibodies were purchased from Cell Signaling Technology (Danvers, MA, USA). The cleaved poly (ADP-ribose) polymerase (PARP), HIF1 $\alpha$  antibodies, and Matrigel were purchased from BD Biosciences (San Jose, CA, USA). Primary antibodies against IGF-1R, VEGF, bFGF, and actin and the horseradish peroxidase (HRP)-conjugated secondary antibodies were purchased from Santa Cruz Biotechnology (Santa Cruz, CA, USA). Anti-HSP90 antibody was purchased from Enzo Life Science (Farmingdale, NY, USA). Anti-PDGF antibody was purchased from Merck Millipore (Billerica, MA, USA). Antibodies against Oct4 and Nanog were purchased from Abcam (Cambridge, UK). The Ni-NTA agarose was purchased from Invitrogen (Carlsbad, CA, USA). ATP-agarose was purchased from Innova Biosciences (Cambridge, UK). The first-strand cDNA synthesis kit was purchased from Takara Bio Inc. (Shiga, Japan). The 3-(4,5-dimethylthiazol-2-yl)-2,5-diphenyl tetrazolium bromide (MTT), propidium iodide (PI), and other chemicals were purchased from Sigma-Aldrich (St. Louis, MO, USA).

## **Cell culture.**

The human NSCLC cell line H226B was kindly provided by Dr. John V. Heymach (MD Anderson Cancer Center, Houston, TX, USA). The human NSCLC cell line H1299, A549, H460, H292, BEAS-2B cells were purchased from the American Type Culture Collection (ATCC, USA). The human umbilical endothelial cells (HUVECs) were purchased from Invitrogen (Carlsbad, CA, USA). H460/R and H226B/R cells were previously generated in our laboratory by continuously exposing cells to the increasing paclitaxel doses for six months. Dr. Jeong Hun Kim (College of Medicine, Seoul National University, Seoul,

Korea) kindly provided the human retinal pigment epithelial cells (RPE). HT-22 cells were kindly provided by Dr. Dong Kyu Jo (College of Pharmacy, Sungkyunkwan University, Suwon, Korea). The NSCLC cells were maintained in RPMI-1640 medium with 10% fetal bovine serum (FBS) and 1% antibiotic (WelGENE, Kyeongsan-si, Korea). The BEAS-2B, HBE cells were cultured in Keratinocytes-SFM (KSFM) (Thermo Fisher, MA, USA) medium supplemented with epithelial growth factor (EGF) and bovine pituitary extract. HT-22 and RPE cells were maintained in DMEM completed medium (WelGENE, Korea). The HUVECs cells were maintained in the vasculife basal medium supplemented with vasculife VEGF life factors (Lifeline cell technology, Frederick, MD, USA). All cells were maintained in the humidified incubator with 5% CO<sub>2</sub> at 37°C.

#### **MTT assay**

Cells (1-2 x 10<sup>3</sup> cells/well) were seeded into 96-well multiwell plates for 24 hours. Cells were treated with vehicle or various saponin, non-saponin fractions, and panaxynol concentrations in the completed medium. After 48 hours, cells were treated with the 10µl/well MTT solution (4mg/ml stock) and incubated for 2-4 h at 37°C. The formazan products were dissolved in 100 µl DMSO, and the 570 nm absorbance was measured. Data are presented as the percentage absorbance values compared to the control group.

#### **Sphere formation assay**

Cells (1000 cells/ well) were seeded on ultra-low attachment 96-well plates (Corning, Corning, NY, USA), were cultured in the spheroid medium ( DMEM-F12 media supplemented with B27 (Thermo Fisher Scientific, Waltham, MA, USA), EGF, bFGF, and 1% antibiotics) containing vehicle or drugs. In sphere-forming experiments using vehicle or panaxynol- pretreated monolayer, cells were grown in sphere-forming conditions for two weeks or until spheres formed and reached sizes above.

### **Aldehyde dehydrogenase (ALDH) assay**

The high ALDH enzymatic activity was determined using the AldeRed ALADH assay kit (Merck Millipore, Billerica, MA, USA). Each group contains a test sample (AldeRed A588 alone) and a control sample (AldeRed A588 plus DEAB). H1299 cells ( $1 \times 10^6$  cells) were suspended in AldeRed buffer and then incubated with AldeRed A588 at 37°C for 40 min. Cells were resuspended in fresh AldeRed buffer and subjected to flow cytometric analysis (BD, Bioscience). The fluorescence baseline and ALDH<sup>high</sup> population were assessed using Flowing Software (Turku Bioscience Center).

### **Anchorage-dependent colony-formation assay**

Cells (300 cells/well) were seeded into 6-well plates and cultured in a medium containing vehicle or various concentrations of panaxynol for two weeks. The drug-containing medium was changed every three days. After two weeks of incubation, the plates were washed with PBS. Colonies were fixed with 100% methanol in RT for 10 min, stained with 0.002% crystal violet solution for 15 min, and washed several times with distilled water. The colony number was counted using ImageJ software (National Institutes of Health, Bethesda, MA, USA).

### **Soft agar colony formation assay**

Cells (1000 cells/well) were suspended with 1% agar solution to get the final concentration of 0.4% and seeded onto 1% bottom agar in the 24-well plates. The agar was solidified at RT and covered with 500µl complete medium with or without panaxynol. Cells were maintained at 37°C with 5% CO<sub>2</sub>, and the drug-containing medium was changed every three days. After two weeks, colonies were stained with MTT solution. Colony number was counted using ImageJ software (National Institutes of Health, Bethesda, MA, USA).

### **Cell cycle analysis**

Cells were treated with vehicle or panaxynol for 48 hours. Cells were washed with PBS two times. The adherent and floating cells were harvested. After being fixed with 100% methanol, cells were stained with a 50 µg/ml Propidium iodide (PI) solution containing RNase A (50 µg/ml) for 30 min at RT. Cells were washed, resuspended in PBS, and subjected to flow cytometry using a FACSCalibur<sup>®</sup> flow cytometer (BD Biosciences). The cell cycle analysis was performed using CellQuest software (BD Biosciences).

### **Tube formation assay**

H1299 cells were treated with panaxynol for one day and further incubated under normoxic or hypoxic conditions for four hours. After incubation, the drug-containing medium was removed, and cells were incubated with a fresh serum-free medium. After 24 hours, the conditioned medium (CM) was collected. The HUVECs cells were seeded onto CellBIND surface 96-well plates (Corning) and treated with vehicle or panaxynol CM for the tube formation assay. The HUVEC tube formation was imaged and scored by ImageJ software (National Institutes of Health, Bethesda, MA, USA).

### **Western blot analysis**

Cells were treated with vehicle or panaxynol for 48 hours. Cells were lysed in RIPA buffer contains 50 mM Tris-HCl (pH 7.4), 150 mM NaCl, 1 mM EDTA, 0.25% sodium deoxycholate, 1% Triton X-100, protease and phosphatase inhibitor cocktail (Roche Applied Science, Indianapolis, IN, USA). The protein concentration was quantified by the BCA assay kit (Thermo Fisher Scientific). Proteins were subjected to SDS-PAGE and transferred onto polyvinylidene difluoride (PVDF) membranes (Bio-Rad Laboratories, Hercules, CA, USA). After blocking with blocking buffer (3% BSA in TBST) for 1 hour at RT, membranes were incubated with diluted primary antibodies (1:1000) overnight at 4°C. Membranes were washed with TBST and incubated with secondary antibodies (1:

5,000 dilution) for 1 hour at RT. Membranes were washed several times with TBST, and the protein expression was visualized by SuperSignal West Femto chemiluminescent substrate (Thermo Fisher Scientific) using the ImageQuantLAS 4000 imaging system (GE Healthcare).

### **RT-PCR**

Total RNA was extracted using the easy-BLUE total RNA extraction kit (Intron Biotechnology, Sungnam-si, Kyunggi-do, Republic of Korea) according to the manufacturer's instruction. RT-PCR conditions are applied as follows: the initial denaturation step at 94°C for 5 min, 20-30 cycles at 94°C for 30 sec, 55-60°C for 30 sec, 72°C for 30 sec, the final elongation step at 72°C for 5-7 min. The PCR products were subjected to agarose gel electrophoresis and visualized using a Gel Doc EZ

### **Reporter gene assay**

The reporter gene assay was performed to determine the effect of panaxynol on the HRE activity. H1299 and H460 cells were transiently cotransfected with the pSV40promoter-EpoHRE-Luc reporter, pCMV- $\beta$ -gal with JetPrime transfection reagent (Polyplus-Transfection SA, Illkirch, France). The cells were maintained in hypoxic conditions. The luciferase assay was performed using the Beetle-Juice luciferase assay kit (Takara), following the manufacture's instructions. The  $\beta$ -galactosidase activity was used to normalize transfection efficiency.

### **Transfection**

H1299 cells were transfected with an empty vector (EV) or HSP90 expressing vector using the JetPrime transfection reagent (Polyplus-Transfection SA). The lentiviral particles of shEV or shHSP90 were generated, followed by the previously described methods. H1299 cells were seeded on the 6-well plate and transduced with lentiviral particles containing

control (shEV; pLKO.1) or HSP90 shRNAs (Sigma-Aldrich) in medium plus polybrene (8 µg/ml). The cells were then selected with 1-2 µg/ml puromycin for 2-3 weeks.

### **Immunoprecipitation and pull-down assay**

For immunoprecipitation assay, cells were washed with cold PBS and lysed in EBC lysis buffer containing 50mM Tris-HCl (pH 8.0), 120 nM NaCl, 0.5% NP-40, 1 mM EDTA, and protease inhibitor cocktail (Roche, Mannheim, Germany). The cell lysates were collected by centrifuging, and the protein concentration was determined using the BCA assay kit (Thermo Fisher Scientific). 1mg of cell lysates were incubated with 1µg of primary antibodies in 1.5ml microtubes. The total volume of IP reaction is 1ml. The IP reaction was rotated overnight at 4°C. Subsequently, 20 µl Protein A agarose (Merck KGaA, Darmstadt, Germany) was added to the reaction following by 2 hours rotation. The immunoprecipitants were washed three times with EBC buffer, boiled in 5X sample buffer, and subject to SDS-PAGE and immunoblotting analysis.

### **Animal experiments**

All the animal procedures were performed under the control of the Seoul National University Institutional Animal Care and Use Committee's approved protocols. Mice were housed in the standard temperature and humidity-controlled facility with 12 hours of light/dark cycle.

For the NSCLC xenograft model, H1299 cells were subcutaneously inoculated into the right flank of 6-week-old NOD/SCID mice. When tumor volume reached 150 mm<sup>3</sup>, the mice were randomly divided into the vehicle (DMSO) or panaxynol groups. Mice were orally treated with corn oil containing vehicle or panaxynol (50 or 100 mg/kg) six times per week for three weeks. Tumor volume was determined by measuring the tumor's short and long diameter using a caliper. The mouse body weight was measured twice per week

to monitor toxicity. The tumor volume was calculated using the following formula: tumor volume ( $\text{mm}^3$ ) = (small diameter)<sup>2</sup> × (large diameter) × 0.5.

For the *in vivo* serial dilution assay using ALDH<sup>high</sup> cells, first, ALDH<sup>high</sup> cell populations of vehicle- or panaxynol (1  $\mu\text{M}$ )-treated H1299 cells were obtained using AldeRed A588-kit and FACS Aria II flow cytometer (BD Biosciences). A serial number of ALDH<sup>high</sup> cells was inoculated into the right flanks of NOD/SCID mice, and the tumor incidences were observed at the endpoint of experiments.

In experiments using *Kras*<sup>G12D/+</sup> transgenic mice, three-month-old *Kras*<sup>G12D/+</sup> mice were randomly grouped and orally treated with vehicle or panaxynol (50 mg/kg) for 8 weeks. Mice were tail-vein injected with MMPsense 680 probe (PerkinElmer; 2 nmol/150  $\mu\text{l}$  in PBS, and bioluminescence images were obtained using the IVIS-Spectrum microCT and Living Image (ver. 4.2) software (PerkinElmer, Alameda, CA, USA) using an). The mice were euthanized. Lung tissues were harvested, paraffin-embedded, and sectioned. The tumor formation was evaluated by H&E staining. The tumor number (N) and volume (V) were measured in a blinded fashion by microscopic evaluation of H&E staining images. The tumor volume was calculated as described above. The number and size of tumors were calculated in five sections uniformly distributed throughout each lung tissue.

#### ***In vivo* serial dilution tumor-propagating assay**

At the end of the treatment, the single cells derived from xenograft tumors of vehicle- or panaxynol-treated mice were obtained using the tumor dissociation kit (Miltenyi Biotech). The trypan blue exclusion assay was performed to determine cell viability. Next,  $5 \times 10^2 - 5 \times 10^4$  viable cells were subcutaneously inoculated into NOD/SCID mice's right flank. The incidence of tumor formation was determined.

### **Immunofluorescence staining**

The expression of CD34, HIF1 $\alpha$ , cleaved caspase3 and Oct4 in tumor tissues was evaluated using immunofluorescence staining. The paraffin-embedded (FFPE) tumor sections were deparaffinized in the incubator at 65°C overnight. The tissues were rehydrated with xylene and sequential percentages of ethanol solution. The tissues were washed with TBST and incubated with 0.3% Triton X-100 for 10 min. Subsequently, tissues were autoclaved with the antigen retrieval buffer and cooled at RT. The tissues were blocked with a blocking solution (1% BSA in TBST) containing 10% normal serum at RT for 1 hour. The slides were drained for a few seconds; applied diluted primary antibodies (1:1000), and incubated overnight at 4°C. After rinsed with TBST, tissues were incubated with secondary antibodies diluted in blocking solution (1:1000 dilution) for 1 hour at RT. The tissues were washed three times with TBST and incubated with fluorochrome-conjugated secondary antibodies (Alexa Fluor 488, Alexa Fluor 546, Alexa Fluor 594) (1:1000 dilution) for 1 hour in RT. Cells were washed, stained with 4',6-diamino-2-phenylidole (DAPI) solution, and mounted onto the glass slides using the fluorescence mounting solution. The fluorescence images were visualized using the fluorescent microscope (Zeiss Axio Observer Z1, Carl Zeiss AG).

### **Statistics**

Data are presented as the mean  $\pm$  SD. All the *in vitro* were independently repeated at least twice, and the representative results are demonstrated. The representative values in each graph were multiple replicated, and statistical significance was determined by a two-tailed student's t-test or one analysis of variance (ANOVA) using GraphPad Prism.

**Table 3. List of primers for RT-PCR**

Targets	Forward	Reverse
<i>VEGF</i>	TCTCCCAGATCGGTGACAGT	GGCAGAGCTGAGTGTTAGC
<i>ACTB</i>	ACTACCTCATGAAGATC	GATCCACATCTGCTGGAA

## **4. RESULTS**

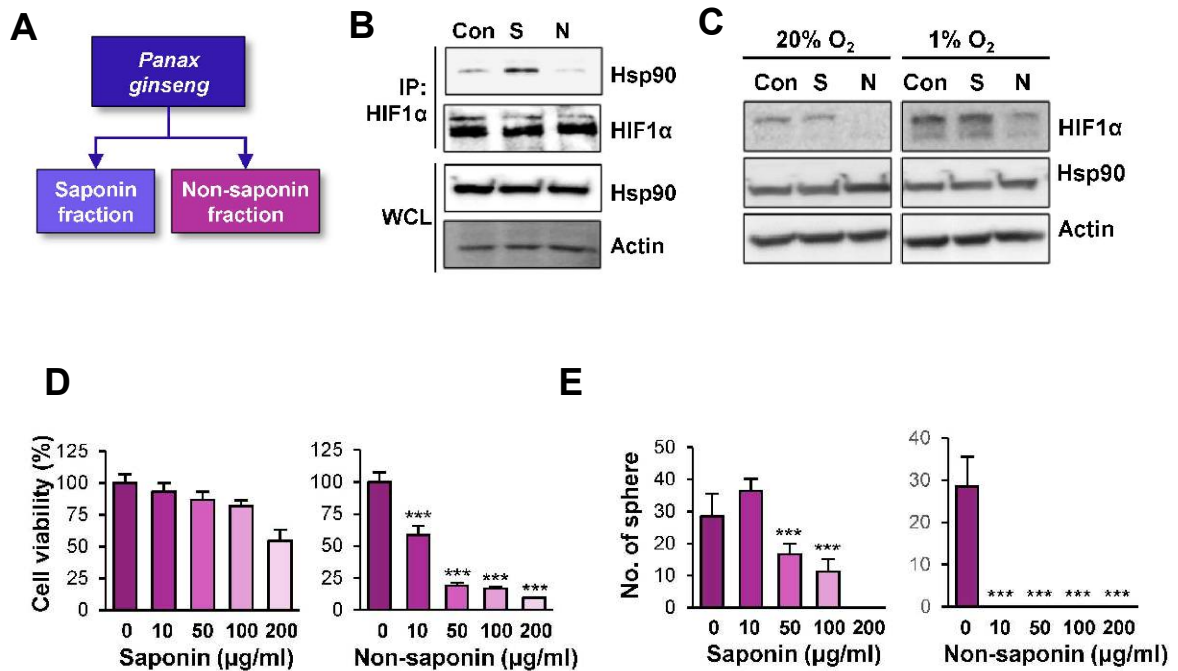
**Panaxynol is the active compound isolated from the non-saponin fraction of *P. ginseng* that suppresses the viability and sphere-forming ability of NSCLC cells.**

Given that overexpression of HSP90 and its cochaperones in several cancer cells has been described previously [108] and the HSP90 plays a crucial role in the survival and maintenance of CSCs [107]; thus, this study attempted to identify the potential anticancer drugs that could effectively disrupt HSP90 functions with limited toxicities. Previous studies have reported several natural compounds that exhibit antitumor activity with minimal toxicities [109]. Among them, I focused on *Panax ginseng*, based on its multi-biological effects, including anticancer activities with minimal toxicities [110]. I first examined the effects of saponin and non-saponin fractions extracted from *P.ginseng* (**Figure 2-3A, B**) on the HSP90 function. Given that HSP90 interacts and control the proper folding of various cellular oncogenic proteins, including the transcription factor hypoxia-inducible factor-1alpha (HIF1 $\alpha$ ). Hence, I investigated whether fractions isolated from *P.ginseng* could affect HSP90 and HIF1 $\alpha$  interaction. Strikingly, treatment with the non-saponin fraction but not saponin fraction remarkably disrupted the interaction between HIF1 $\alpha$  and HSP90 (**Figure 2-3B**) and inhibited HIF1 $\alpha$  protein expression in both normoxia (20% O<sub>2</sub>) and hypoxia condition (1% O<sub>2</sub>) (**Figure 2-3C**) in H1299 cells. I further investigated the effects of saponin and non-saponin fraction on the cell viability and sphere-forming ability of H1299 cells by MTT and sphere-forming assay. **Figures 2-3D, E** showed that the non-saponin fraction displayed significantly decreased H1299 cell viability and sphere-forming ability compared to the saponin fraction. These results suggest that the non-saponin fraction of *P. ginseng* exhibits inhibitory effects on both NSCLC non-CSC and CSCs populations.

I further investigated the non-saponin fraction's effect on lung tumor formation using the Kras<sup>G12D/+</sup>-driven-spontaneous lung tumor mouse model [111]. Kras<sup>G12D/+</sup> mice were orally

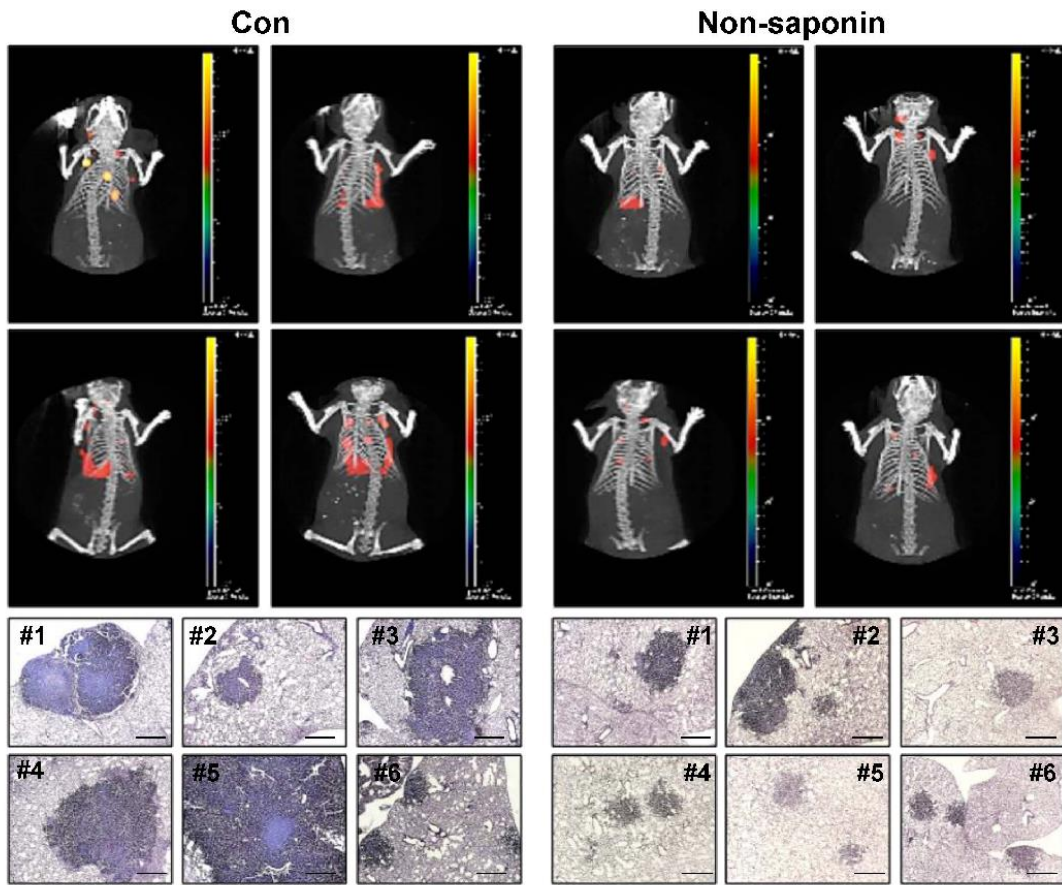
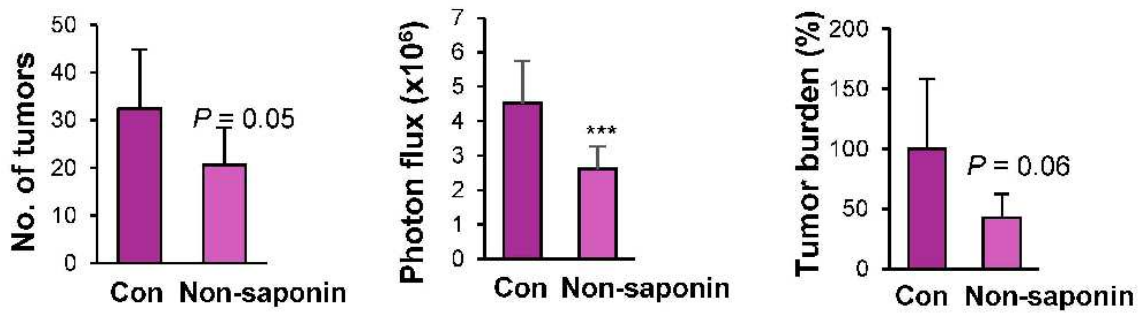
administered with vehicle or non-saponin fraction for eight weeks, and the bioluminescence images were examined by IVIS analysis. As shown in **Figure 2-4A**, non-saponin-treated mice markedly exhibited decreased lung tumor formation compared to the vehicle-treated mice. Microscopic evaluation of lung tumor formation showed significantly decreased tumor number, tumor volume, and tumor burden in mice treated with the non-saponin fraction compared to vehicle-treated mice (**Figure 2-4B**). These findings indicated the potential antitumor activity of *P. ginseng* non-saponin fraction.

To identify the active compound in the non-saponin fraction that effectively suppresses NSCLC non-CSCs and CSCs, we separated the non-saponin fraction into six sub-fractions (F1 to F6) (**Figure 2-5A**) and tested their effects on the NSCLC cell viability and sphere-forming ability. **Figures 2-5B, C** showed that F2 was the most effective fraction to suppresses non-CSC viability and sphere-forming activity. The chromatographic and instrumental analysis revealed the major component of F2 is panaxynol [112].



**Figure 2-3. The non-saponin fraction of *P. Ginseng* disrupts the HSP90 function and viability of both non-CSC and CSCs.**

The total extraction from *P. ginseng* was separated into non-saponin and saponin fractions, as shown in the schematic diagram (A). (B) The effects of saponin and non-saponin fractions on HSP90 and HIF1 $\alpha$  interaction was determined by immunoprecipitation using anti-Hif1 $\alpha$  antibody. (C) H1229 cells were treated with saponin or non-saponin fraction (50 $\mu$ g/ml) for 6 hours under normoxia (20% O<sub>2</sub>) and hypoxia (1% O<sub>2</sub>) conditions. The protein expressions were determined by western bot analysis. (D) H1299 cells were treated with saponin and non-saponin fraction at various concentrations for 48 hours, and cell viability was determined by MTT assay. (E) H1299 cells were seeded onto the low-attached 96-well and cultures in spheroid medium containing various saponin or non-saponin fraction concentrations until forming spheres. Con: control; S: Saponin fraction; N: non-saponin fraction. The bar represented mean  $\pm$  SD, \*P<0.05, \*\*P<0.01, \*\*\*P<0.001 as determined by the two-tailed Student's t-test compared with the vehicle-treated cells.

**A****B**

**Figure 2-4. The effects of the *P.ginseng* non-saponin fraction on lung tumorigenesis.**

(A) The antitumor activity of non-saponin fraction in  $Kras^{G12D/+}$ -driven-spontaneous lung tumorigenesis model.  $Kras^{G12D/+}$  mice were orally treated with vehicle or non-saponin fraction every day. After eight weeks, the representative bioluminescence images of  $Kras$  mice were assessed by IVIS Imaging analysis (top). The lung tumor nodules in the vehicle and non-saponin fraction-treated mice were accessed by H&E staining (bottom). Scale bar: 20  $\mu$ m. (B) The evaluation of lung tumor formation of non-saponin fraction-treated mice. The bar represented mean  $\pm$  SD, \* $P < 0.05$ , \*\* $P < 0.01$ , \*\*\* $P < 0.001$  as determined by the two-tailed Student's t-test compared with the vehicle-treated cells.

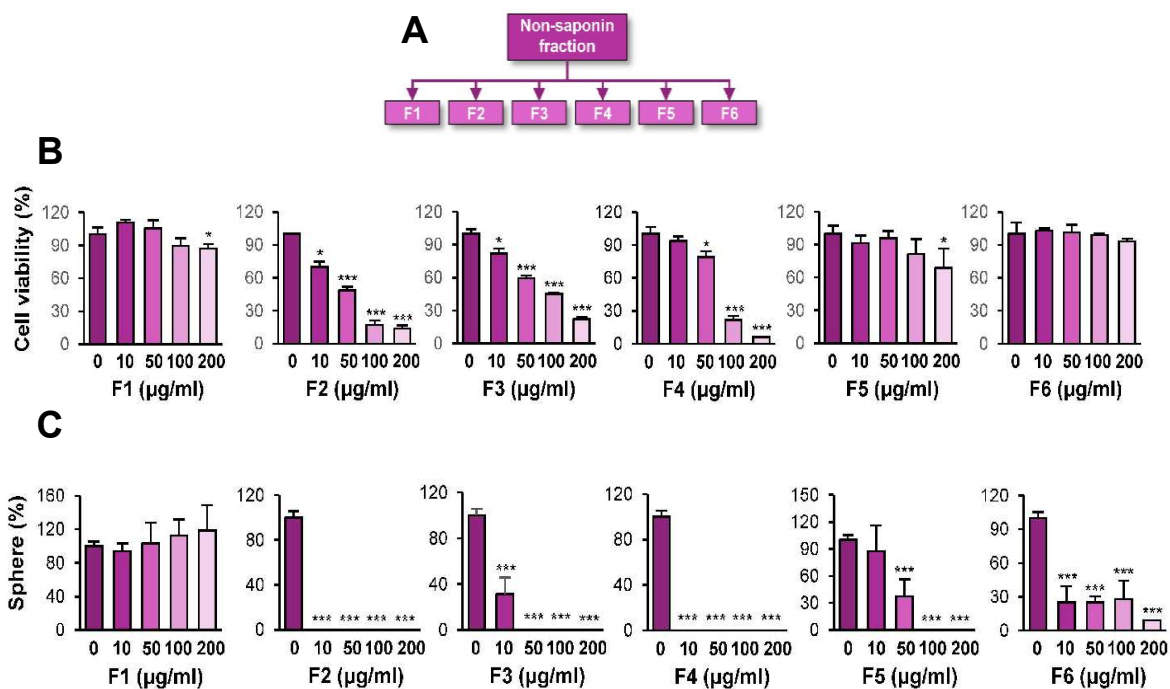


**Figure 2-5. The inhibitory effect of six non-saponin sub-fractions on H1299's cell viability.**

(A) The schematic diagram illustrates the separation of six non-saponin fraction sub-fractions. (B, C) The effects of the six subfractions on H1299 cell viability and sphere-forming ability. H1299 cells were treated with vehicle or six non-saponin subfractions (F1-F6) for 48 hours, and cell viability was determined by MTT assay (B). H1299 cells were seeded on low-attached 96-well plates and cultured in a sphere medium containing various concentrations of six non-saponin sub-fractions (F1-F6) until forming spheres (C). The number of spheres was analyzed using ImageJ software. The bar represented mean  $\pm$  SD, \* $P < 0.05$ , \*\* $P < 0.01$ , \*\*\* $P < 0.001$  as determined by the two-tailed Student's t-test compared with the vehicle-treated cells.

### **Panaxynol suppresses the function of HSP90 in NSCLC cells.**

I next investigated whether panaxynol suppresses HSP90 function in NSCLC cells. As shown in **Figure 2-6A**, dose-dependent treatment with panaxynol suppressed the total and phosphorylated expression of various oncogenic proteins regulated by HSP90 function [93, 113] in NSCLC cells. Additionally, I observed the decreased expression of angiogenic factors regulated by the IGF-axis (bFGF, PDGF) [38] in NSCLC cells treated with panaxynol. Consistent results were observed in the panaxynol-treated CSC population. Western blot analysis revealed the decreased expression of phosphorylated IGF-1R, EGFR, and Akt in H1299 spheres (**Figure 2-6B**). I further investigated the effect of panaxynol on HSP90-HIF1 $\alpha$  interaction. As expected, panaxynol markedly disrupted the interaction of HSP90 and HIF1 $\alpha$  (**Figure 2-6C**). Moreover, dose-dependent treatment of panaxynol suppressed HIF1 $\alpha$  level, results in decreased protein and mRNA expression of VEGF- a well-known target gene regulated by HIF1 $\alpha$  (**Figure 2-6D**). Consistently, the modulation HRE (HIF1 $\alpha$  response element) activity of NSCLC cells by panaxynol treatment was confirmed by HRE reporter assay (**Figure 2-7A**). Given that panaxynol treatment decreased the expression of angiogenic factors such as bFGF, PDGF, and VEGF, I next investigated the effect of panaxynol on the angiogenetic activity of NSCLC cells. HUVEC cells were incubated with conditioned media (CM) collected from panaxynol-treated H1299 cells experienced significantly decreased tube formation compared to those incubated with CM collected from vehicle-treated cells (**Figure 2-7B**). These results suggested the anti-angiogenic activity and the suppressive HSP90 function ability of panaxynol in NSCLC. Interestingly, panaxynol treatment did not affect the expression of HSP90 and HSP70 in monolayer cultured NSCLC cells (**Figure 2-8**). To assess whether panaxynol exerts the antitumor activities through inhibition of HSP90 function. I established the H1299 cells silenced HSP90 expression by stable transfection of HSP90

shRNAs. The silencing of HSP90 markedly decreased the sphere-forming and colony-forming abilities of H1299 cells. However, panaxynol treatment showed no effects on H1299 shHSP90 cells (**Figure 2-9A, B**). Panaxynol suppressed Akt expression in H1299 shEV cells but not in shHSP90 cells (**Figure 2-9C**). These results suggest that panaxynol exerts the antitumor effect through the disruption of HSP90 function.

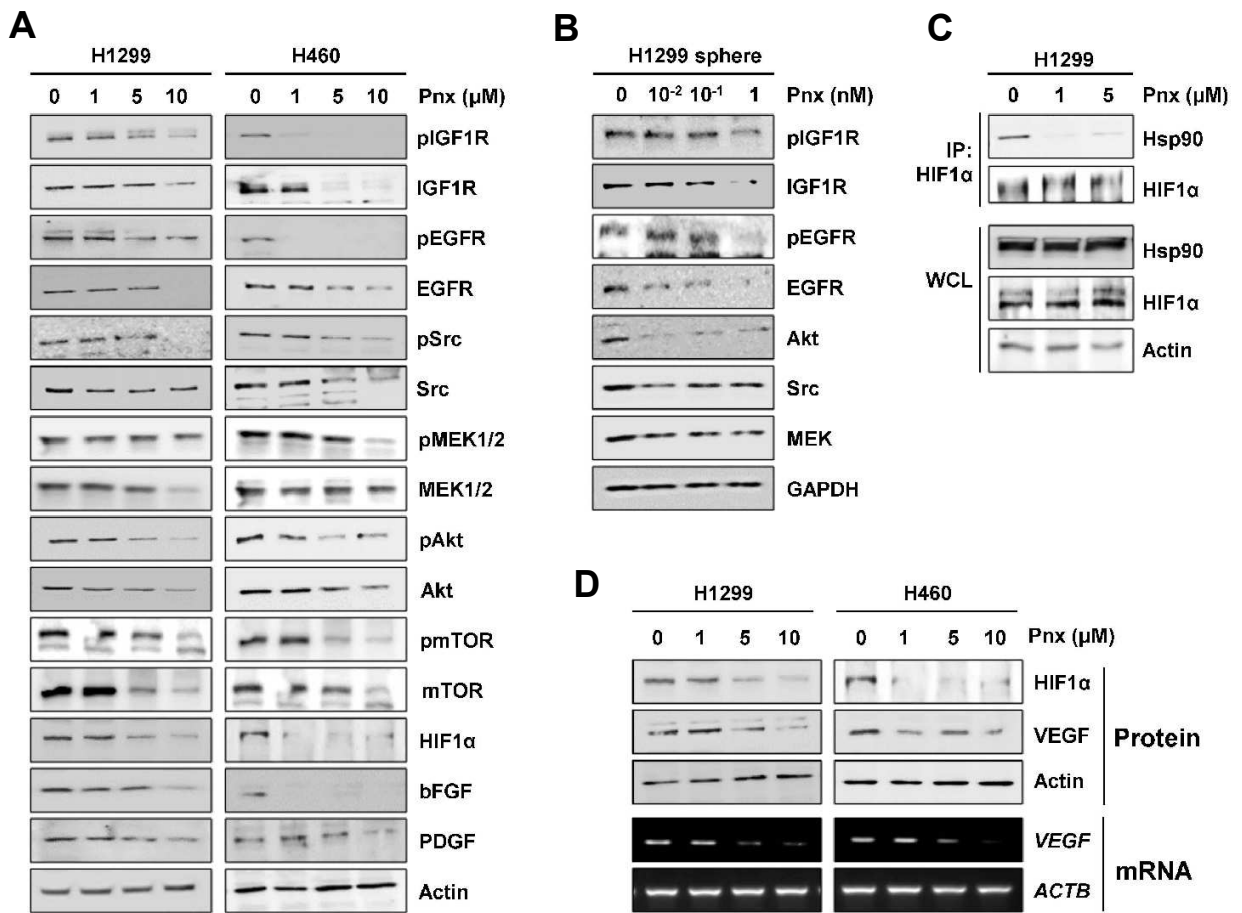


**Figure 2-6. Panaxynol suppresses HSP90 function in NSCLC cells.**

(A) The decreased expression of HSP90 clients in panaxynol-treated H1299 and H460 cells. The cells were dose-dependently treated with panaxynol for 48 hours, and the expression of HSP90 client proteins was determined by western blot analysis. (B) The decreased expression of total and phosphorylated forms of IGF1R, EGFR, Akt, Src, Mek in the H1299 spheres was determined by western blot analysis. (C) Panaxynol disrupts the interaction between HSP90 and HIF1α was determined by immunoprecipitation assay. H1299 cells were treated with vehicle or panaxynol for 6 hours under hypoxia condition. The cell lysates were prepared and subjected to immunoprecipitation using an anti-HIF1α antibody, followed by western blot analysis. (D) The decreased expression of HIF1α and its target gene VEGF by panaxynol was determined by western blot (upper) and RT-PCR (lower) analysis.

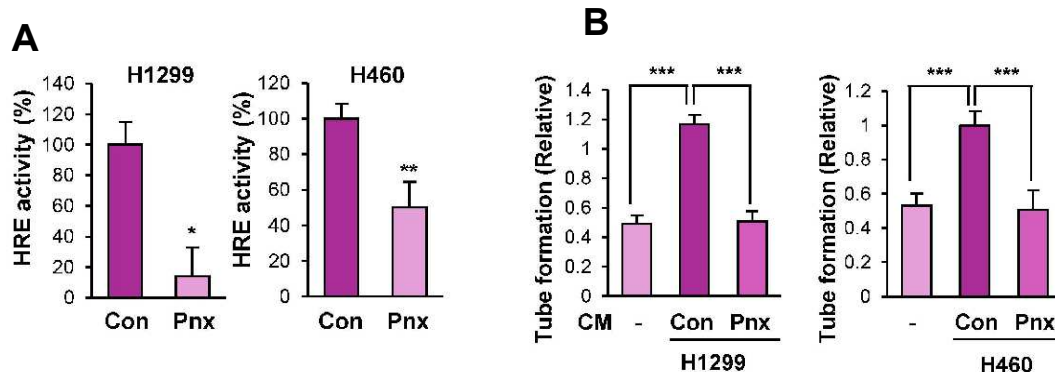


**Figure 2-7. Panaxynol suppresses HRE activity and tube formation of HUVEC cells.**

(A) Panaxynol suppresses HRE activity under hypoxic conditions. H1299 and H460 cells were transiently transfected with pSV40 promoter-EpoHRE-Luc for 48 hours and maintained in a medium containing vehicle or panaxynol (10  $\mu$ M) under hypoxia condition. The HRE activity was determined by Luciferase assay. (B) HUVEC cells were treated with media and CM derived from the vehicle or panaxynol-treated H1299 cells. In the tube formation assay, three branch-point was determined as one tube. The bar represented the mean  $\pm$  SD, \*P<0.05, \*\*\*P<0.01, were determined by the two-tailed Student's t-test compared with the media or vehicle-treated cells.

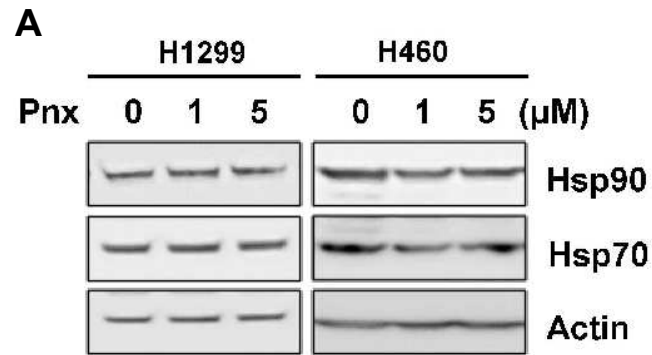


**Figure 2-8. Panaxynol treatment does not alter HSP70 expression.**

Panaxynol treatment did not change HSP90, HSP70 expression in NSCLC cells. H1299 and H460 cells were cultured in the medium containing the vehicle or panaxynol for 48 hours. The cell lysates were prepared, and the protein expression of HSP90 and HSP70 were determined by western blot analysis.

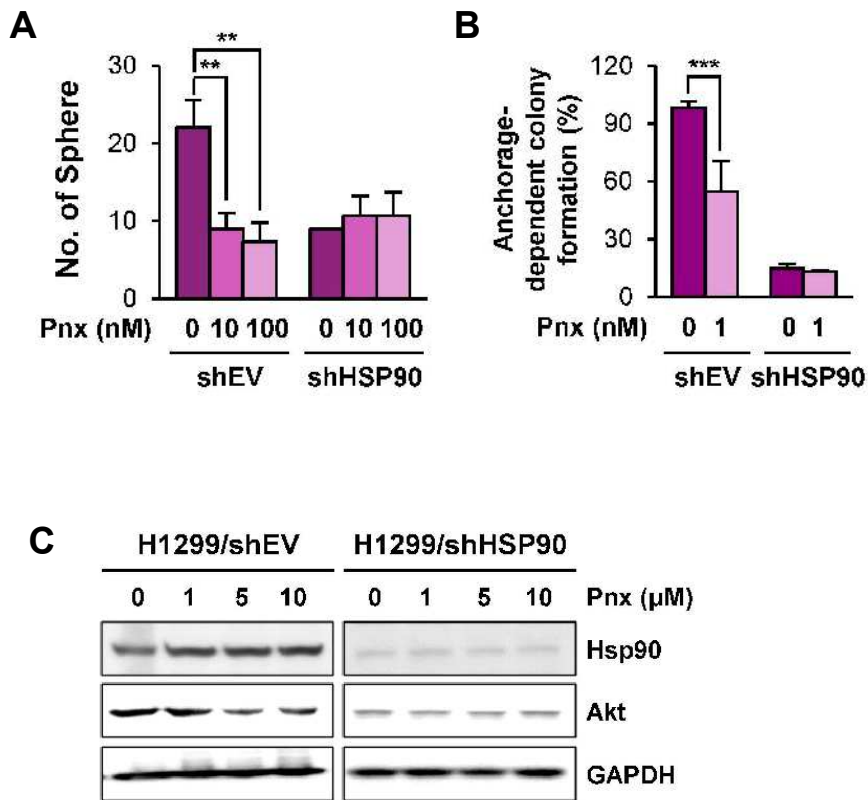


**Figure 2-9. The effect of panaxynol on the sphere-forming ability and anchorage-dependent-colony formation in H1299shEV and shHSP90 cells.**

H1299/shEV and H1299/shHSP90 cells were subjected to sphere-forming (A) and anchorage-dependent colony-forming assay (B) in the media containing vehicle or panaxynol. (C) H1299/shEV and H1299/shHSP90 cells were treated with vehicle or panaxynol in monolayer conditions. The cell lysates were prepared. The expression of HSP90 and Akt were determined by western blot analysis. The bar represented mean  $\pm$  SD, \*\* $P < 0.01$ , \*\*\* $P < 0.001$ , as determined by the two-tailed Student's t-test compared with the corresponding vehicle-treated cells.

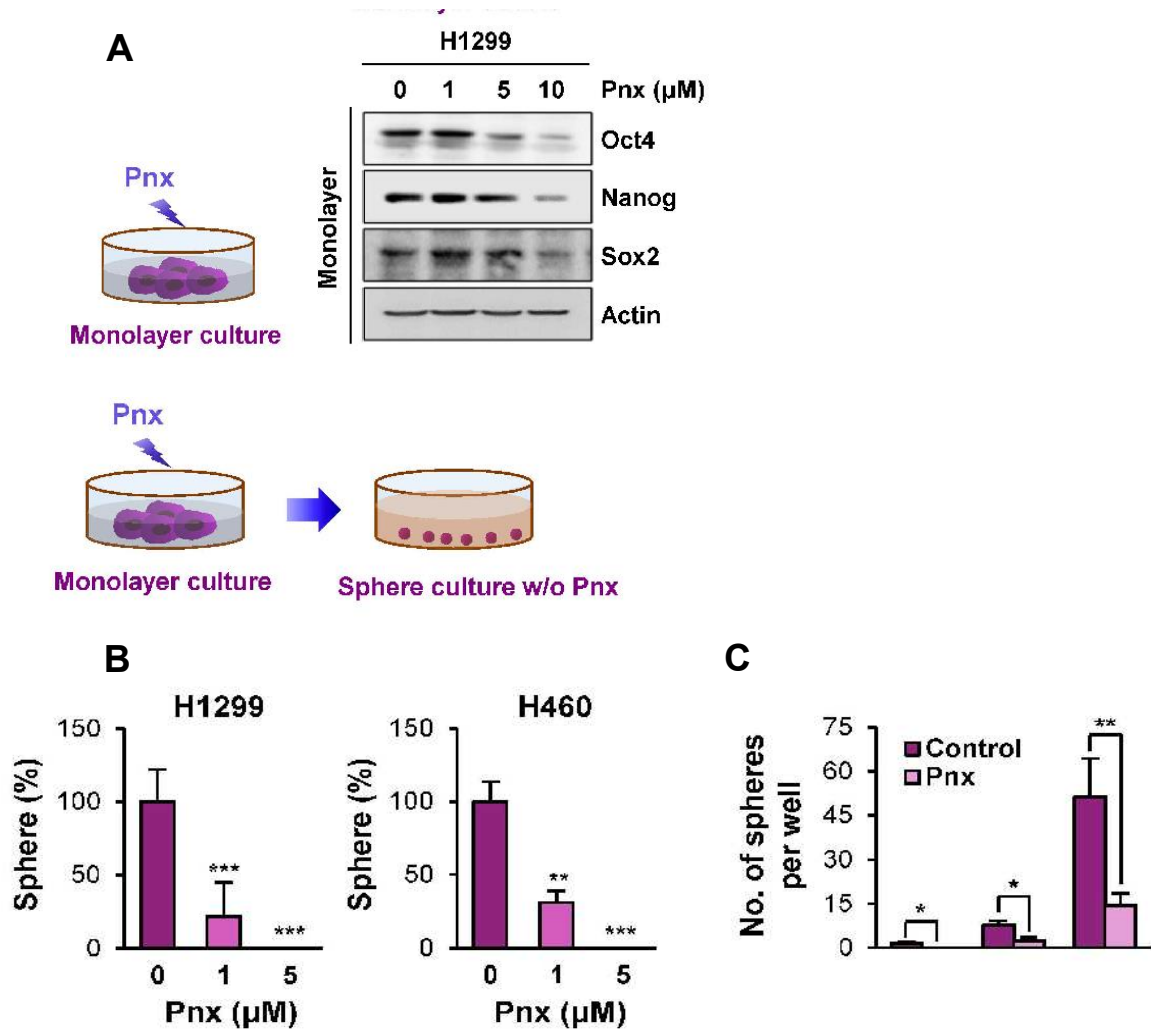
**Panaxynol inhibits both the CSC and non-CSC population of NSCLC by inducing apoptosis.**

I further investigated the selective inhibitory effects of panaxynol on CSC. Panaxynol dose-dependently reduced expression of CSC markers (Oct4, Sox2) in monolayer-cultured H1299 cells (**Figure 2-10A**). Additionally, panaxynol-treated cells displayed significantly decreased sphere-forming ability than the vehicle-treated cells (**Figure 2-10B**). Serial numbers of panaxynol-treated cells exhibit decreased sphere-forming ability, as shown in the *in vitro* serial dilution assay (**Figure 2-10C**). Given that chemoresistance is the characteristic of cancer stemness [114], I examined the effect of panaxynol on NSCLC cells acquired chemoresistance. The experiments were performed using the two NSCLC cell lines (H226B, H460) and their corresponding sublines (designated “R/”) that acquired resistance to paclitaxel (H226B/R and H460/R) [115]. **Figure 2-11A** showed that nanomolar concentrations of panaxynol suppressed the sphere-forming ability of both naïve and chemoresistant cells. Aldehyde dehydrogenase (ALDH) has been considered the universal marker for CSC; I next examined the anti-CSC activity of panaxynol by assessing the ALDH<sup>high</sup> population. As shown in **Figure 2-11B**, ALDH<sup>high</sup> H1299 population was also decreased by panaxynol treatment. Moreover, the panaxynol-treated CSC subpopulation underwent apoptosis, as evidenced by inducing caspase3 and its substrate poly-(ADP-ribose) polymerase (PARP) cleavages (**Figure 2-12A**). Consistently, the Hoechst staining results showed significantly increased apoptosis-related chromatin condensation in panaxynol-treated H1299 spheres than vehicle-treated spheres (**Figure 2-12B**). Co-treatment with caspase3 inhibitor (Z-DEVD-FMK) significantly abrogated panaxynol-induced apoptotic events, including caspase3 cleavage (**Figure 2-12C**), apoptosis-related chromatin condensation (**Figure 2-12B**), and sphere-forming ability

(**Figure 2-12D**). These results indicate that panaxynol treatment suppresses CSC by inducing CSC apoptosis.

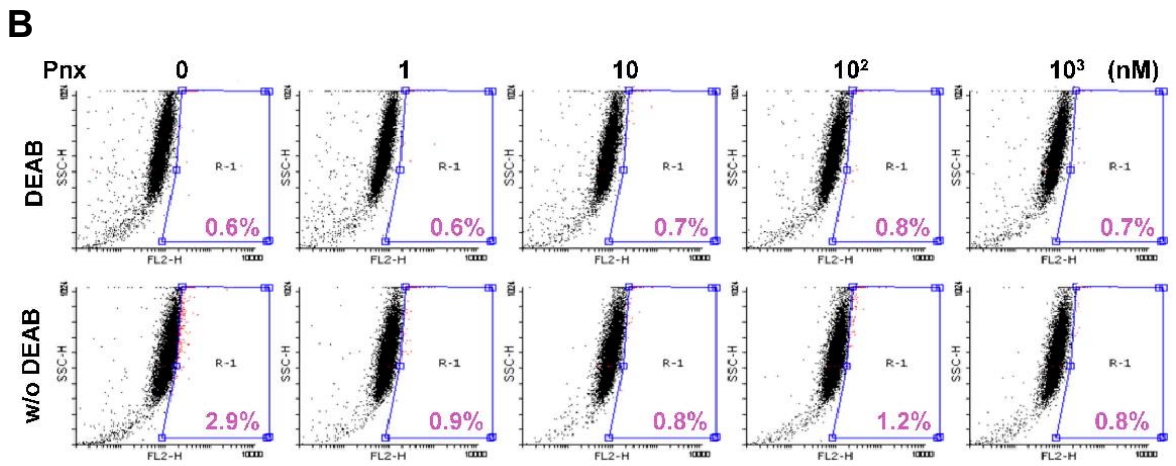
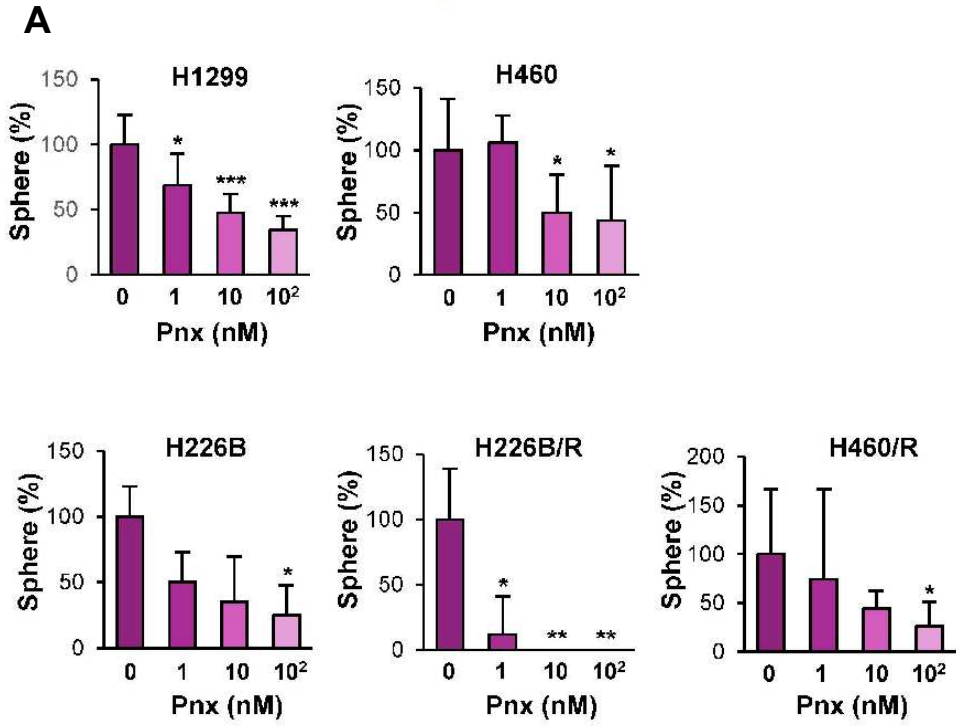
I next assessed the effect of panaxynol on the ability of CSCs to form tumors *in vivo*. The serial numbers of the ALDH<sup>high</sup> population isolated from the vehicle and panaxynol-treated cells were inoculated into NOD/SCID mice's flank. Mice inoculated with the ALDH<sup>high</sup> population from panaxynol-treated cells displayed significantly decreased tumor formation than those carrying the ALDH<sup>high</sup> population of vehicle-treated cells (**Figure 2-12E**). I further investigated the effect of panaxynol on the non-CSC populations of NSCLC cells. KRAS mutation and TP53's loss function implicated in the self-renewal ability of CSCs [116, 117] and NSCLC development [118] have been described previously. Thus, I assessed the effect of panaxynol on derivatives of HBE cell lines (HBEs) carrying mutant KRAS (HBE/KRAS<sup>G12V</sup>), siRNA mediated loss of TP53 (HBE/TP53i), or both(HBE/KRAS<sup>G12V</sup>; TP53i) [119] and observed the inhibitory effect of panaxynol on the viability of these cells (**Figure 2-13**). Panaxynol inhibited various NSCLC cells with IC50 of 5  $\mu$ M/L, which is significantly higher than IC50 in the sphere-forming assay (**Figure 2-14**), suggesting that low doses of panaxynol effectively eradicate CSC than the non-CSC population. Moreover, panaxynol treatment did not affect the viability of several normal cells that originated from various organs (**Figure 2-15**). Panaxynol also suppressed anchorage-dependent and anchorage-independent colony-forming abilities of NSCLC cells (**Figure 2-16**). Panaxynol induced the non-CSC apoptosis, as illustrated in **Figure 2-17A** with the increased sub G0/G1 population. Western blot analysis showed that treatment with panaxynol induced caspase3 and PARP cleavages (**Figure 2-17B**). Moreover, the effects of panaxynol on colony-forming ability and caspase3 cleavages were ablated by the presence of DEVD- a caspase3 inhibitor (**Figure 2-17C, D**). Altogether, these findings

indicate that panaxynol selectively eliminates CSC at nanomolar concentrations and the bulk non-CSC at micromolar concentrations without inducing toxicity in normal cells.



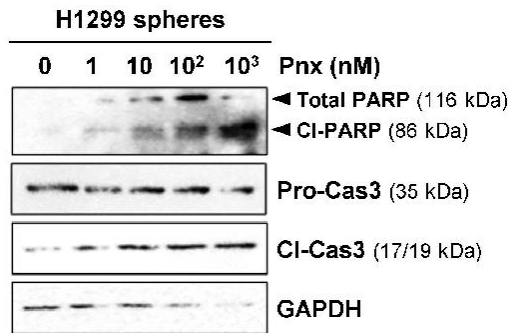
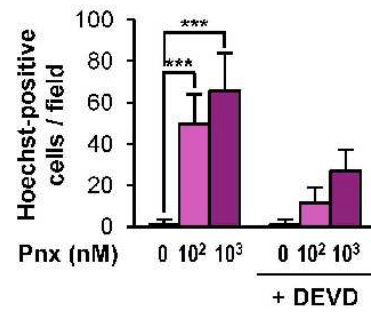
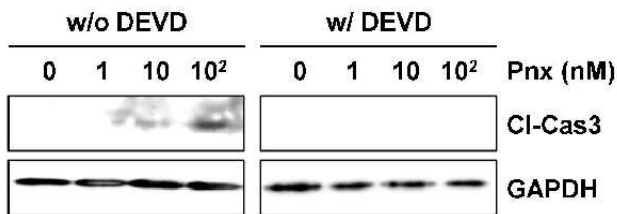
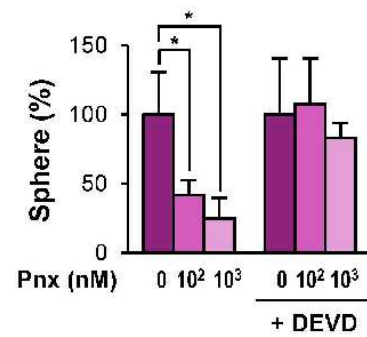
**Figure 2-10. Panaxynol inhibits NSCLC CSC populations.**

(A) Decreased expression of CSC markers in H1299 cells by panaxynol treatment. Monolayer cultured H1299 cells were treated with increasing doses of panaxynol for 48 hours. The expression of CSC markers was determined by western blot analysis. (B) Panaxynol inhibits CSC populations. H1299 and H460 cells cultured in monolayer conditions were pretreated with panaxynol and then seeded on low-attached 96-well plates (left) in a sphere medium until forming spheres. The serial numbers of cells were subjected to sphere formation assay (C). The bar represented mean  $\pm$  SD, \* $P < 0.05$ , \*\* $P < 0.01$ , \*\*\* $P < 0.001$ , as determined by the two-tailed Student's t-test compared with the vehicle-treated cells.



**Figure 2-11. Panaxynol inhibits NSCLC cells in sphere culture conditions and ALDH activity of H1299 cells.**

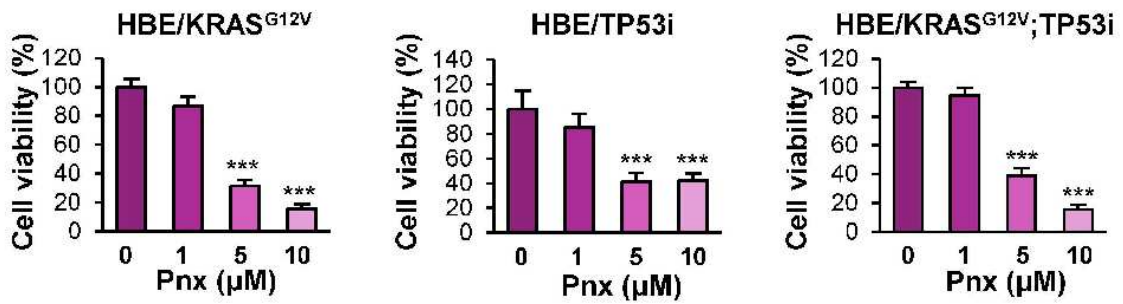
(A) The effect of panaxynol on the sphere-forming ability of NSCLC cells. The NSCLC cells (naïve and acquired chemoresistance) were seeded on low-attached 96-well plates in a sphere medium containing vehicle or nanomolar concentrations of panaxynol until forming spheres. (B) Panaxynol decreased the ALDH<sup>high</sup> populations in H1299 cells. H1299 cells were treated with nanomolar concentrations of panaxynol. An aliquot of each cell sample was treated with AldeRed 588-A in the presence or absence of an ALDH inhibitor (DEAB), followed by FACS analysis. The DEAB sample is a negative control. The shift of fluorescence is defined in the gating area, presenting the ALDH<sup>high</sup> population. The bar represented mean  $\pm$  SD, \*P<0.05, \*\*P<0.01, \*\*\*P<0.001, as determined by the two-tailed Student's t-test compared with the vehicle-treated cells.

**A****B****C****D****E**

No. of cells	Con	Pnx
50	2/6	1/6
500	4/6	1/6
5000	4/6	4/6

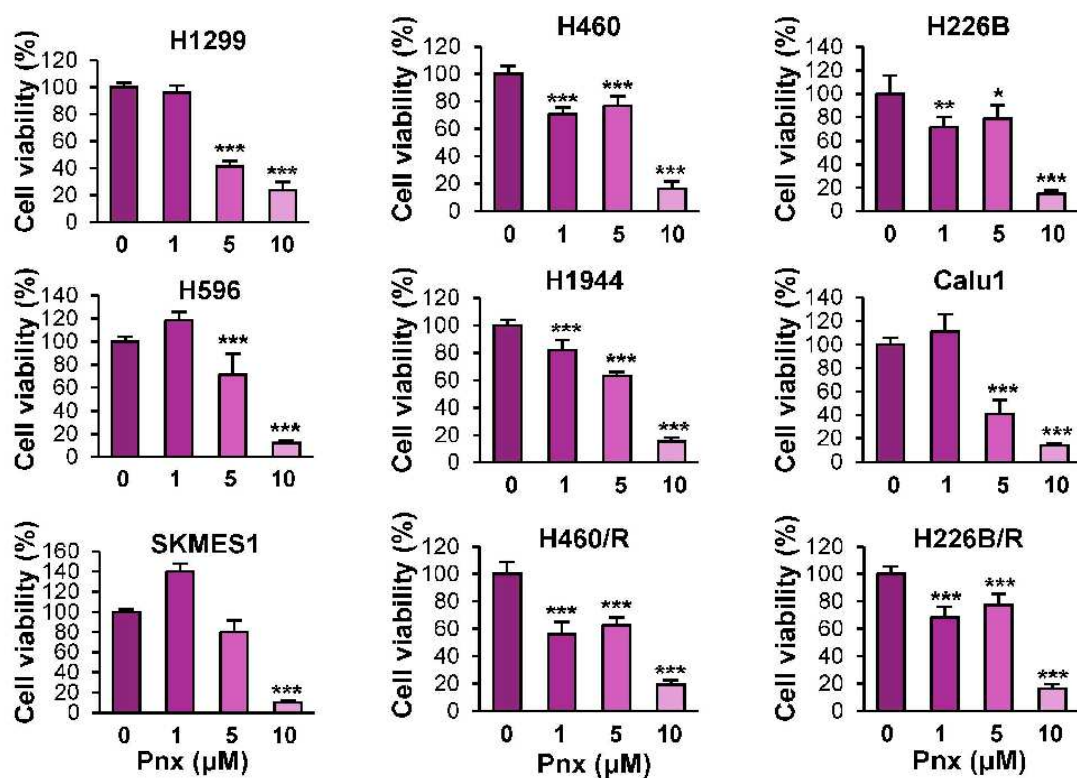
**Figure 2-12. Panaxynol induces apoptosis in H1299 cells grown in sphere-forming conditions.**

(A-D) Panaxynol induces apoptosis in H1299 cells grown in sphere condition. (A) H1299 cells were then seeded on low-attached 96-well plates in a sphere medium containing nanomolar concentrations of panaxynol until forming spheres. The expression of total and cleaved forms of PARP and caspase3 were determined by western blot analysis. The apoptotic-related chromatin condensation was determined by the Hoechst staining (B), and the cleaved caspase3 expression was determined by western blot analysis (C). (D) H1299 cells grown in sphere-forming conditions were treated with nanomolar concentrations of panaxynol in the presence and absence of caspase3 inhibitor-DEVD. The sphere number was determined by ImageJ software. (E) Panaxynol suppresses the tumor formation potential of the CSC population. Serial dilution tumor propagation assay using the ALDH<sup>high</sup> population of the vehicle or panaxynol-treated H1299 cells. The serial numbers of cells were injected into the flank of NOD/SCID mice, and the tumor incidence was observed. The bar represented mean  $\pm$  SD, \*P<0.05, \*P<0.01, \*P<0.001 were determined by the two-tailed Student's t-test compared with the vehicle-treated cells.



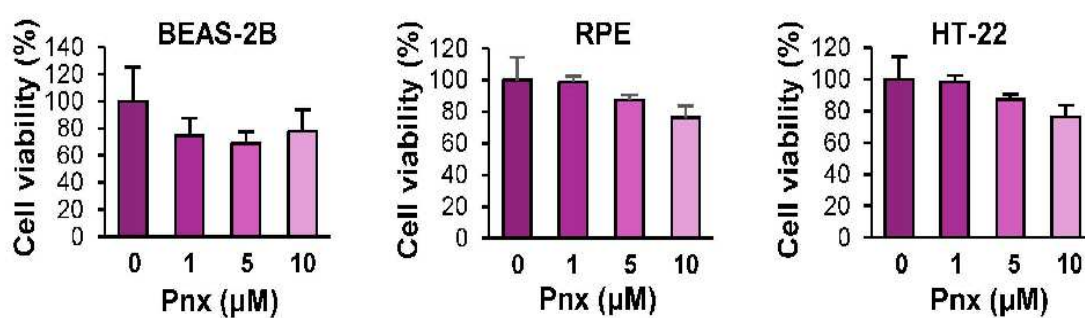
**Figure 2-13. The effect of panaxynol on the viability of HBE cells with KRAS mutant or p53 loss function.**

The effect of panaxynol on the viability of HBE cells carrying, loss function of p53 or both was determined by MTT assay. The bar represented mean  $\pm$  SD, \*\*\*P<0.001, as determined by the two-tailed Student's t-test compared with the vehicle-treated cells.



**Figure 2-14. The effect of panaxynol on the viability of naïve or acquired anticancer drug resistance NSCLC cells**

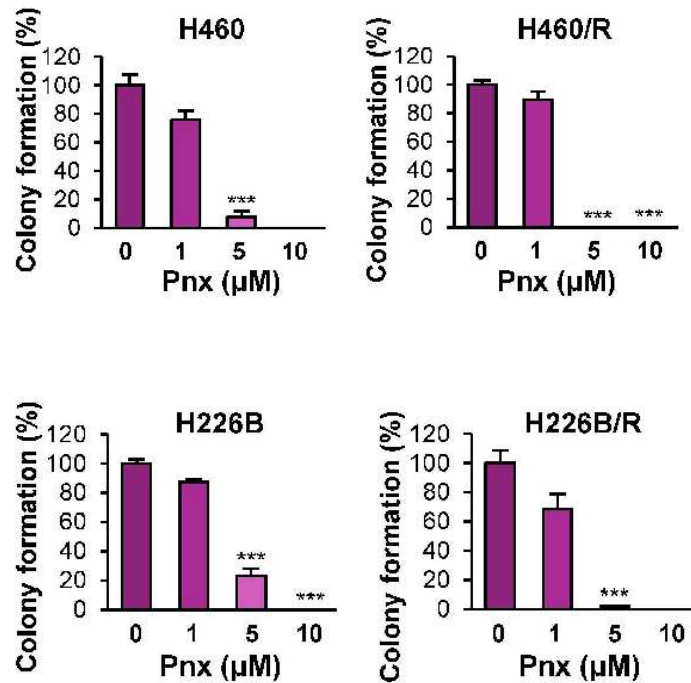
The viability of vehicle and panaxynol-treated NSCLC cells (naïve and chemoresistant cells) was determined by MTT assay. The bar represented mean  $\pm$  SD, \* $P < 0.05$ , \*\* $P < 0.01$ , \*\*\* $P < 0.001$ , as determined by the two-tailed Student's t-test compared with the vehicle-treated cells.



**Figure 2-15. The effect of panaxynol on the viability of normal cells.**

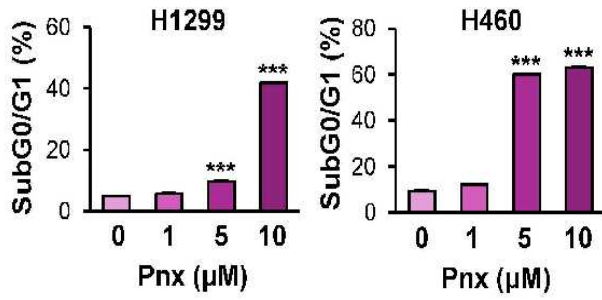
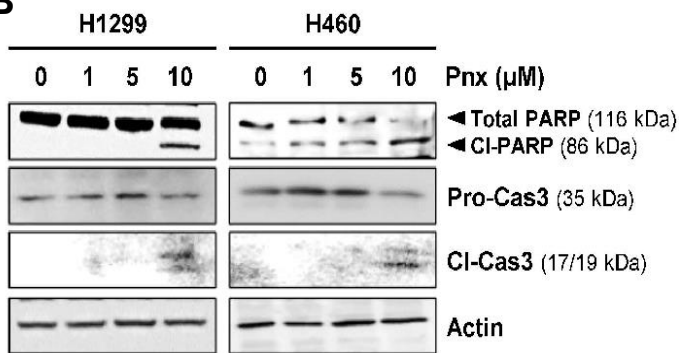
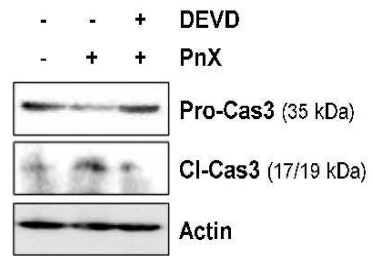
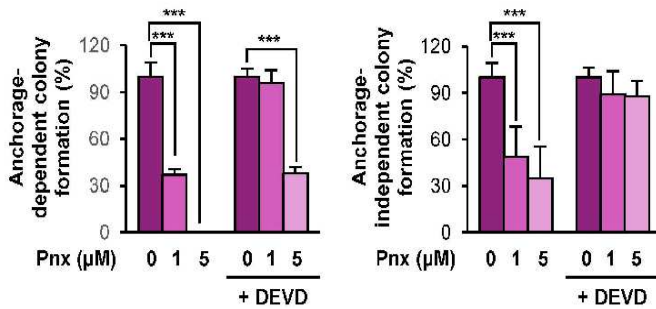
The viability of vehicle or panaxynol-treated normal cells was determined by MTT assay.

The bar represented mean  $\pm$  SD, \* $P < 0.05$ , \*\* $P < 0.01$ , \*\*\* $P < 0.001$ , as determined by the two-tailed Student's t-test compared with the vehicle-treated cells.



**Figure 2-16. Panaxynol suppresses the anchorage-dependent colony-forming ability of NSCLC cells.**

The colony-forming ability of the vehicle and panaxynol-treated NSCLC cells was determined by anchorage-dependent colony formation assay. The bar represented mean  $\pm$  SD, \*\*\* $P < 0.001$ , as determined by the two-tailed Student's t-test compared with the vehicle-treated cells.

**A****B****C****D**

**Figure 2-17. Panaxynol induces apoptosis in NSCLC cells grown in monolayer conditions.**

H1299 and H460 cells were treated with panaxynol for 48 hours and subjected to cell cycle analysis (A) or western blot analysis (B). (C) H1299 cells were treated with panaxynol in the presence or absence of DEVD. The expression of cleaved caspase3 was determined by western blot analysis (C), and the colony-forming ability was determined by anchorage-dependent colony formation assay (D). The colony formation was accessed by ImageJ analysis. The bar represented mean  $\pm$  SD, \*\*\*P<0.001, as determined by the two-tailed Student's t-test compared with the vehicle-treated cells.

### **Panaxynol suppresses NSCLC tumor growth *in vivo*.**

To examine the effect of panaxynol on lung tumor formation, I tested the antitumor activity of panaxynol in the  $Kras^{G12D/+}$ -driven-spontaneous lung tumor mouse model [115], in which  $Kras^{G12D/+}$  mice were treated with the vehicle and panaxynol for eight weeks. The panaxynol-treated mice exhibited lung tumor formation significantly compared to the vehicle-treated mice (**Figure 2-18A**). The microscopic evaluation of lung tumor formation revealed the remarkably decreased tumor number, volume, and burden in panaxynol-treated mice compared with the corresponding control mice (**Figure 2-18B**). Moreover, I detected the increased cleaved caspase3 expression and decreased CD34, HIF1 $\alpha$ , and Oct4 expressions in tumors derived from panaxynol-treated mice compared to those derived from control mice (**Figure 2-18C**). The self-renewal ability contributing to the cancer cells' growth and survival is a hallmark of CSC [120]. To further examine whether panaxynol can suppress NSCLC tumor growth of CSC *in vivo*, I performed the H1299 xenograft model in which NOD/SCID mice were orally treated with either vehicle or panaxynol (50 and 100mg/kg). **Figure 2-19A, B** showed that panaxynol treatment remarkably suppressed the volume and weight of H1299 xenograft tumors. The proapoptotic and antiangiogenic activities of panaxynol were confirmed by immunofluorescence staining of cleavages caspase3, CD34, and HIF1 $\alpha$  in xenograft tumor tissues (**Figure 2-19C**). To confirm the anti-CSC activity of panaxynol *in vivo*, I performed the serial dilution tumor propagation assay. Serial numbers of tumor cells derived from the vehicle or panaxynol-treated mice were inoculated into the right flank of NOD/SCID mice. As shown in **Figure 2-19D**, tumor cells derived from panaxynol-treated mice exhibited decreased tumor formation compared to those derived from control mice. 4/6 mice injected with 50000 tumor cells from control mice developed tumors, whereas only 1/6 mice injected with tumor cells derived from panaxynol-treated mice displayed tumor formation. Moreover, treatment of panaxynol did

not affect the body weight or induce any inflammation signs in H1299 xenograft or  $Kras^{G12D/+}$  mice (data not shown), suggesting the minimal toxicity of panaxynol. Altogether, these results suggest that panaxynol suppresses CSC and NSCLC tumor formation *in vivo*.

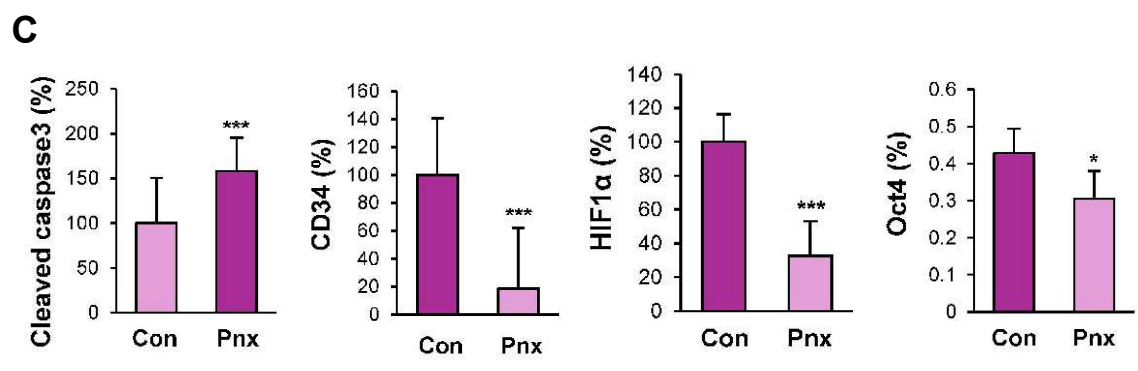
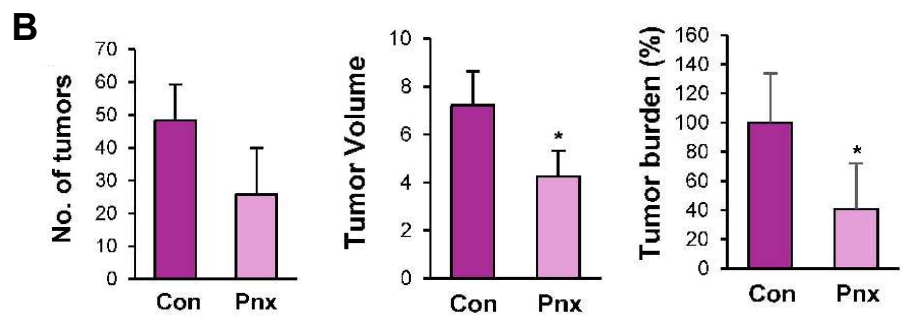
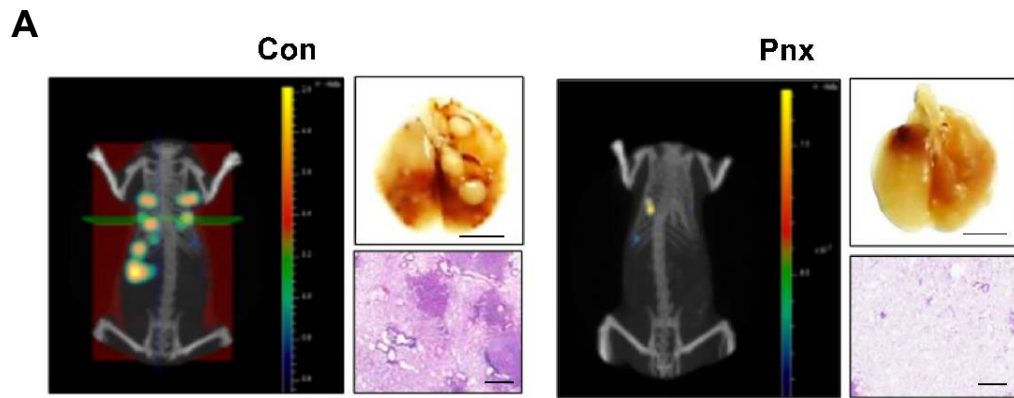
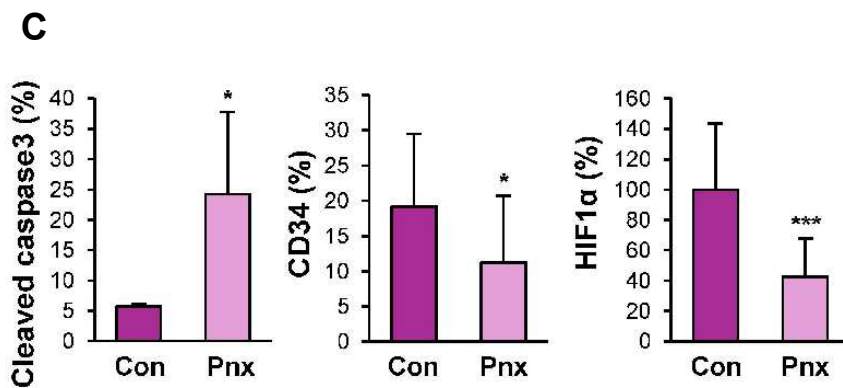
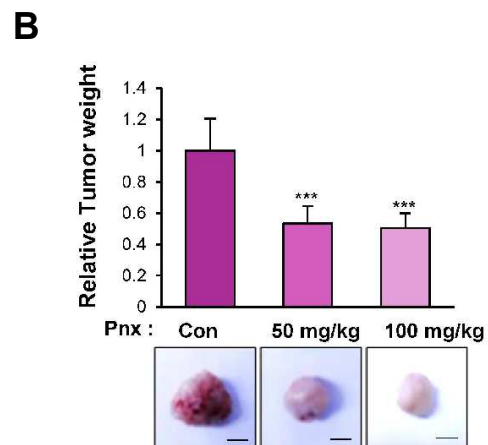
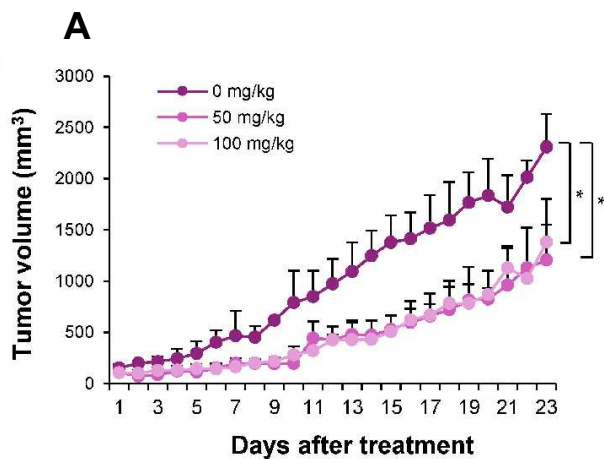


**Figure 2-18. The antitumor activities of panaxynol on  $Kras^{G12D/+}$ -driven-spontaneous lung tumor formation.**

$Kras^{G12D/+}$  mice were treated with the vehicle or panaxynol for 8 weeks. Representative images of bioluminescence imaging (top) and gross observation (right, top, scale bar: 5mm) was determined by IVIS analysis, and tumor formation was demonstrated by H&E staining of lung tissues (right, bottom, scale bar 20  $\mu$ m) from  $Kras^{G12D/+}$  mice treated with vehicle or panaxynol (A). The quantification of tumor multiplicity, volume, and burden in lung tissues of vehicle or panaxynol treated mice was determined by histological and microscopic evaluation (B). (C) The expression of cleaved caspase3, HIF1 $\alpha$ , CD34, and Oct4 in lung tumor-derived from the vehicle or panaxynol-treated mice was determined by immunofluorescence staining. The quantification was assessed using ImageJ software. The bar represented mean  $\pm$  SD, \*P<0.05, \*\*\*P<0.01, as determined by the two-tailed Student's t-test compared with the vehicle-treated mice.



**D**

No. of cells	Con	Pnx
500	2/6	0/6
5000	2/6	0/6
50000	4/6	1/6

**Figure 2-19. The antitumor effect of panaxynol in the H1299 xenograft model**

H1299 cells were injected into the flank of NOD/SCID mice until the tumors reach the volume of 150mm<sup>3</sup>. Mice were then administered with vehicle or panaxynol, and the tumor volume was measured every two days by the caliper. Panaxynol treatment reduces H1299 xenograft tumor volume (A) and tumor weight (B). Scale bar: 5 mm. (C) The expression of cleaved caspase3, CD34, and HIF1 $\alpha$  in tumor tissues derived from the vehicle or panaxynol-treated mice was determined by immunofluorescence staining. (D) Serial numbers of tumor cells isolated from the vehicle or panaxynol-treated mice were injected into the NOD/SCID mice, and tumor incidence was observed. The number of tumor-bearing mice over the number of total recipient mice (n=6) in each group was shown. The bar represented mean  $\pm$  SD, \*P<0.05, \*\*\*P<0.001 were determined by the two-tailed Student's t-test compared with the vehicle-treated mice.

## **5. DISCUSSION**

For the first time, this study demonstrates panaxynol, a polyacetylene compound isolated from the non-saponin fraction of *P.ginseng*, suppressed the non-CSC population at micromolar concentrations and CSC population at nanomolar concentrations in NSCLC by inducing apoptosis. Treatment with panaxynol did not induce the elevation of HSP70 and toxicity in normal cells. Furthermore, panaxynol exerts the antitumor effect by disrupting HSP90 function. Our *in vivo* results revealed the antitumor activity of panaxynol in *Kras*<sup>G12D/+</sup> -driven-spontaneous lung tumor formation and NSCLC xenograft mouse models. Panaxynol treatment inhibits the tumor formation of the CSC population by using *in vivo* serial dilution assay. These findings provide a potent strategy utilizing the natural compound targeting HSP90 for anti-cancer therapy in NSCLC.

CSC is the subpopulations within tumor cells with the self-renewal and differentiated capacity to give rise to various tumor cell types. Chemotherapies virtually eliminate the bulk of tumor cells while leaving behind the CSCs, results in tumor relapse from the survival CSCs after a long time of treatment. Accumulating studies show that CSCs contribute to tumor growth, relapse, metastasis, and anticancer drug resistance in several cancers, including NSCLC [121]. Therefore, targeting CSC could be an effective anticancer strategy. Given that CSC can survive in hostile conditions and promote tumorigenesis [122], identifying key molecules responsible for the self-renewal capacity and tumorigenicity is vital for developing CSC-treatment approaches. Previous studies demonstrate the crucial role of HSP90 in CSC homeostasis maintenance under stress environments [107] and increased expression of oncogenic HSP90 client proteins in the CSC population [107]; thus, I hypothesized that HSP90 inhibitor might be a novel strategy for anti-CSC therapy [95, 107]. HSP90 controls various cellular proteins' proper folding and the numerous HSP90 client proteins associated with cancer cell proliferation, survival, metastasis, and drug-resistance. High HSP90 expression correlates with the poor outcomes

in NSCLCS [123]. Thus, targeting HSP90 has been considered a promising strategy for anti-CSC in lung cancer. Several clinical trials have been conducted to identify the effective HSP90 inhibitors, especially those that suppress its N-terminal ATP binding pocket [95]. The N-terminal HSP90 inhibitors' significant concerns are its toxicity and HSP70-mediated cancer recurrence [97, 124]. Thus, identifying safety agents targeting HSP90 without inducing the elevation of HSP70 is urgently needed. Here, I examined the antitumor efficacy of panaxynol, a polyacetylene compound isolated from *P. ginseng* that suppresses HSP90 function. Panaxynol eradicates both NSCLC CSCs and the bulk non-CSCs populations while exhibits minimal toxicity to normal cells.

Previous studies have shown the antimicrobial, anti-inflammation, and antitumor activities of panaxynol [125]. Panaxynol inhibits cancer cell proliferation through the downregulation of E cyclin mRNA levels [126]. Treatment with panaxynol decreased breast cancer resistance protein (BCRP/ABCG2) [127]. Activation of the ATP-binding cassette (ABC) transporter protein, a marker for cancer stemness, is the cancer cells' mechanism to acquire multi-drug resistance. Moreover, the HSP90 impacts various oncogenic proteins related to anticancer drug resistance. In line with these findings, this study provides evidence as follows: 1) panaxynol suppresses viability, self-renewal, colony-forming ability in various NSCLC, and the acquired chemoresistant cells without HSP70 induction; 2) panaxynol suppresses various NSCLC cells' viability and the acquired chemoresistant subtypes while exhibiting no toxicity in normal cells; 3) no detectable changes in body weight and inflammatory signs in panaxynol-treated mice after several months of treatment indicating the safety profile of panaxynol; 4) panaxynol induces CSC and non-CSCs apoptosis, which evident by cleaved caspase3 and PARP upregulation. The apoptotic and antiangiogenic activity of panaxynol were confirmed by *in vitro* and *in vivo* experiments; 5) panaxynol suppresses lung tumor formation and the tumor initiation

capacity of NSCLC cells *in vivo*. All these above findings suggest that panaxynol is the effective natural HSP90 inhibitor that suppresses angiogenesis, tumor development and tumor resistance in NSCLCs.

## 6. CONCLUSION

In summary, chapter 2 highlights panaxynol as the novel natural HSP90 inhibitor that effectively suppresses both the CSCs and non-CSCs population without mediating the upregulation of HSP70. Panaxynol exhibits antitumor effects on various NSCLC cells and the acquired chemoresistant cells without inducing cytotoxicity in normal cells. Moreover, panaxynol treatment inhibits lung tumor progression and tumor formation capacity of NSCLC cells *in vivo*. Therefore, it is promising to consider panaxynol as a novel anticancer compound providing a practical approach to target both non-CSC and CSCs in NSCLCs.

### **III. SUMMARY**

IGFBP-3 has been known as a tumor suppressor with antitumor, antiangiogenic, anti-cell-adhesion capacities in NSCLC and HNSCC. In chapter 1 of this study, I demonstrated the antimetastatic function of IGFBP-3 in NSCLC and HNSCC by mediating the ubiquitin-mediated proteasome degradation of vimentin expression through the cooperation with the E3 ligase FBXL14. This finding highlights the potential function of IGFBP-3 as a novel strategy to control metastasis progression in aerodigestive tract cancers.

Given that the raising of the CSC population contributing to tumor relapse and drug resistance and HSP90 is critical for the maintenance homeostasis of CSC under environmental stress, we identified the active compound from *P. ginseng* disrupts HSP90 function and effectively suppresses CSC viability. Chapter 2 of this study demonstrated the capacity of panaxynol as a natural HSP90 inhibitor, which suppresses both the non-CSC and CSC population in NSCLC while exhibits minimal toxicity in the normal cells. The findings open new windows for future drug development, especially utilizing natural compounds for patients with NSCLC.

Altogether, this study has provided promising strategies utilizing IGFBP-3 to suppress invasion and metastatic tumors in NSCLC and HNSCC; and panaxynol as a natural HSP90 inhibitor effectively suppresses both cancer stem and non-stem cells in NSCLC.

## **IV. REFERENCES**

- [1] F. Bray, J. Ferlay, I. Soerjomataram, R.L. Siegel, L.A. Torre, A. Jemal, Global cancer statistics 2018: GLOBOCAN estimates of incidence and mortality worldwide for 36 cancers in 185 countries, *CA Cancer J Clin*, 68 (2018) 394-424.
- [2] N. Vigneswaran, M.D. Williams, Epidemiologic trends in head and neck cancer and aids in diagnosis, *Oral Maxillofac Surg Clin North Am*, 26 (2014) 123-141.
- [3] D.E. Johnson, B. Burtneess, C.R. Leemans, V.W.Y. Lui, J.E. Bauman, J.R. Grandis, Head and neck squamous cell carcinoma, *Nature Reviews Disease Primers*, 6 (2020) 92.
- [4] T. Chen, J. Luo, R. Wang, H. Gu, Y. Gu, Q. Huang, Y. Wang, J. Zheng, C. Gu, X. Pan, J. Yang, Y. Yang, H. Zhao, Visceral pleural invasion predict a poor survival among lung adenocarcinoma patients with tumor size  $\leq 3$ cm, *Oncotarget*, 8 (2017) 66576-66583.
- [5] Z. Xu, Q. Yang, X. Chen, L. Zheng, L. Zhang, Y. Yu, M. Chen, Q. You, J. Sun, Clinical associations and prognostic value of site-specific metastases in non-small cell lung cancer: A population-based study, *Oncol Lett*, 17 (2019) 5590-5600.
- [6] J. Zhu, R. Zhou, Y. Wang, M. Yu, Perineural invasion as a prognostic factor in head and neck squamous cell carcinoma: a systematic review and meta-analysis, *Acta Oto-Laryngologica*, 139 (2019) 1038-1043.
- [7] S.L. Bhave, T.N. Teknos, Q. Pan, Molecular parameters of head and neck cancer metastasis, *Crit Rev Eukaryot Gene Expr*, 21 (2011) 143-153.
- [8] J.S. Lee, J.H. Hong, D.S. Sun, H.S. Won, Y.H. Kim, M.S. Ahn, S.Y. Kang, H.W. Lee, Y.H. Ko, The impact of systemic treatment on brain metastasis in patients with non-small-cell lung cancer: A retrospective nationwide population-based cohort study, *Scientific Reports*, 9 (2019) 18689.
- [9] C.L. Chaffer, R.A. Weinberg, A Perspective on Cancer Cell Metastasis, *Science*, 331 (2011) 1559-1564.
- [10] S. Lamouille, J. Xu, R. Derynck, Molecular mechanisms of epithelial-mesenchymal transition, *Nat Rev Mol Cell Biol*, 15 (2014) 178-196.
- [11] A. Dongre, R.A. Weinberg, New insights into the mechanisms of epithelial–mesenchymal transition and implications for cancer, *Nature Reviews Molecular Cell Biology*, 20 (2019) 69-84.
- [12] S.A. Mani, W. Guo, M.J. Liao, E.N. Eaton, A. Ayyanan, A.Y. Zhou, M. Brooks, F. Reinhard, C.C. Zhang, M. Shipitsin, L.L. Campbell, K. Polyak, C. Brisken, J. Yang, R.A. Weinberg, The epithelial-mesenchymal transition generates cells with properties of stem cells, *Cell*, 133 (2008) 704-715.
- [13] A.P. Morel, M. Lièvre, C. Thomas, G. Hinkal, S. Ansieau, A. Puisieux, Generation of breast cancer stem cells through epithelial-mesenchymal transition, *PLoS One*, 3 (2008) e2888.
- [14] C.L. Chaffer, B.P. San Juan, E. Lim, R.A. Weinberg, EMT, cell plasticity and metastasis, *Cancer Metastasis Rev*, 35 (2016) 645-654.
- [15] R.A. Battaglia, S. Delic, H. Herrmann, N.T. Snider, Vimentin on the move: new developments in cell migration, *F1000Res*, 7 (2018).
- [16] A. Tadokoro, N. Kanaji, D. Liu, H. Yokomise, R. Haba, T. Ishii, T. Takagi, N. Watanabe, N. Kita, N. Kadowaki, S. Bandoh, Vimentin Regulates Invasiveness and Is a Poor Prognostic Marker in Non-small Cell Lung Cancer, *Anticancer Res*, 36 (2016) 1545-1551.
- [17] Z. Ye, X. Zhang, Y. Luo, S. Li, L. Huang, Z. Li, P. Li, G. Chen, Prognostic Values of Vimentin Expression and Its Clinicopathological Significance in Non-Small Cell Lung Cancer: A Meta-Analysis of Observational Studies with 4118 Cases, *PLoS One*, 11 (2016) e0163162.
- [18] S. Liu, L. Liu, W. Ye, D. Ye, T. Wang, W. Guo, Y. Liao, D. Xu, H. Song, L. Zhang, H. Zhu, J. Deng, Z. Zhang, High Vimentin Expression Associated with Lymph Node Metastasis and Predicated a Poor Prognosis in Oral Squamous Cell Carcinoma, *Sci Rep*, 6 (2016) 38834.
- [19] P.F. Liu, B.H. Kang, Y.M. Wu, J.H. Sun, L.M. Yen, T.Y. Fu, Y.C. Lin, H.H. Liou, Y.S. Lin, H.C. Sie, I.C. Hsieh, Y.K. Tseng, C.W. Shu, Y.D. Hsieh, L.P. Ger, Vimentin is a potential prognostic factor for tongue squamous cell carcinoma among five epithelial-mesenchymal transition-related proteins, *PLoS One*, 12 (2017) e0178581.
- [20] M.G. Mendez, S. Kojima, R.D. Goldman, Vimentin induces changes in cell shape, motility, and adhesion during the epithelial to mesenchymal transition, *Faseb j*, 24 (2010) 1838-1851.

- [21] S. Liu, L. Liu, W. Ye, D. Ye, T. Wang, W. Guo, Y. Liao, D. Xu, H. Song, L. Zhang, H. Zhu, J. Deng, Z. Zhang, High Vimentin Expression Associated with Lymph Node Metastasis and Predicated a Poor Prognosis in Oral Squamous Cell Carcinoma, *Scientific Reports*, 6 (2016) 38834.
- [22] A. TADOKORO, N. KANAJI, D. LIU, H. YOKOMISE, R. HABA, T. ISHII, T. TAKAGI, N. WATANABE, N. KITA, N. KADOWAKI, S. BANDO, Vimentin Regulates Invasiveness and Is a Poor Prognostic Marker in Non-small Cell Lung Cancer, *Anticancer Research*, 36 (2016) 1545-1551.
- [23] R. Virtakoivu, A. Mai, E. Mattila, N. De Franceschi, S.Y. Imanishi, G. Corthals, R. Kaukonen, M. Saari, F. Cheng, E. Torvaldson, V.M. Kosma, A. Mannermaa, G. Muharram, C. Gilles, J. Eriksson, Y. Soini, J.B. Lorens, J. Ivaska, Vimentin-ERK Signaling Uncouples Slug Gene Regulatory Function, *Cancer Res*, 75 (2015) 2349-2362.
- [24] K. Yoshida, T. Saito, A. Kamida, K. Matsumoto, K. Saeki, M. Mochizuki, N. Sasaki, T. Nakagawa, Transforming growth factor- $\beta$  transiently induces vimentin expression and invasive capacity in a canine mammary gland tumor cell line, *Res Vet Sci*, 94 (2013) 539-541.
- [25] A.M. Richardson, L.S. Havel, A.E. Koyen, J.M. Konen, J. Shupe, W.G. Wiles, W.D. Martin, H.E. Grossniklaus, G. Sica, M. Gilbert-Ross, A.I. Marcus, Vimentin Is Required for Lung Adenocarcinoma Metastasis via Heterotypic Tumor Cell–Cancer-Associated Fibroblast Interactions during Collective Invasion, *Clinical Cancer Research*, 24 (2018) 420-432.
- [26] M.N. Pollak, E.S. Schernhammer, S.E. Hankinson, Insulin-like growth factors and neoplasia, *Nat Rev Cancer*, 4 (2004) 505-518.
- [27] R.C. Baxter, IGF binding proteins in cancer: mechanistic and clinical insights, *Nat Rev Cancer*, 14 (2014) 329-341.
- [28] B. Liu, H.Y. Lee, S.A. Weinzimer, D.R. Powell, J.L. Clifford, J.M. Kurie, P. Cohen, Direct functional interactions between insulin-like growth factor-binding protein-3 and retinoid X receptor-alpha regulate transcriptional signaling and apoptosis, *J Biol Chem*, 275 (2000) 33607-33613.
- [29] K.W. Lee, L.J. Cobb, V. Paharkova-Vatchkova, B. Liu, J. Milbrandt, P. Cohen, Contribution of the orphan nuclear receptor Nur77 to the apoptotic action of IGFBP-3, *Carcinogenesis*, 28 (2007) 1653-1658.
- [30] S.S. Huang, T.Y. Ling, W.F. Tseng, Y.H. Huang, F.M. Tang, S.M. Leal, J.S. Huang, Cellular growth inhibition by IGFBP-3 and TGF-beta1 requires LRP-1, *Faseb j*, 17 (2003) 2068-2081.
- [31] L.J. Schedlich, S.L. Le Page, S.M. Firth, L.J. Briggs, D.A. Jans, R.C. Baxter, Nuclear import of insulin-like growth factor-binding protein-3 and -5 is mediated by the importin beta subunit, *J Biol Chem*, 275 (2000) 23462-23470.
- [32] A. Agostini-Dreyer, A.E. Jetzt, H. Stires, W.S. Cohick, Endogenous IGFBP-3 Mediates Intrinsic Apoptosis Through Modulation of Nur77 Phosphorylation and Nuclear Export, *Endocrinology*, 156 (2015) 4141-4151.
- [33] V.A. Papadimitrakopoulou, E.N. Brown, D.D. Liu, A.K. El-Naggar, J. Jack Lee, W.K. Hong, H.-Y. Lee, The prognostic role of loss of insulin-like growth factor-binding protein-3 expression in head and neck carcinogenesis, *Cancer Letters*, 239 (2006) 136-143.
- [34] G. Song, K. Liu, X. Zhu, X. Yang, Y. Shen, W. Wang, G. Shi, Q. Li, Y. Duan, Y. Zhao, G. Feng, The low IGFBP-3 level is associated with esophageal cancer patients: a meta-analysis, *World J Surg Oncol*, 14 (2016) 307-307.
- [35] Y.S. Chang, K. Gong, S. Sun, D. Liu, A.K. El-Naggar, F.R. Khuri, W.K. Hong, H.-Y. Lee, Clinical Significance of Insulin-like Growth Factor-binding Protein-3 Expression in Stage I Non-Small Cell Lung Cancer, *Clinical Cancer Research*, 8 (2002) 3796-3802.
- [36] H.Y. Lee, K.H. Chun, B. Liu, S.A. Wiehle, R.J. Cristiano, W.K. Hong, P. Cohen, J.M. Kurie, Insulin-like growth factor binding protein-3 inhibits the growth of non-small cell lung cancer, *Cancer Res*, 62 (2002) 3530-3537.
- [37] N. Bhattacharyya, K. Pechhold, H. Shahjee, G. Zappala, C. Elbi, B. Raaka, M. Wiench, J. Hong, M.M. Rechler, Nonsecreted Insulin-like Growth Factor Binding Protein-3 (IGFBP-3) Can Induce

Apoptosis in Human Prostate Cancer Cells by IGF-independent Mechanisms without Being Concentrated in the Nucleus, *Journal of Biological Chemistry*, 281 (2006) 24588-24601.

[38] J.-H. Kim, D.S. Choi, O.-H. Lee, S.-H. Oh, S.M. Lippman, H.-Y. Lee, Antiangiogenic antitumor activities of IGFBP-3 are mediated by IGF-independent suppression of Erk1/2 activation and Egr-1-mediated transcriptional events, *Blood*, 118 (2011) 2622-2631.

[39] H.J. Lee, J.S. Lee, S.J. Hwang, H.Y. Lee, Insulin-like growth factor binding protein-3 inhibits cell adhesion via suppression of integrin  $\beta$ 4 expression, *Oncotarget*, 6 (2015) 15150-15163.

[40] S.H. Oh, O.H. Lee, C.P. Schroeder, Y.W. Oh, S. Ke, H.J. Cha, R.W. Park, A. Onn, R.S. Herbst, C. Li, H.Y. Lee, Antimetastatic activity of insulin-like growth factor binding protein-3 in lung cancer is mediated by insulin-like growth factor-independent urokinase-type plasminogen activator inhibition, *Mol Cancer Ther*, 5 (2006) 2685-2695.

[41] H.H. Mehta, Q. Gao, C. Galet, V. Paharkova, J. Wan, J. Said, J.J. Sohn, G. Lawson, P. Cohen, L.J. Cobb, K.-W. Lee, IGFBP-3 Is a Metastasis Suppression Gene in Prostate Cancer, *Cancer Research*, 71 (2011) 5154-5163.

[42] P.L. Torng, Y.C. Lee, C.Y. Huang, J.H. Ye, Y.S. Lin, Y.W. Chu, S.C. Huang, P. Cohen, C.W. Wu, C.T. Lin, Insulin-like growth factor binding protein-3 (IGFBP-3) acts as an invasion-metastasis suppressor in ovarian endometrioid carcinoma, *Oncogene*, 27 (2008) 2137-2147.

[43] J.-H. Kim, D.S. Choi, O.-H. Lee, S.-H. Oh, S.M. Lippman, H.-Y. Lee, Antiangiogenic antitumor activities of IGFBP-3 are mediated by IGF-independent suppression of Erk1/2 activation and Egr-1-mediated transcriptional events, *Blood*, 118 (2011) 2622-2631.

[44] H.H. Mehta, Q. Gao, C. Galet, V. Paharkova, J. Wan, J. Said, J.J. Sohn, G. Lawson, P. Cohen, L.J. Cobb, K.-W. Lee, IGFBP-3 Is a Metastasis Suppression Gene in Prostate Cancer, *Cancer Research*, 71 (2011) 5154.

[45] P.L. Torng, Y.C. Lee, C.Y. Huang, J.H. Ye, Y.S. Lin, Y.W. Chu, S.C. Huang, P. Cohen, C.W. Wu, C.T. Lin, Insulin-like growth factor binding protein-3 (IGFBP-3) acts as an invasion-metastasis suppressor in ovarian endometrioid carcinoma, *Oncogene*, 27 (2008) 2137-2147.

[46] M.J. Blouin, M. Bazile, E. Birman, M. Zakikhani, L. Florianova, O. Aleynikova, D.R. Powell, M. Pollak, Germ line knockout of IGFBP-3 reveals influences of the gene on mammary gland neoplasia, *Breast Cancer Res Treat*, 149 (2015) 577-585.

[47] Y.S. Chang, L. Wang, Y.-A. Suh, L. Mao, S.J. Karpen, F.R. Khuri, W.K. Hong, H.-Y. Lee, Mechanisms underlying lack of insulin-like growth factor-binding protein-3 expression in non-small-cell lung cancer, *Oncogene*, 23 (2004) 6569-6580.

[48] J. Xu, S. Lamouille, R. Derynck, TGF-beta-induced epithelial to mesenchymal transition, *Cell Res*, 19 (2009) 156-172.

[49] T. Shibue, R.A. Weinberg, EMT, CSCs, and drug resistance: the mechanistic link and clinical implications, *Nat Rev Clin Oncol*, 14 (2017) 611-629.

[50] S. Tanabe, S. Quader, H. Cabral, R. Ono, Interplay of EMT and CSC in Cancer and the Potential Therapeutic Strategies, *Frontiers in Pharmacology*, 11 (2020).

[51] D.W. Clark, K. Palle, Aldehyde dehydrogenases in cancer stem cells: potential as therapeutic targets, *Ann Transl Med*, 4 (2016) 518.

[52] W.Y. Kim, M.J. Kim, H. Moon, P. Yuan, J.S. Kim, J.K. Woo, G. Zhang, Y.A. Suh, L. Feng, C. Behrens, C.S. Van Pelt, H. Kang, J.J. Lee, W.K. Hong, Wistuba, II, H.Y. Lee, Differential impacts of insulin-like growth factor-binding protein-3 (IGFBP-3) in epithelial IGF-induced lung cancer development, *Endocrinology*, 152 (2011) 2164-2173.

[53] X.-H. Tang, B. Knudsen, D. Bemis, S. Tickoo, L.J. Gudas, Oral Cavity and Esophageal Carcinogenesis Modeled in Carcinogen-Treated Mice, *Clinical Cancer Research*, 10 (2004) 301-313.

[54] R.A. Schoop, M.H. Noteborn, R.J. Baatenburg de Jong, A mouse model for oral squamous cell carcinoma, *J Mol Histol*, 40 (2009) 177-181.

[55] L.P. Smith, G.R. Thomas, Animal models for the study of squamous cell carcinoma of the upper aerodigestive tract: a historical perspective with review of their utility and limitations. Part

- A. Chemically-induced de novo cancer, syngeneic animal models of HNSCC, animal models of transplanted xenogeneic human tumors, *Int J Cancer*, 118 (2006) 2111-2122.
- [56] C.D. Woodworth, E. Michael, L. Smith, K. Vijayachandra, A. Glick, H. Hennings, S.H. Yuspa, Strain-dependent differences in malignant conversion of mouse skin tumors is an inherent property of the epidermal keratinocyte, *Carcinogenesis*, 25 (2004) 1771-1778.
- [57] G.T. Stathopoulos, T.P. Sherrill, D.S. Cheng, R.M. Scoggins, W. Han, V.V. Polosukhin, L. Connelly, F.E. Yull, B. Fingleton, T.S. Blackwell, Epithelial NF-kappaB activation promotes urethane-induced lung carcinogenesis, *Proc Natl Acad Sci U S A*, 104 (2007) 18514-18519.
- [58] N. Wakamatsu, T.R. Devereux, H.H. Hong, R.C. Sills, Overview of the molecular carcinogenesis of mouse lung tumor models of human lung cancer, *Toxicol Pathol*, 35 (2007) 75-80.
- [59] T. Nomura, Diminution of tumorigenesis initiated by 4-nitroquinoline-l-oxide by post-treatment with caffeine in mice, *Nature*, 260 (1976) 547-549.
- [60] S. Maier, T. Wilbertz, M. Braun, V. Scheble, M. Reischl, R. Mikut, R. Menon, P. Nikolov, K. Petersen, C. Beschorner, H. Moch, C. Kakies, C. Protzel, J. Bauer, A. Soltermann, F. Fend, A. Staebler, C. Lengerke, S. Perner, SOX2 amplification is a common event in squamous cell carcinomas of different organ sites, *Hum Pathol*, 42 (2011) 1078-1088.
- [61] C.K. Buckway, E.M. Wilson, M. Ahlsén, P. Bang, Y. Oh, R.G. Rosenfeld, Mutation of three critical amino acids of the N-terminal domain of IGF-binding protein-3 essential for high affinity IGF binding, *J Clin Endocrinol Metab*, 86 (2001) 4943-4950.
- [62] S.H. Kao, W.L. Wang, C.Y. Chen, Y.L. Chang, Y.Y. Wu, Y.T. Wang, S.P. Wang, A.I. Nesvizhskii, Y.J. Chen, T.M. Hong, P.C. Yang, Analysis of Protein Stability by the Cycloheximide Chase Assay, *Bio Protoc*, 5 (2015).
- [63] Y.L. Deribe, T. Pawson, I. Dikic, Post-translational modifications in signal integration, *Nature Structural & Molecular Biology*, 17 (2010) 666-672.
- [64] Y. Zhu, Y. Zhang, Z. Sui, Y. Zhang, M. Liu, H. Tang, USP14 de-ubiquitinates vimentin and miR-320a modulates USP14 and vimentin to contribute to malignancy in gastric cancer cells, *Oncotarget*, 8 (2017) 48725-48736.
- [65] M. Galanis, S.M. Firth, J. Bond, A. Nathanielsz, A.A. Kortt, P.J. Hudson, R.C. Baxter, Ligand-binding characteristics of recombinant amino- and carboxyl-terminal fragments of human insulin-like growth factor-binding protein-3, *J Endocrinol*, 169 (2001) 123-133.
- [66] M. Müller, S.S. Bhattacharya, T. Moore, Q. Prescott, T. Wedig, H. Herrmann, T.M. Magin, Dominant cataract formation in association with a vimentin assembly disrupting mutation, *Hum Mol Genet*, 18 (2009) 1052-1057.
- [67] A. Aziz, J.F. Hess, M.S. Budamagunta, P.G. FitzGerald, J.C. Voss, Head and rod 1 interactions in vimentin: identification of contact sites, structure, and changes with phosphorylation using site-directed spin labeling and electron paramagnetic resonance, *J Biol Chem*, 284 (2009) 7330-7338.
- [68] T. Cardozo, M. Pagano, The SCF ubiquitin ligase: insights into a molecular machine, *Nat Rev Mol Cell Biol*, 5 (2004) 739-751.
- [69] Y.-H. Cui, H. Kim, M. Lee, J.M. Yi, R.-K. Kim, N. Uddin, K.-C. Yoo, J.H. Kang, M.-Y. Choi, H.-J. Cha, O.-S. Kwon, I.-H. Bae, M.-J. Kim, N. Kaushik, S.-J. Lee, FBXL14 abolishes breast cancer progression by targeting CDCP1 for proteasomal degradation, *Oncogene*, 37 (2018) 5794-5809.
- [70] J.H. Kang, M.Y. Choi, Y.H. Cui, N. Kaushik, N. Uddin, K.C. Yoo, M.J. Kim, S.J. Lee, Regulation of FBXO4-mediated ICAM-1 protein stability in metastatic breast cancer, *Oncotarget*, 8 (2017) 83100-83113.
- [71] R. Viñas-Castells, M. Beltran, G. Valls, I. Gómez, J.M. García, B. Montserrat-Sentís, J. Baulida, F. Bonilla, A.G. de Herreros, V.M. Díaz, The hypoxia-controlled FBXL14 ubiquitin ligase targets SNAIL1 for proteasome degradation, *J Biol Chem*, 285 (2010) 3794-3805.
- [72] J. Zhong, K. Ogura, Z. Wang, H. Inuzuka, Degradation of the transcription factor Twist, an oncoprotein that promotes cancer metastasis, *Discov Med*, 15 (2013) 7-15.
- [73] R.L. Anderson, T. Balasas, J. Callaghan, R.C. Coombes, J. Evans, J.A. Hall, S. Kinrade, D. Jones, P.S. Jones, R. Jones, J.F. Marshall, M.B. Panico, J.A. Shaw, P.S. Steeg, M. Sullivan, W. Tong, A.D.

Westwell, J.W.A. Ritchie, U.K. on behalf of the Cancer Research, C.R.C.A.M.W.G. Cancer Therapeutics, A framework for the development of effective anti-metastatic agents, *Nature Reviews Clinical Oncology*, 16 (2019) 185-204.

[74] J.E. Talmadge, I.J. Fidler, AACR centennial series: the biology of cancer metastasis: historical perspective, *Cancer Res*, 70 (2010) 5649-5669.

[75] T.N. Seyfried, L.C. Huysentruyt, On the origin of cancer metastasis, *Crit Rev Oncog*, 18 (2013) 43-73.

[76] R. Kalluri, R.A. Weinberg, The basics of epithelial-mesenchymal transition, *J Clin Invest*, 119 (2009) 1420-1428.

[77] L.S. Havel, E.R. Kline, A.M. Salgueiro, A.I. Marcus, Vimentin regulates lung cancer cell adhesion through a VAV2-Rac1 pathway to control focal adhesion kinase activity, *Oncogene*, 34 (2015) 1979-1990.

[78] D.C. Phua, P.O. Humbert, W. Hunziker, Vimentin regulates scribble activity by protecting it from proteasomal degradation, *Mol Biol Cell*, 20 (2009) 2841-2855.

[79] M.J. Bollong, M. Pietilä, A.D. Pearson, T.R. Sarkar, I. Ahmad, R. Soundararajan, C.A. Lyssiotis, S.A. Mani, P.G. Schultz, L.L. Lairson, A vimentin binding small molecule leads to mitotic disruption in mesenchymal cancers, *Proceedings of the National Academy of Sciences*, 114 (2017) E9903-E9912.

[80] N.T. Snider, N.O. Ku, M.B. Omary, The sweet side of vimentin, *Elife*, 7 (2018).

[81] A.E. Vernon, C. LaBonne, Slug stability is dynamically regulated during neural crest development by the F-box protein Ppa, *Development*, 133 (2006) 3359-3370.

[82] J.E. Visvader, G.J. Lindeman, Cancer stem cells in solid tumours: accumulating evidence and unresolved questions, *Nat Rev Cancer*, 8 (2008) 755-768.

[83] X. Li, M.T. Lewis, J. Huang, C. Gutierrez, C.K. Osborne, M.F. Wu, S.G. Hilsenbeck, A. Pavlick, X. Zhang, G.C. Chamness, H. Wong, J. Rosen, J.C. Chang, Intrinsic resistance of tumorigenic breast cancer cells to chemotherapy, *J Natl Cancer Inst*, 100 (2008) 672-679.

[84] S. Bao, Q. Wu, R.E. McLendon, Y. Hao, Q. Shi, A.B. Hjelmeland, M.W. Dewhirst, D.D. Bigner, J.N. Rich, Glioma stem cells promote radioresistance by preferential activation of the DNA damage response, *Nature*, 444 (2006) 756-760.

[85] A. Wiechert, C. Saygin, P.S. Thiagarajan, V.S. Rao, J.S. Hale, N. Gupta, M. Hitomi, A.B. Nagaraj, A. DiFeo, J.D. Lathia, O. Reizes, Cisplatin induces stemness in ovarian cancer, *Oncotarget*, 7 (2016) 30511-30522.

[86] V. Plaks, N. Kong, Z. Werb, The cancer stem cell niche: how essential is the niche in regulating stemness of tumor cells?, *Cell Stem Cell*, 16 (2015) 225-238.

[87] J.A. Clara, C. Monge, Y. Yang, N. Takebe, Targeting signalling pathways and the immune microenvironment of cancer stem cells — a clinical update, *Nature Reviews Clinical Oncology*, 17 (2020) 204-232.

[88] C. Ginestier, M.H. Hur, E. Charafe-Jauffret, F. Monville, J. Dutcher, M. Brown, J. Jacquemier, P. Viens, C.G. Kleer, S. Liu, A. Schott, D. Hayes, D. Birnbaum, M.S. Wicha, G. Dontu, ALDH1 is a marker of normal and malignant human mammary stem cells and a predictor of poor clinical outcome, *Cell stem cell*, 1 (2007) 555-567.

[89] T. Yamashita, J. Ji, A. Budhu, M. Forgues, W. Yang, H.-Y. Wang, H. Jia, Q. Ye, L.-X. Qin, E. Wauthier, L.M. Reid, H. Minato, M. Honda, S. Kaneko, Z.-Y. Tang, X.W. Wang, EpCAM-positive hepatocellular carcinoma cells are tumor-initiating cells with stem/progenitor cell features, *Gastroenterology*, 136 (2009) 1012-1024.

[90] S.K. Singh, C. Hawkins, I.D. Clarke, J.A. Squire, J. Bayani, T. Hide, R.M. Henkelman, M.D. Cusimano, P.B. Dirks, Identification of human brain tumour initiating cells, *Nature*, 432 (2004) 396-401.

[91] P.C. Hermann, S.L. Huber, T. Herrler, A. Aicher, J.W. Ellwart, M. Guba, C.J. Bruns, C. Heeschen, Distinct Populations of Cancer Stem Cells Determine Tumor Growth and Metastatic Activity in Human Pancreatic Cancer, *Cell Stem Cell*, 1 (2007) 313-323.

- [92] G. Jego, A. Hazoumé, R. Seigneuric, C. Garrido, Targeting heat shock proteins in cancer, *Cancer Lett*, 332 (2013) 275-285.
- [93] M. Taipale, D.F. Jarosz, S. Lindquist, HSP90 at the hub of protein homeostasis: emerging mechanistic insights, *Nat Rev Mol Cell Biol*, 11 (2010) 515-528.
- [94] F.H. Schopf, M.M. Biebl, J. Buchner, The HSP90 chaperone machinery, *Nat Rev Mol Cell Biol*, 18 (2017) 345-360.
- [95] L. Neckers, P. Workman, Hsp90 molecular chaperone inhibitors: are we there yet?, *Clin Cancer Res*, 18 (2012) 64-76.
- [96] J.S. Isaacs, W. Xu, L. Neckers, Heat shock protein 90 as a molecular target for cancer therapeutics, *Cancer Cell*, 3 (2003) 213-217.
- [97] S. Modi, A. Stopeck, H. Linden, D. Solit, S. Chandarlapaty, N. Rosen, G. D'Andrea, M. Dickler, M.E. Moynahan, S. Sugarman, W. Ma, S. Patil, L. Norton, A.L. Hannah, C. Hudis, HSP90 inhibition is effective in breast cancer: a phase II trial of tanespimycin (17-AAG) plus trastuzumab in patients with HER2-positive metastatic breast cancer progressing on trastuzumab, *Clin Cancer Res*, 17 (2011) 5132-5139.
- [98] C.Z. Wang, S. Anderson, W. Du, T.C. He, C.S. Yuan, Red ginseng and cancer treatment, *Chin J Nat Med*, 14 (2016) 7-16.
- [99] C.Z. Wang, Z. Zhang, J.Y. Wan, C.F. Zhang, S. Anderson, X. He, C. Yu, T.C. He, L.W. Qi, C.S. Yuan, Protopanaxadiol, an active ginseng metabolite, significantly enhances the effects of fluorouracil on colon cancer, *Nutrients*, 7 (2015) 799-814.
- [100] S. Chen, Z. Wang, Y. Huang, S.A. O'Barr, R.A. Wong, S. Yeung, M.S.S. Chow, Ginseng and Anticancer Drug Combination to Improve Cancer Chemotherapy: A Critical Review, *Evidence-Based Complementary and Alternative Medicine*, 2014 (2014) 168940.
- [101] K.W. Leung, L.W. Cheung, Y.L. Pon, R.N. Wong, N.K. Mak, T.P. Fan, S.C. Au, J. Tombran-Tink, A.S. Wong, Ginsenoside Rb1 inhibits tube-like structure formation of endothelial cells by regulating pigment epithelium-derived factor through the oestrogen beta receptor, *Br J Pharmacol*, 152 (2007) 207-215.
- [102] B. Li, J. Zhao, C.Z. Wang, J. Searle, T.C. He, C.S. Yuan, W. Du, Ginsenoside Rh2 induces apoptosis and paraptosis-like cell death in colorectal cancer cells through activation of p53, *Cancer Lett*, 301 (2011) 185-192.
- [103] N.W. He, Y. Zhao, L. Guo, J. Shang, X.B. Yang, Antioxidant, antiproliferative, and pro-apoptotic activities of a saponin extract derived from the roots of *Panax notoginseng* (Burk.) F.H. Chen, *J Med Food*, 15 (2012) 350-359.
- [104] J.L. Gao, G.Y. Lv, B.C. He, B.Q. Zhang, H. Zhang, N. Wang, C.Z. Wang, W. Du, C.S. Yuan, T.C. He, Ginseng saponin metabolite 20(S)-protopanaxadiol inhibits tumor growth by targeting multiple cancer signaling pathways, *Oncol Rep*, 30 (2013) 292-298.
- [105] J.H. Cheong, H. Kim, M.J. Hong, M.H. Yang, J.W. Kim, H. Yoo, H. Yang, J.H. Park, S.H. Sung, H.P. Kim, J. Kim, Stereoisomer-specific anticancer activities of ginsenoside Rg3 and Rh2 in HepG2 cells: disparity in cytotoxicity and autophagy-inducing effects due to 20(S)-epimers, *Biol Pharm Bull*, 38 (2015) 102-108.
- [106] A. Ahuja, J.H. Kim, J.-H. Kim, Y.-S. Yi, J.Y. Cho, Functional role of ginseng-derived compounds in cancer, *Journal of Ginseng Research*, 42 (2018) 248-254.
- [107] G.C. Fan, Role of heat shock proteins in stem cell behavior, *Prog Mol Biol Transl Sci*, 111 (2012) 305-322.
- [108] D.R. Ciocca, A.P. Arrigo, S.K. Calderwood, Heat shock proteins and heat shock factor 1 in carcinogenesis and tumor development: an update, *Arch Toxicol*, 87 (2013) 19-48.
- [109] S. Singh, B. Sharma, S.S. Kanwar, A. Kumar, Lead Phytochemicals for Anticancer Drug Development, *Front Plant Sci*, 7 (2016) 1667.
- [110] K.-t. Choi, Botanical characteristics, pharmacological effects and medicinal components of Korean *Panax ginseng* C A Meyer, *Acta Pharmacologica Sinica*, 29 (2008) 1109-1118.

- [111] L. Johnson, K. Mercer, D. Greenbaum, R.T. Bronson, D. Crowley, D.A. Tuveson, T. Jacks, Somatic activation of the K-ras oncogene causes early onset lung cancer in mice, *Nature*, 410 (2001) 1111-1116.
- [112] M.C. Yang, D.S. Seo, S.U. Choi, Y.H. Park, K.R. Lee, Polyacetylenes from the roots of cultivated-wild ginseng and their cytotoxicity in vitro, *Arch Pharm Res*, 31 (2008) 154-159.
- [113] L. Giulino-Roth, H.J. van Besien, T. Dalton, J.E. Totonchy, A. Rodina, T. Taldone, A. Bolaender, H. Erdjument-Bromage, J. Sadek, A. Chadburn, M.J. Barth, F.S. Dela Cruz, A. Rainey, A.L. Kung, G. Chiosis, E. Cesarman, Inhibition of Hsp90 Suppresses PI3K/AKT/mTOR Signaling and Has Antitumor Activity in Burkitt Lymphoma, *Mol Cancer Ther*, 16 (2017) 1779-1790.
- [114] L.N. Abdullah, E.K. Chow, Mechanisms of chemoresistance in cancer stem cells, *Clin Transl Med*, 2 (2013) 3.
- [115] S.C. Lee, H.Y. Min, H. Choi, S.Y. Bae, K.H. Park, S.Y. Hyun, H.J. Lee, J. Moon, S.H. Park, J.Y. Kim, H. An, S.J. Park, J.H. Seo, S. Lee, Y.M. Kim, H.J. Park, S.K. Lee, J. Lee, J. Lee, K.W. Kim, Y.G. Suh, H.Y. Lee, Deguelin Analogue SH-1242 Inhibits Hsp90 Activity and Exerts Potent Anticancer Efficacy with Limited Neurotoxicity, *Cancer Res*, 76 (2016) 686-699.
- [116] K.M. Haigis, K.R. Kendall, Y. Wang, A. Cheung, M.C. Haigis, J.N. Glickman, M. Niwa-Kawakita, A. Sweet-Cordero, J. Sebolt-Leopold, K.M. Shannon, J. Settleman, M. Giovannini, T. Jacks, Differential effects of oncogenic K-Ras and N-Ras on proliferation, differentiation and tumor progression in the colon, *Nat Genet*, 40 (2008) 600-608.
- [117] Z. Zhao, J. Zuber, E. Diaz-Flores, L. Lintault, S.C. Kogan, K. Shannon, S.W. Lowe, p53 loss promotes acute myeloid leukemia by enabling aberrant self-renewal, *Genes Dev*, 24 (2010) 1389-1402.
- [118] L.A. Pikor, V.R. Ramnarine, S. Lam, W.L. Lam, Genetic alterations defining NSCLC subtypes and their therapeutic implications, *Lung Cancer*, 82 (2013) 179-189.
- [119] H.-J. Boo, H.-Y. Min, H.-J. Jang, H.J. Yun, J.K. Smith, Q. Jin, H.-J. Lee, D. Liu, H.-S. Kweon, C. Behrens, J.J. Lee, I.I. Wistuba, E. Lee, W.K. Hong, H.-Y. Lee, The tobacco-specific carcinogen-operated calcium channel promotes lung tumorigenesis via IGF2 exocytosis in lung epithelial cells, *Nat Commun*, 7 (2016) 12961.
- [120] A. Kreso, J.E. Dick, Evolution of the cancer stem cell model, *Cell Stem Cell*, 14 (2014) 275-291.
- [121] B. Beck, C. Blanpain, Unravelling cancer stem cell potential, *Nat Rev Cancer*, 13 (2013) 727-738.
- [122] D.R. Pattabiraman, R.A. Weinberg, Tackling the cancer stem cells - what challenges do they pose?, *Nat Rev Drug Discov*, 13 (2014) 497-512.
- [123] Y. Wu, B. Huang, Q. Liu, Y. Liu, Heat shock protein 90- $\beta$  over-expression is associated with poor survival in stage I lung adenocarcinoma patients, *Int J Clin Exp Pathol*, 8 (2015) 8252-8259.
- [124] R.K. Ramanathan, D.L. Trump, J.L. Eisman, C.P. Belani, S.S. Agarwala, E.G. Zuhowski, J. Lan, D.M. Potter, S.P. Ivy, S. Ramalingam, A.M. Brufsky, M.K.K. Wong, S. Tutchko, M.J. Egorin, Phase I Pharmacokinetic-Pharmacodynamic Study of 17-(Allylamino)-17-Demethoxygeldanamycin (17AAG, NSC 330507), a Novel Inhibitor of Heat Shock Protein 90, in Patients with Refractory Advanced Cancers, *Clinical Cancer Research*, 11 (2005) 3385-3391.
- [125] L.P. Christensen, K. Brandt, Bioactive polyacetylenes in food plants of the Apiaceae family: occurrence, bioactivity and analysis, *J Pharm Biomed Anal*, 41 (2006) 683-693.
- [126] Y.C. Kuo, Y.L. Lin, C.P. Huang, J.W. Shu, W.J. Tsai, A tumor cell growth inhibitor from *Saposhnikovia divaricata*, *Cancer Invest*, 20 (2002) 955-964.
- [127] K.W. Tan, D.P. Killeen, Y. Li, J.W. Paxton, N.P. Birch, A. Scheepens, Dietary polyacetylenes of the falcarinol type are inhibitors of breast cancer resistance protein (BCRP/ABCG2), *Eur J Pharmacol*, 723 (2014) 346-352.

# ACKNOWLEDGEMENT

Foremost, I would like to express my sincere gratitude to my advisor - Prof. Ho-Young Lee, for her instruction and support during my Ph.D. study program, for her enthusiasm, motivation, and immense knowledge.

Besides my professor, I would appreciate all the committee members: Prof. Young Kee Shin, Prof. Yun-Hee Lee, Prof. Woo-Young Kim, Prof. Hyo-Jong Lee for all of their encourages, comments, and advice that help me improve and complete this thesis.

I would appreciate prof. Jeong Hill Park for introducing me to SNU, for his support and kindness to my husband and me when we studied here!

I would like to thank my partner - Ho-Jin Lee, who worked hard and support me a lot to complete essential experiments in this study. The researcher contributed to the following results in chapter 1 of this thesis:

Figure: 1-5,6, 10A, 17A, 16D data of H226B cells.

Figure 1-16CB: IF staining H1299 cells

Figure 1-11, 1-13, 1-16D: 4-NQO induced HNSCC and NSCLC xenograft models

I would like to thank my husband, Truong Huy Nguyen, who purified the *P. ginseng* fractions and panaxynol in chapter 2 of this thesis. He contributed to the following results:

Figure 2-3, 2-5: the purification of the saponin, non-saponin, and non-saponin subfractions isolated from *P.ginseng*.

Figure 2-5: the isolation F2 fraction and the identification of the compound panaxynol.

I would like to thank Dr. Hye Young Min, who supported me a lot during the paper submission and thesis preparation.

I would like to thank all the lab members: Dr. Hye Jin Lee, Dr. Ji Son Lee, Ho-Jin Lee, Jaebeom Cho, Syun Yeob Hyung, Huyn Ji Jang, Myong Kyung Noh, Ji Hwan Ann, Hye

Jeong Yun, Xuan, Sim Jeong Yeon, Hyukjin Kwon for their support during my Ph.D. study and thesis defense.

I want to thank my family: my mother, my parent-in-law, my husband, my brothers, sisters for their encouragement and support during my study in Korea.

Thank my daughter for giving hope, happiness, and love to my life.

During the time I was staying in Korea. I have received help and support from many people: seniors, juniors, and friends..... and I genuinely want to send all of them a great appreciation for their kindness, which makes me feel warm as I was in my home, family, and country.

I have learned many lessons in life in Korea, which makes me stronger and mature.

Thank Seoul National University, and I am proud to be a member of you!